UNIVERSIDAD DE CHILE
FACULTAD DE CIENCIAS FÍSICAS Y MATEMÁTICAS
DEPARTAMENTO DE FÍSICA

# MANIPULATION OF SQUEEZED LIGHT IN A ONE-DIMENSIONAL TOPOLOGICAL SYSTEM

TESIS PARA OPTAR AL GRADO DE MAGÍSTER, MENCIÓN FÍSICA

GABRIEL O'RYAN PÉREZ

PROFESORES GUÍAS:
Carla Hermann-Avigliano
Luis E.F. Foà Torres

MIEMBROS DE LA COMISIÓN:
Rodrigo A. Vicencio
Pablo Solano

Este trabajo ha sido parcialmente financiado por:
Fondo Nacional de Desarrollo Científico y Tecnológico FONDECYT y el
Instituto Milenio de Investigación en Óptica MIRO.

SANTIAGO DE CHILE
2023

# MANIPULATION OF SQUEEZED LIGHT IN A ONE-DIMENSIONAL TOPOLOGICAL SYSTEM


**Resumen en español**

Durante el siglo XX, se evidenciaron las limitaciones de la física clásica. Esta nos brinda una comprensión adecuada del mundo cotidiano, pero se queda corta al intentar describir fenómenos en escalas extremadamente grandes o diminutas. Es aquí donde entra en juego la física cuántica, que se encarga de describir la naturaleza a niveles atómicos y subatómicos. En este dominio emergen propiedades cuánticas únicas, las cuales posibilitan fenómenos y tecnologías sin paralelo en el ámbito clásico. En los últimos años, los creciente avances tecnológicos en el control y uso de propiedades cuánticas muestran la posibilidad futura de crear, propagar y usar de forma confiable y escalable los sistemas cuánticos.

Un ejemplo de tecnología actual que utiliza propiedades cuánticas es el estado comprimido del campo electromagnético (squeezed state), que permite aumentar la precisión en una cuadratura del campo a costa de perder en la cuadratura ortogonal. Han sido principalmente utilizados en metrología [1], más famosamente en la detección de ondas gravitacionales [2], y en la computación cuántica [3]. Entre los sistemas para propagar luz, se encuentran las guías de onda, en ellas, la luz puede ser propagada y guiada dentro de un medio al cambiar localmente el índice de refracción. Crear varias guías de onda forman una red fotónica y la luz puede progaparse a través de ellas de forma análoga a un electrón en una red cristalina. De la mano con esto, los aislantes topológicos en la materia condensada, se caracterizan por un número topológico obtenido del bulto de la red. Este número está relacionado con la aparición de estados localizados robustos en el borde. Quizás el ejemplo más famoso es el efecto Hall cuántico [4], donde la precisión de la conductancia medida permitió la redefinición de constantes universales [5]. Esto no es único a la electrónica y, en los últimos años, ha habido un gran interés en el área de fotónica topológica debido a la capacidad de estos sistemas para controlar y proteger a la luz usando las propiedades topológicas [6, 7, 8]. A pesar de que luz cuántica ha sido utilizada en algunos casos [9], los efectos topológicos en las propiedades cuánticas de la luz aún no han sido completamente explicados y comprendidos. Esta tesis parte de la premisa de utilizar la robustez de la luz comprimida debido a los efectos conocidos de la topología [10]. Esto se realiza a través de una red fotónica topológica unidimensional, en la cuál, al modificar el sistema sin romper la topología, generamos interacciones entre la luz comprimida. Esto se explica y caracteriza utilizando los parámetros del sistema y más tarde, se prueba la robustez para comprender los beneficios que otorga la topología.

La búsqueda de tecnologías cuánticas confiables y robustas para propagar y manipular la luz cuántica todavía continúa. Esperamos que esta tesis impulse el uso de sistemas topológicos para mejorar el control y la estabilidad de la luz comprimida a través de guías de onda.

## MANIPULATION OF SQUEEZED LIGHT IN A ONE-DIMENSIONAL TOPOLOGICAL SYSTEM

**Summary in english**

During the 20th century, the limitations of classical physics became evident. While classical physics provides us with a proper understanding of the everyday world, it falls short when attempting to describe phenomena on extremely large or tiny scales. This is where quantum physics comes into play, which deals with describing nature at atomic and subatomic levels. In this domain, unique quantum properties emerge, enabling phenomena and technologies unparalleled in the classical realm. In recent years, the growing technological advancements in controlling and utilizing quantum properties show the future potential to create, propagate, and reliably scale quantum systems.

An example of current technology utilizing quantum properties is the squeezed state of the electromagnetic field, which allows for increased precision in one quadrature of the field at the expense of losing precision in the orthogonal quadrature. These states have mainly been used in metrology [1], most famously in the detection of gravitational waves [2], and in quantum computing [3]. Among light propagation systems, waveguides are present where light can be guided and propagated within a medium by locally changing the refractive index. Multiple waveguides create a photonic network, and light can propagate through them similarly to an electron in a crystalline lattice. Alongside this, topological insulators in condensed matter are characterized by a topological number obtained from the lattice's bulk. This number is related to the appearance of robust localized states at the edge. Perhaps the most famous example is the quantum Hall effect [4], where the precision of measured conductance led to the redefinition of universal constants [5]. This phenomenon is not unique to electronics, and in recent years, there has been great interest in the field of topological photonics due to these systems' ability to control and protect light using topological properties [6, 7, 8]. Despite quantum light having been used in some cases [9], the topological effects on the quantum properties of light have not yet been fully explained and understood.

This thesis is based on the premise of utilizing the robustness of squeezed light due to known topological effects [10]. This is achieved through a one-dimensional topological photonic network, in which, by modifying the system without breaking topology, we generate interactions among squeezed light. This is explained and characterized using the system's parameters, and later, the robustness is tested to understand the benefits conferred by topology. The search for reliable and robust quantum technologies to propagate and manipulate quantum light continues. We hope that this thesis will drive the use of topological systems to enhance the control and stability of squeezed light through waveguides.

*Para mi familia, amigos, y cercanos que pusieron su granito en mi, soy gracias a ustedes.*

***Vendisuone***

# Agradecimientos

Tengo harto que agradecer pero no creo poder acordarme de todos ni todas, asique iré por lo grupos de mi vida y si alguien cree que falta, no se lo tome a pecho, invíteme a salir y salga en la siguiente dedicatoria (ayiaa).
Quisiera partir agradeciendo a mi familia por el constante apoyo y cariño que me han dado, por respetar mis tiempos pero apurándome para no quedarme atrás, estar constantemente ayudándome, y enseñarme a disfrutar la vida respetando y cuidando al otro.
Agradezco a los cabros de Talca por todas las juntas, juegos, risas, conversas y asados que han habido (y habrán), con conversaciones tan chistosas que da risa el recuerdo y otras tan profundas que siguen guiándome.
Agradezco a toda la gente de mi pregrado, estemos en contacto o no, a pesar de ser años confusos, tuve los mejores carretes y baciles de la U en esos años.
Agradezco a la salita por toda su gente y el tremendo espacio que fué en mi entrada a física, conociendo a personas que compartiré toda mi vida y viviendo experiencias únicas, aprendí y disfruté muchísimo en especial de la compañía.
Agradecer a la gente del tercero, por estos últimos años de apañe, café, investigación, quejas y risas. A toda la gente bonita que he conocido y amistades que hemos construido. Mención especial al Luquitas y su café, parte crucial para la realización de esta tesis.
Por último, quiero agradecer a cada persona que me compartió una risa, consejo, crítica, historia o mirada, esas son las acciones que hacen disfrutar e impulsar cada día.
La vida es compartir y compartirse ya que todo es mejor acompañado.

# Contents

# Figure index

# Introduction

This thesis consists of six chapters, the first 4 chapters will set the fundamentals to understand the theory. The fifth chapter fills all the details and bounds together with the topic explained before with the purpose of presenting the system under study. The results, analysis, and conclusions are shown in the last chapter.

The first chapter briefly introduces the history of topological systems, mainly in condensed matter, and explains the basic properties of topological systems and their relation to symmetries. To do this we use the Su-Schrieffer–Heeger model and calculate its band structure, topological invariant, and edge states while addressing the limits of the topology. We also introduce localized states in domain walls and how to move them using a time-dependent Hamiltonian.

The second chapter introduces photonic systems and the propagation of light through waveguides. The evolution of light is calculated using the coupled mode approximation for one and two waveguides to then generalize a photonic lattice. We finalize this section by commenting on the experimental realization and the advantages waveguides have in the fabrication of lattices.

In the third section, quantum light is presented by quantizing the electromagnetic field. We define the principal states and tools used to represent and study the properties of the fields. with special attention to the squeezed state of light, the main state used in this investigation.

In the fourth section, we comment on propagation quantum states using the coupled-mode theory, the definition of topology for photonic systems called topological photonics, and the principal differences between bosonic and fermionic systems.

In the fifth section, preliminary topics about quantum light on photonic and topological systems are discussed in order to fully understand the results and conclusions. This consists on two works where the evolution of squeezed light inside a dimer and a topological lattice is studied. Finalizing by presenting the numerical method used to calculate expectation values.

The last section consists of the setup, results, and conclusions of this investigation. The setup consists of topological states localized on domain walls that through time-dependent Hamiltonian are moved across the system and put next to each other. By injecting squeezed light in these sites it is possible for the light to interact generating interference between them. We study the effects these interactions have on the quantum properties of the squeezed state and the advantages the topology brings against different kinds of disorder.

# Chapter 1

# Topological systems

## 1.1. Introduction to topological systems

A topological insulator has the properties of being an insulator in the bulk while hosting conductive states on the edges, these states are related to a topological invariant defined by the geometry of the wave functions obtained from the periodic (edge-less) system. As long as the topological number remains, the states will possess localization and robustness.
To introduce these systems we start with the quantum hall effect [4]. In this experiment when an electron gas is confined in two dimensions and placed under a strong magnetic field, a current appears on the edges with a conductance quantized in multiples of $e^2/\hbar$. The precision in the measured conductivity was never seen before, this was the beginning of a new area in physics called topological insulators, and later, it even impulsed the redefinition of universal constants [5].
This precise conductivity in the surface (edge) of the system was attributed to the topological quantity called the Chern number [11] defined by the eigenstates of the infinite version of the system. This relation between the appearance of edge states and bulk properties is called the bulk-boundary correspondence. Despite these amazing properties, strong magnetic fields and confined 2D electrons are specific conditions for the phenomena to occur. It was not until 1988 that F. D. M. Haldane [12] proposed a theoretical honey-comb lattice with complex second-neighbor coupling giving a locally magnetic-like phase between sites but a null global magnetic field on each unit cell. Haldane obtained a Chern number related to the surface states just like in the quantum hall effect. Even though this system was not experimentally plausible at the time, the theoretical consequences gave a second kick to topological systems, they are now depending on the configuration and interaction inside the lattice rather than external effects.
Kane and Mele made the next milestone in 2005 [13] when they managed to get helicoidal surface states polarized by their spin. Their system consisted of a honeycomb lattice with spin-orbit interaction, and it made it possible to induce a topological phase without breaking time-reversal symmetry. This system was called the quantum spin hall effect. In 2007, just two years later, it was experimentally realized in HgTe quantum wells [14] setting the

topological insulators as a whole new branch in physics.
Since then, topological systems have been extensively studied in many more dimensions and with different interactions, some examples are the 3D crystals [15], Weyl semimetal [16], Floquet insulators [17] and Non-hermitian systems [18] to mention a few. Even more, the concept of topology has reached beyond crystals and electronic systems. Topological properties have been found in areas like mechanical systems [19], electric circuits [20] and, the focus of this thesis, photonic systems [6, 21], among others.
The following section will briefly introduce topological systems, what defines them, and their properties. To do this, we will focus on defining and calculating the topological properties of the Su-Schrieffer–Heeger (SSH) model. In the end, we define topological states localized in domain walls and a time-dependent SSH model which "moves" the domain wall through the system.

## 1.2. The Su-Schrieffer–Heeger (SSH) model

In condensed matter, a tight-binding model approximates the behavior of a single electron inside a crystal, represented as an array of atoms with some periodicity, as a sum of bound states in each atom with the hopping between them defined by how much the tails of the wave-function between atoms overlap [22] (To be consistent with the vocabulary, from here on, we use the concept of coupling instead of hopping). The electron is only allowed to be on an atom with a probability of jumping to some neighbor proportional to the coupling. Because of the lattice's periodicity, the system's Hamiltonian commutes with the translational operator thus the system's wave function can then be expressed in terms of Bloch waves with the same periodicity as the lattice. By using this transformation, we get to the Bloch-Hamiltonian. Studying the eigenvalues depending on the crystal momentum $\mathbf{k}$ yields the band structure of the system encoding the basic electronic properties [23, 24].
The topological system used in this thesis is the Su-Schrieffer–Heeger model for polyacetylene or SSH model [25, 26]. It corresponds to a dimerized chain with an alternating coupling $u$ and $v$, and a site energy $\varepsilon_0$. It possesses two sites per unit cell where the intercell coupling is $v$ and the intracell coupling is $u$ as shown in figure 1.1.
Considering N unit cells, the tight-binding Hamiltonian is

$$\mathcal{H} = \sum_{i}^{N}[\epsilon_{(2i)}\hat{a}_{2i}^{\dagger}\hat{a}_{2i}+\epsilon_{(2i+1)}\hat{a}_{2i+1}^{\dagger}\hat{a}_{2i+1}]+[u\hat{a}_{2i+1}^{\dagger}\hat{a}_{2i}+v\hat{a}_{2i-1}^{\dagger}\hat{a}_{2i}+h.c.] = \sum_{mn} H_{mn}\hat{a}_{m}^{\dagger}\hat{a}_{n}, \tag{1.1}$$

where $H_{mn}$ is a real matrix with the on-site and coupling coefficients corresponding to the diagonal and off-diagonal components, respectively. $\hat{a}_i$ and $\hat{a}_i^{\dagger}$ are annihilation and creation operators, respectively, for each site index by $i$.

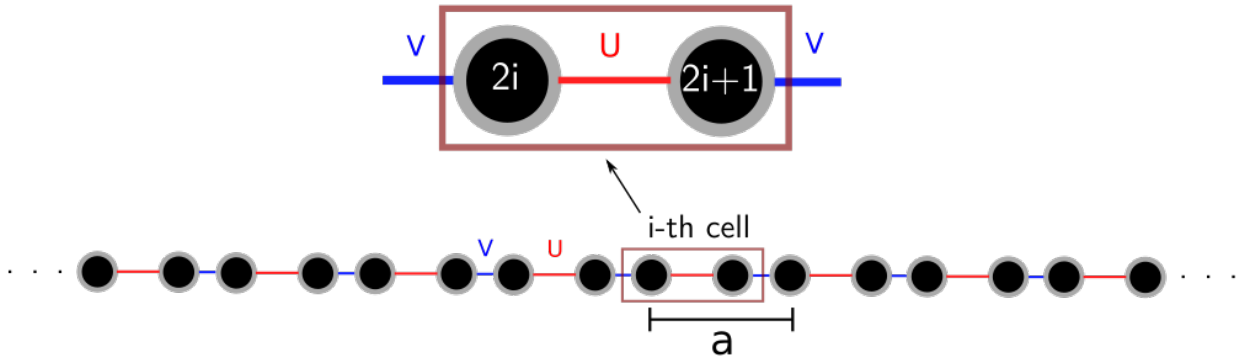


Figure 1.1: The Su-Schrieffer-Heeger (SSH) chain. The unit cell possesses two sites connected by the intra-cell coupling $u$ while each unit cell is connected by the inter-cell coupling $v$. All on-site energies are equal and the periodicity of the lattice is given by a.

The site's energies are equal, $\varepsilon_{2i} = \varepsilon_{2i+1} = \varepsilon_0$. They only represent a shift in the energies which can always be made zero with the correct transformation, thus we can assume, without loss in generality, that $\varepsilon_0 = 0$.

To understand how topological protection arises from symmetry and gives birth to localized edge states, we begin by studying the bulk properties. The following development has been done before in references [27, 28].

We begin by assuming an infinite periodic chain as depicted in 1.1, because translation symmetry allows for Bloch states to be the shared basis with the Hamiltonian, we apply a discrete Fourier transform separating the even and odd sites corresponding to each sub-lattice composing the unit cell.

$$\hat{a}_{2n} = \frac{1}{\sqrt{N}} \sum_k \hat{a}_{2k} e^{ikan} \qquad\qquad \hat{a}_{2n+1} = \frac{1}{\sqrt{N}} \sum_k \hat{a}_{2k+1} e^{ikan}, \tag{1.2}$$

The Hamiltonian in the Reciprocal space is

$$\hat{\mathcal{H}} = \sum_k (u + ve^{ika}) \hat{a}^\dagger_{2k+1} \hat{a}_{2k} + (u + ve^{-ika}) \hat{a}_{2k+1} \hat{a}^\dagger_{2k} = \sum_k \hat{\mathbf{a}}^\dagger_k H(k) \hat{\mathbf{a}}_k, \tag{1.3}$$

where $\hat{\mathbf{a}}_k = (\hat{a}_{2k+1}, \hat{a}_{2k})^t$. The matrix $H(k)$ has the form

$$H(k) = \begin{pmatrix} 0 & (u + ve^{ika}) \\ (u + ve^{-ika}) & 0 \end{pmatrix}, \tag{1.4}$$

$H(k)$ is the square matrix defining each block of the block diagonal matrix $\mathcal{H}$. We calculate the energy bands by solving the eigenvalue problem, directly yielding

$$E(k)_\pm = \pm\sqrt{u^2 + v^2 + 2uv\cos(ka)}, \tag{1.5}$$

each eigenvalue with the associated eigenstates

$$|\pm k\rangle = \frac{1}{\sqrt{2}} \begin{pmatrix} e^{\pm i\phi(k)} \\ 1 \end{pmatrix} \qquad \phi(k) = \arctan\left(\frac{v\sin(ka)}{u + v\cos(ka)}\right). \tag{1.6}$$

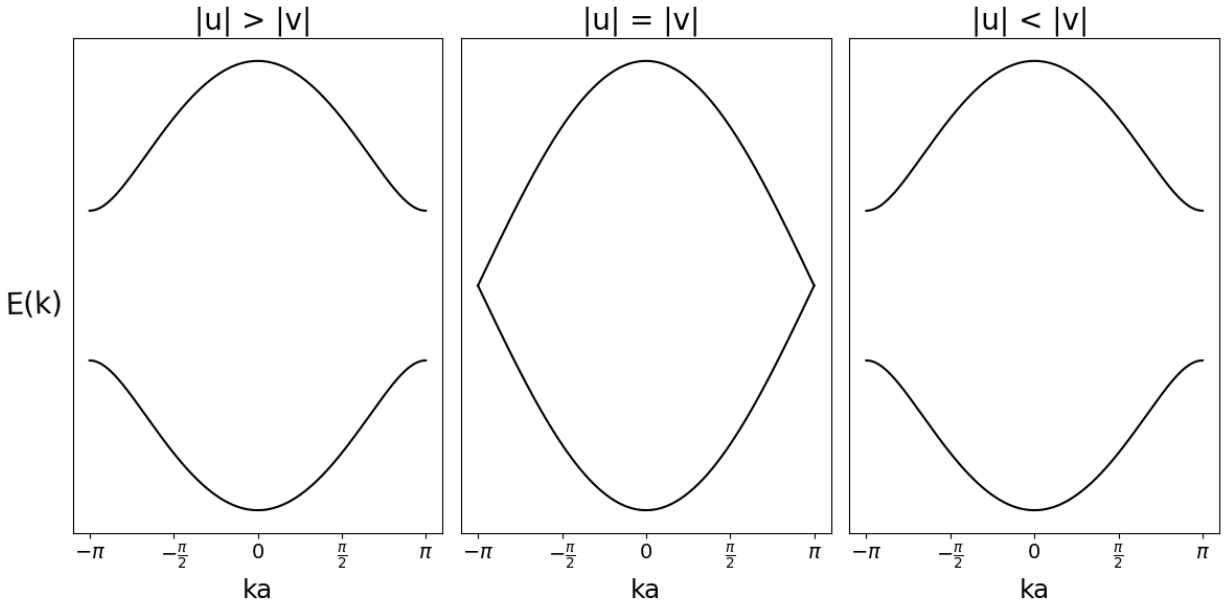


Figure 1.2: Energy bands for different conditions on the coupling. The left panel shows the bands for intra-coupling greater than inter-coupling, the middle panel shows equal coupling and the right panel show the intra-coupling lower than inter-coupling.

From figure 1.2, when $u = v$ we have a metallic model where the energy gap closes and the solutions are plane waves that take arbitrarily low energy to move through the system. For $u \neq v$ there is an energy band gap of size $\Delta = |u - v|$, representing an insulator with states extended across the system.

At first sight, we notice no difference between the cases $|u| > |v|$ and $|u| < |v|$ in the eigenvalues, does that mean both conditions are symmetric? To understand this we introduce the topology and its relation with symmetry. The SSH model possesses chiral symmetry, which is defined for a given Hamiltonian as

$$\hat{\Gamma}\,\hat{\mathcal{H}}\,\hat{\Gamma}^{\dagger} = -\hat{\mathcal{H}}, \tag{1.7}$$

to understand what this symmetry brings we must set the basic properties that the chiral operator satisfies. First, it must be hermitian and unitary, this means that $\hat{\Gamma} = \hat{\Gamma}^{\dagger}$ and $\hat{\Gamma}^2 = 1$ *i.e.*, it has real eigenvalues and leaves the Hamiltonian invariant if applied twice. The second is that it must be local so if we apply it to the unit cell the operator $\hat{\Gamma}$ is block diagonal and can be defined using a local chiral operator acting on the $i$ unit cell. The total chiral

operator can be expressed as a tensorial product of each local chiral operator $\hat{\gamma}_i$

$$\hat{\Gamma} = \hat{\gamma}_1 \otimes \hat{\gamma}_2 \otimes \cdots = \bigoplus_{i=1}^{N} \hat{\gamma}_i, \tag{1.8}$$

with $N$ the number of unit cells in the system. This means that the chiral operator $\hat{\Gamma}$ satisfies, in the real space, $\langle 2m'+1|\,\hat{\Gamma}\,|2m+1\rangle = 0 = \langle 2m'|\,\hat{\Gamma}\,|2m\rangle$ if $m \neq m'$, and as expected there are no even-even and odd-odd site transitions for these type of Hamiltonian. Since the local chiral operator acts on the unit cell, the Bloch-Hamiltonian satisfies

$$\hat{\gamma} H(k) \hat{\gamma}^{\dagger} = -H(k), \tag{1.9}$$

It can also be easily checked that the energy spectrum of a system with chiral symmetry is symmetrical, meaning that for an eigenstate $|\psi_n\rangle$ and energy $E_n$ there is another state with energy $-E_n$. This means that if the eigenvalue of energy $E_n = 0$ exists, it is, at least, double degenerate.

Chiral symmetry is preserved when adding coupling disorder and broken when adding on-site disorder. This is because when adding on-site disorder the Hamiltonian stops satisfying the relation in equation (1.7). To understand how this comes to be we start with the Bloch Hamiltonian, which, as a 2x2 system, can be decomposed as a sum of the known Pauli matrices $(\sigma_x, \sigma_y, \sigma_z)$ as

$$H(k) = d_x(k)\sigma_x + d_y(k)\sigma_y + d_z(k)\sigma_z = \vec{d}(k) \cdot \vec{\sigma}, \tag{1.10}$$

where, for our system in 1.4, each component take the values $d_x = u + \cos(2ka)$, $d_y = v\sin(2ka)$, $d_z = 0$. The local 2x2 chiral operator can be expressed as a Pauli matrix which fulfills all the properties mentioned before

$$\hat{\gamma} = \sigma_z = \begin{pmatrix} 1 & 0 \\ 0 & -1 \end{pmatrix} \tag{1.11}$$

The Hamiltonian then must fulfill the symmetry condition (1.9). Applying the transformation yields that

$$\begin{aligned} \gamma H(k) \gamma^{\dagger} &= \sigma_z d_x(k) \sigma_x \sigma_z^{\dagger} + \sigma_z d_y(k) \sigma_y \sigma_z^{\dagger} + \sigma_z d_z(k) \sigma_z \sigma_z^{\dagger} \\ &= -(d_x(k)\sigma_x + d_y(k)\sigma_y) + d_z(k)\sigma_z \end{aligned} \tag{1.12}$$

The condition in equation (1.9) is only fulfilled if $d_z = 0$ which translates in our initial Hamiltonian (1.1) as having equal site energies (any non-zero value of the on-site energy can be made zero by a simple shifting in the energies proportional to the identity). How does this come into place with the topology?

To understand this, we introduce a topological invariant, the winding number, which is the normalized version of the Zak phase [29]. The winding number can be expressed using the

eigenstates as a closed integral in the Brillouin zone of the following form

$$\zeta = \frac{1}{2\pi i} \oint \langle u(k)| \frac{\partial}{\partial k} |u(k)\rangle \, dk, \tag{1.13}$$

this is an integral in a closed path of the eigenvectors through the momentum space. Using the states in (1.6), it can be rewritten using $\phi(k)$ and integrating a closed loop between $[\frac{-\pi}{a}, \frac{\pi}{a}]$ in the reciprocal space as

$$\zeta = \frac{1}{2\pi} \int_{-\pi/a}^{\pi/a} \frac{\partial}{\partial k}(\phi(k))dk, \tag{1.14}$$

which can be calculated for all conditions of the coupling. The relation $|v| > |u|$ yields $\zeta = 1$, $|u| > |v|$ yields $\zeta = 0$, and for $|u| = |v|$ it crosses the origin of the plane where the function is undefined. The difference in the results is due to a branch crossing of the function $\phi(k)$. For $|v| > |u|$, it only crosses one time meaning $\zeta = 1$. For $|u| > |v|$, it crosses an even amount of times (with opposite value) or zero, depending on the coupling difference, resulting in $\zeta = 0$. This is where the difference between coupling conditions appears, the eigenstates tell us that there is a topological difference for each condition.

Two topological phases can be identified by the same invariant if by continuously changing the parameters, we can go from one to the other without closing the energy gap ($|u| \neq |v|$). This is not the case for the SSH system as we have two topological phases related to two different topological invariants. We will call the topological phase, trivial for $\zeta = 0$ and non-trivial or topological for $\zeta = 1$. To go from one to the other it is necessary to close the energy gap, so we have a topological transition.

As we talked about before, having different on-site energies on each sub-lattice breaks the chiral symmetry. This translates into $\phi(k)$ having an extra term that lifts the function in the $k$ space and it no longer crosses the branch, giving a zero winding number and breaking the topology. This is the relation between the symmetry and the topological number, breaking one breaks the other.

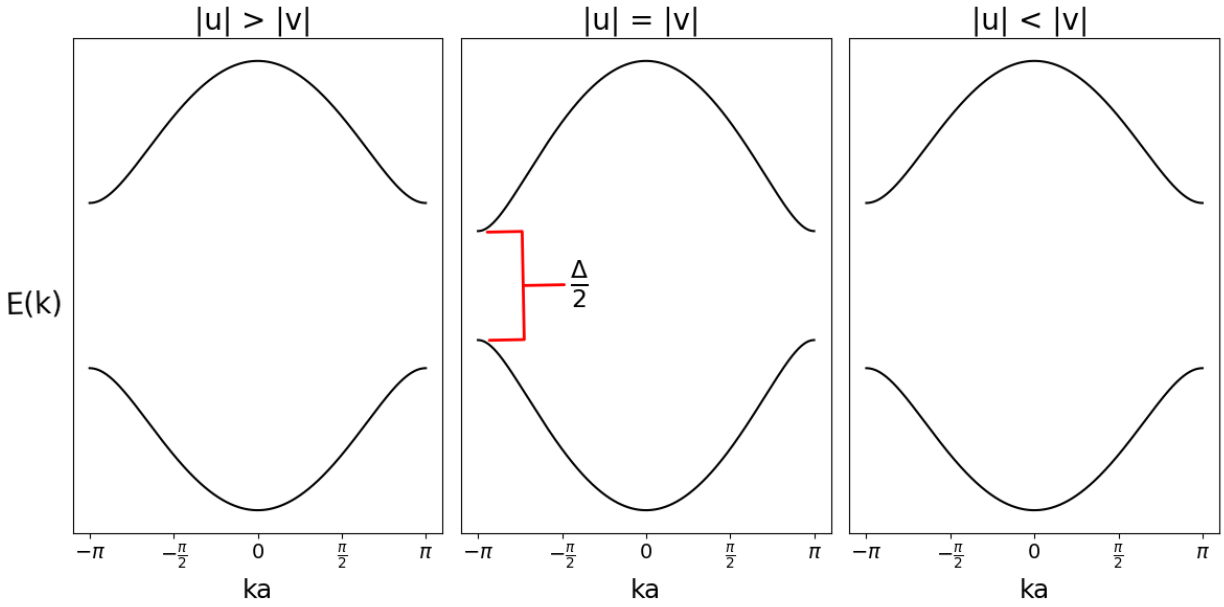


Figure 1.3: Energy bands for different coupling conditions when adding an on-site energy difference $\Delta$ between sites. The system can go between both coupling conditions without closing the gap, meaning there is no topological transition and the system is always in a trivial phase.

If we add an onsite difference to one of the sub-lattices as $\epsilon_{2n} = \Delta$, the energy gap opens up for any values of $u$ and $v$, as shown in figure 1.3, and we can go adiabatically from one condition of the couplings to the other without closing the energy gap, making both topological phases equal and trivial.

The appearance of a non-zero topological invariant will have consequences and, as we will see, this number is linked to the emergence of edge states in the system. Assuming stationary states as $\phi_n = \psi_n e^{iE_n t}$ and solving the eigenvalue problem

$$E_m \psi_m = \sum_n H_{mn} \psi_n, \tag{1.15}$$

each one of these modes will have a wave function distributed across the sites of the chain. We are interested in the spatial distribution across the chain of the eigenstates with zero energy, which are states outside of the bulk bands. We introduce the inverse participation ratio (IPR) defined as

$$IPR = \frac{(\sum_n |\psi_n|)^2}{\sum_n |\psi_n|^4} \tag{1.16}$$

This quantity helps us understand how localized are the states across the lattice. For extended states, the IPR tends to 1, while for localized states the IPR tends to 0.

We now study a finite SSH system with 30 sites and couplings $u = 2$, $v = 4$ in order to understand the properties of topological states.

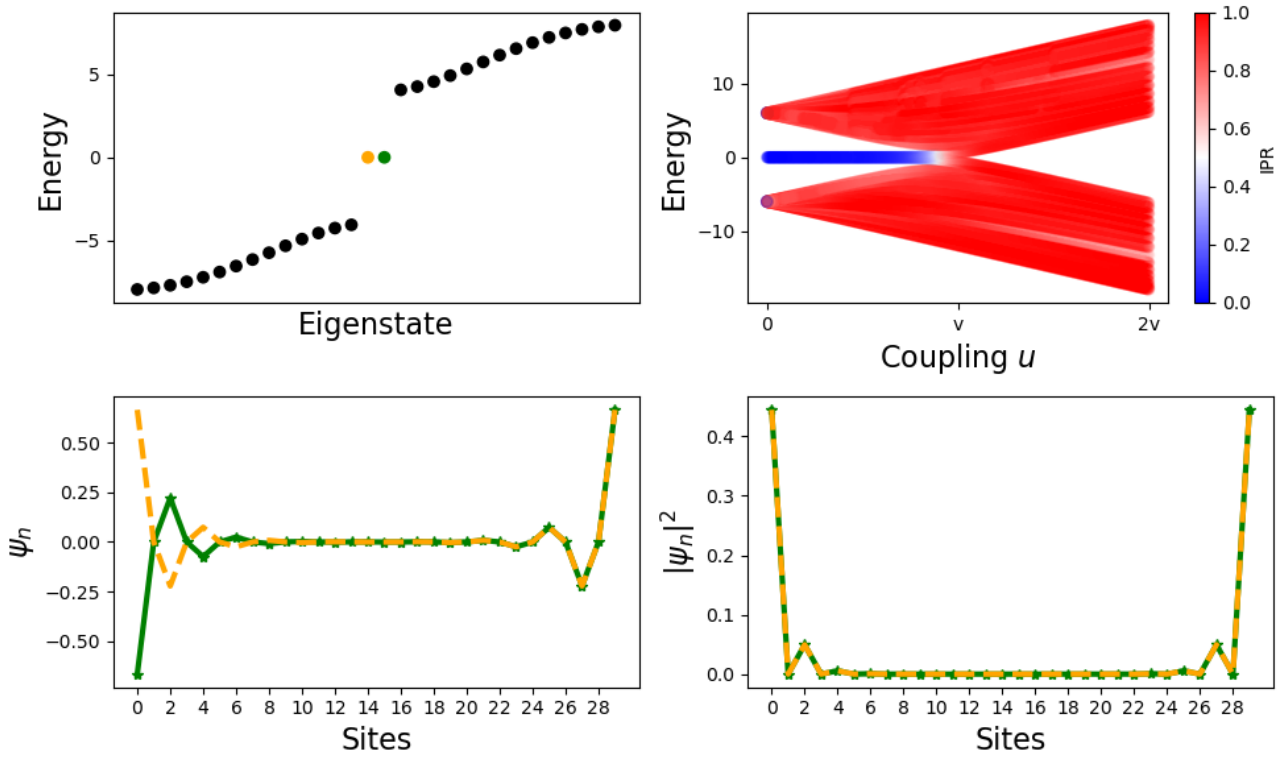


Figure 1.4: SSH model of 30 sites with coupling $u = 2$ and $v = 4$. The top left shows the energy spectrum with the topological states highlighted. The top right shows the energy spectrum as a function of the coupling $u$. When the condition $|u| < |v|$ is met, localized zero energy states appear. The bottom left and right panels show the amplitude and squared modulus, respectively, distributions across the lattice for the zero energy state which are exponentially localized on the edges with opposite phases.

The top right panel of figure 1.4 shows that when $u > v$, there are no states with zero energy meaning that the edge state disappears, which is the condition where the topological number is zero. On the contrary, for $v > u$ the topological number is one, and the zero energy states appear localized on the edges. This is a manifestation of the bulk-boundary relation where we can get information from the edges by studying the properties of the bulk.

In the same figure, the wave function of the zero energy states is exponentially localized at both edges. They also possess sub-lattice polarization, where the left and right edge state decay through even and odd sites, respectively.

Another property these states possess is the robustness against coupling disorder. This is because the topological invariant is independent of the coupling values and, as long as the ratio between them is maintained in the topological condition, it will remain. The topological states we just showed are called symmetry-protected edge states because they will prevail against a disorder that does not break the symmetry. To visualize the robustness and its

limits, coupling and on-site energy disorder are added as

$$\begin{aligned} \Delta &= [-\delta, \delta] \cdot |u - v| \\ u' &= u + \Delta \\ v' &= v + \Delta \\ \epsilon'_{2n} &= \Delta \end{aligned} \tag{1.17}$$

where $[-\delta, \delta]$ is a random uniform distribution limited by $\delta$. We add coupling and on-site disorder separately in order to compare the effect on the edge states, When $\delta = 1$ the disordered couplings can switch ratios which is the limit to study before a topological transition. We plot the energy spectrum as a function of the amount of disorder.

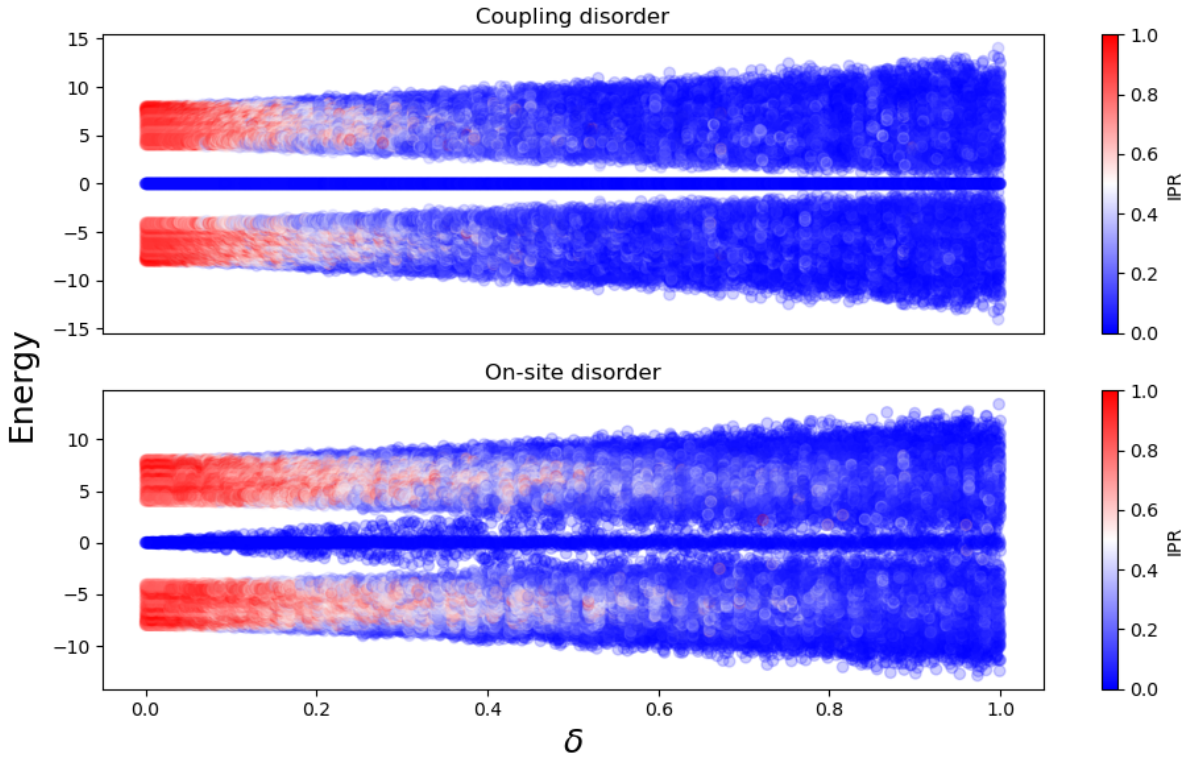


Figure 1.5: Energy spectrum as a function of the disorder magnitude $\delta$. The top panel shows the robustness of the zero energy states when adding coupling disorder, maintaining the zero states inside the energy gap for a considerable disorder. In the bottom panel, little amounts of disorder affect the states and their energy, this showcases the weakness against on-site disorder. At increasing disorder Anderson's localization arises, explaining the low IPR.

Adding onsite disorder break the zero energy states, moving their energy as shown in figure 1.5. Adding the same amount of disorder to the coupling preserves them because of the topological protection and they remain pinned at zero. We have shown, in the finite SSH,

the dependence of the appearance of edge states to the topological condition. The states persist against symmetry-preserving disorder, which in this case is coupling disorder..

## 1.3. Localized states in domain walls

We now know that the SSH model has two edge states (supported on both edges) of zero energy which exist within the band gap and are protected by chiral symmetry. This is not the whole history, in a more general approach, a topological state can form in the boundaries between systems with different topological phases [27]. The junction between systems is called a domain wall, for example, the edge of the SSH can be considered a domain wall separating the SSH from the vacuum and because of it, it can host a topological state given the right condition. This can also happen inside lattices, an example of a domain wall inside the SSH is shown in figure 1.6. To create it we attach two SSH models using an extra site and the coupling $u$, this way we can maintain the topological geometry on both systems and create a topological localized state in the junction.
The state in the domain wall will possess the properties of the edge state *i.e.* zero energy, exponential localization to both sides of the site, and robustness against coupling disorder.

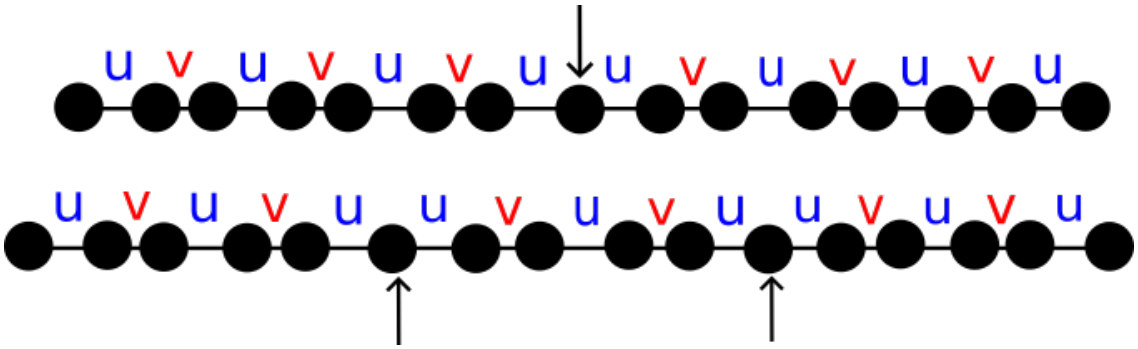


Figure 1.6: Example of SSH chains with domain walls pointed by the arrow. The upper image shows a single domain wall while the lower image shows two domain walls. Both systems have topological localized states on the domain walls.

By joining two SSH models of $N$ and $M$ unit cells using an extra site, we get a localized state in the $2N+1$ position. The Hamiltonian describing this system is

$$\mathcal{H} = \sum_{i=0}^{N}( u\hat{a}^{\dagger}_{2i+1}\hat{a}_{2i} + v\,\hat{a}^{\dagger}_{2i-1}\hat{a}_{2i}) + \sum_{j=N+1}^{M} +(v\,\hat{a}^{\dagger}_{2j+1}\hat{a}_{2j} + u\,\hat{a}^{\dagger}_{2j-1}\hat{a}_{2j}) + h.c., \tag{1.18}$$

where $\hat{a}_{i<0} = \hat{a}_{i>2M} = 0$. It is possible to have more than one domain wall per system and, by properly adjusting the system's geometry, as depicted in the bottom image of figure 1.6, each domain wall will possess a localized topological state [30]. Creating a chain hosting $w$ domain walls by joining SSHs of $N$ unit cells yields a full system of size $2N(w+1)+w$.

To study the state of the domain wall, we use a finite SSH model of 31 sites, couplings $v = 4$ and $u = 2$, and a domain wall in site 15.

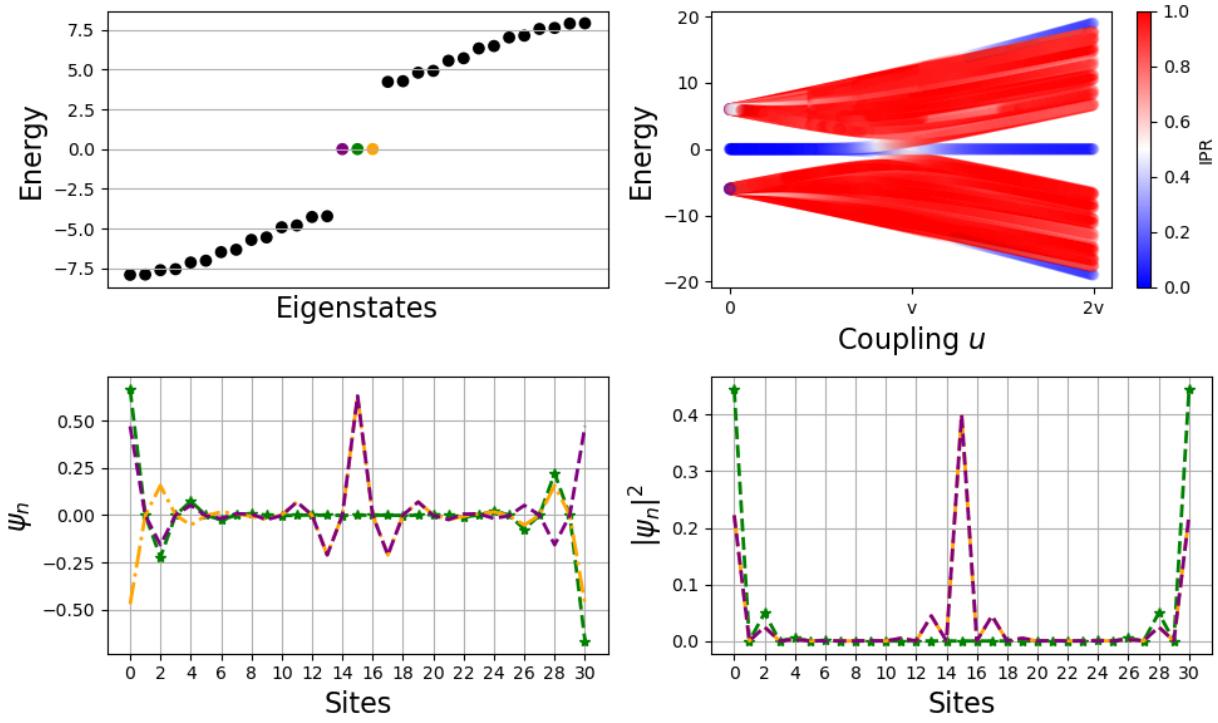


Figure 1.7: Top left shows the energy spectrum of the SSH with 31 sites, couplings $u = 2, v = 4$, and a domain wall on site 15. The top right is the energy spectrum as a function of the coupling $u$, zero energy localized states persist for both coupling conditions. Bottom left and right show the amplitude and modulus squared, respectively, of the highlighted states in the energy spectrum. Two of the states are localized on the domain wall and they all have weight on the edges.

From the top right panel in figure 1.7, we can see that the condition $v > u$ hosts zero energy states like the SSH without the domain walls. For $u > v$ this changes and a zero energy state appears but, this state is not topological because the system is not in a topological phase, it corresponds to a trivially localized state due to the coupling, which can be thought of as a coupling impurity. As seen on the bottom panels of 1.7, the state localized on the domain wall will gain weight on the nearest sites hosting a state of the same energy, this is known as fractioning of the charge or the hybridizing of the state [31, 32].

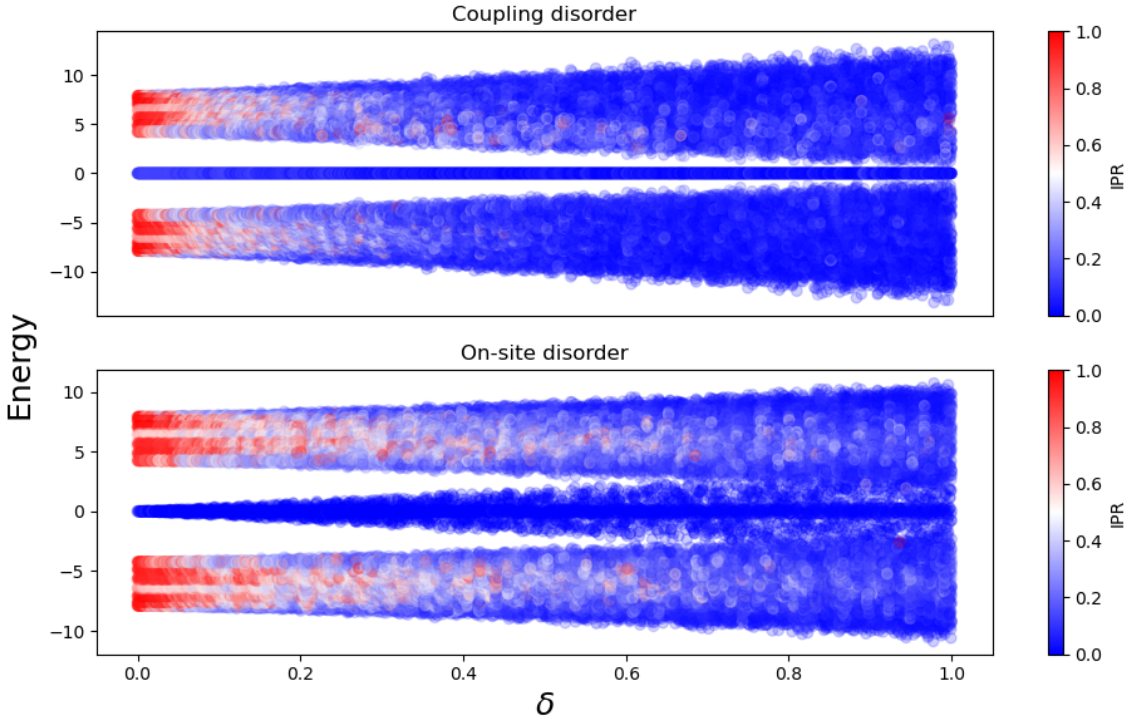


Figure 1.8: Energy spectrum as a function of the disorder with $v = 4$ and $u = 2$. In the top panel, the effect of coupling disorder is shown, and, as the normal SSH, the zero energy states persist at increasing disorder. On the contrary, on-site impurities break the topology and states, moving their energies. As the disorder is introduced, Anderson's localization arises explaining the low IPR.

In figure 1.8 is plotted the energy spectrum as a function of both types of disorder, with the same form as (1.17). The states of zero energy remain at that energy for a great amount of coupling disorder, proof of the robustness. On the contrary, adding the same amount of on-site disorder moves the energies of the edge states, and they start to break. The domain wall located between two couplings $u$ only hosts topological states with zero energy, just like the topological edge states, meaning that an excitation of the site will mostly stay in it, as the dispersion to adjacent sites is low.

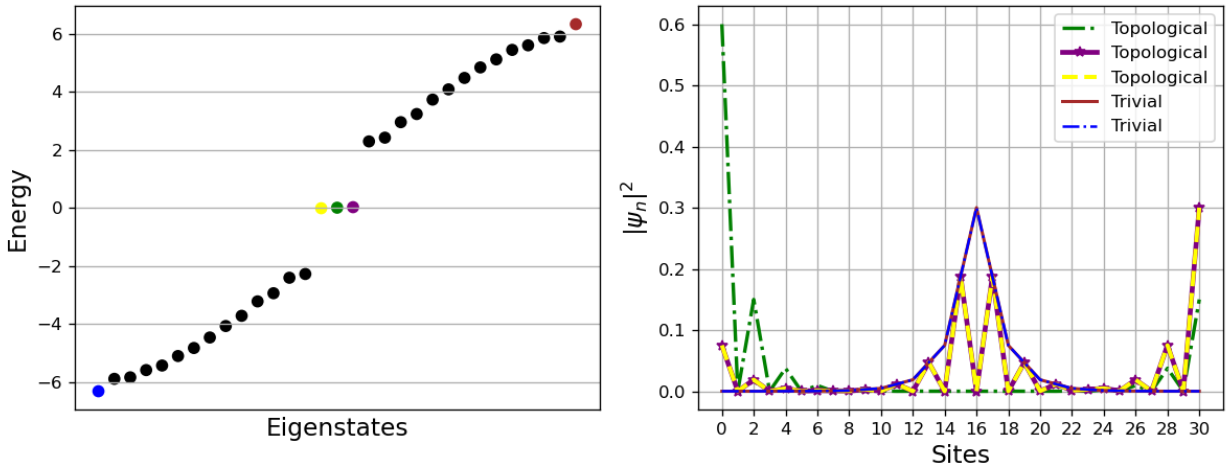


Figure 1.9: The left panel shows the energy spectrum of SSH with a domain wall between two couplings $v$ where $v = 4$ and $u = 2$. The right panel shows the modulus squared on each site for the eigenstates of the highlighted topological and trivial states. The zero energy states are exponentially localized on the sub-lattice around the position of the domain wall. On the other hand, the trivial states are exponentially localized on the domain wall.

It is also possible to have a domain wall between two couplings $v$ which will host topological states, however, the shape of the state is also different. This is due to the forming of an effective site consisting of the domain wall and both of its neighbors, the wave function of the topological state is localized on the sites adjacent to the domain wall, as seen in 1.9. Alongside the topological state, there are two trivial states which are localized on the domain wall and adjacent sites. This implies that exciting the topological state will also excite the trivial states generating a coupling between them. This coupling between states is not wanted and, as we will see in Chapter 5, it makes the domain wall unsuitable for the investigation but we mention it here for completeness.

## 1.4. Moving domain walls using a time-dependent Hamiltonian

We now introduce a local time-dependent SSH model. This system possesses couplings around specific sites which depend on the dynamical coordinate. Varying the coupling allows us to "move" the domain wall to a different position across the system. If we want to maintain the localization and topological properties of the state on the moving domain wall, the function defining the modulated coupling must be smooth and continuous while also maintaining the topological geometry at the end, as depicted in Figure 1.10, otherwise the state couples to the bulk and scatters. Both the speed of the modulation and the initial band gap of the system size define the accuracy of the modulation and how much scattering to the bulk is produced. A slower modulation accepts a lower band gap while a bigger band gap accepts

a faster modulation. Both conditions come into play when defining a good modulation that diminishes the coupling to the bulk but takes into account the limits of experimental realizations.

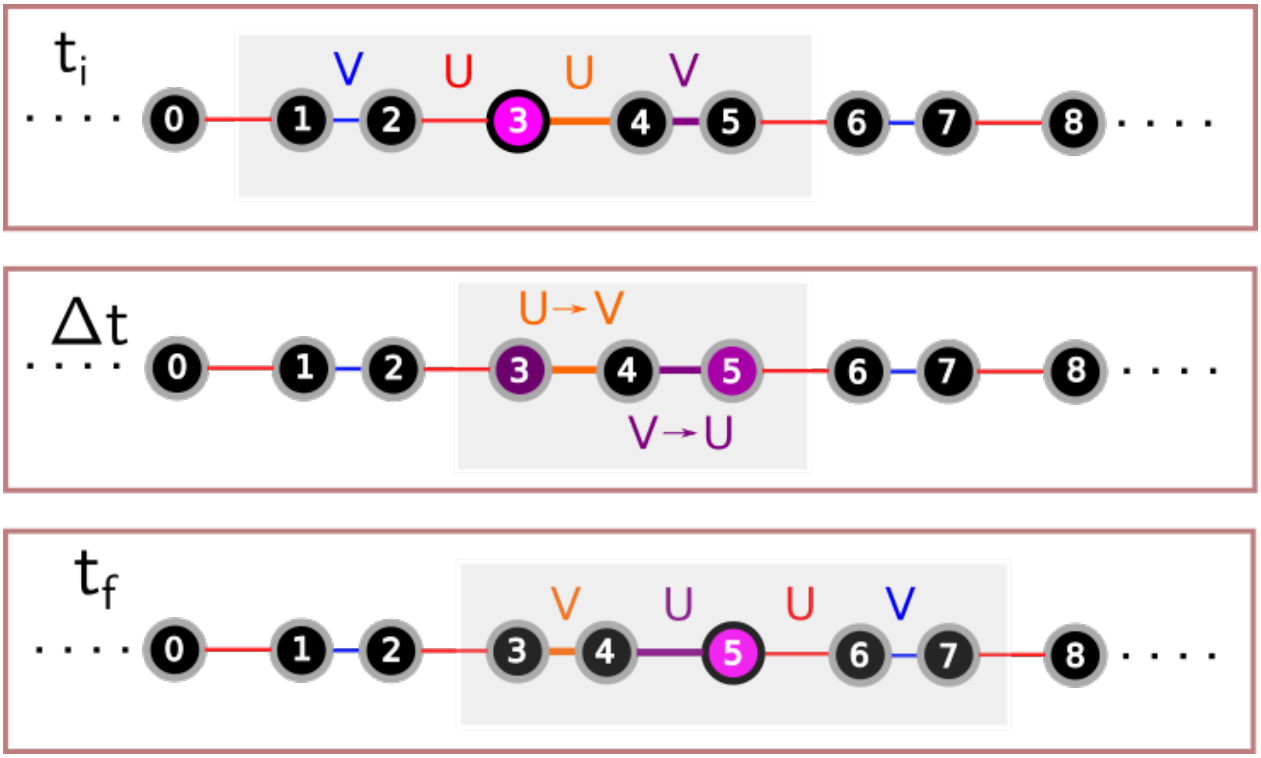


Figure 1.10: Example of how to move the domain wall. At the beginning of the modulation, the domain wall is located on site 3, highlighted with pink. By changing the orange and purple couplings, as depicted in the middle panel, the domain wall can be "moved" to two sites to the right. At the end of the modulation, the domain wall is located at the highlighted site 5 and the system is still in a topological phase.

In order to maintain the topological phase of the system, the domain wall can only be moved to its next neighbor, a pictorial representation of the modulation is shown in 1.10. As talked before, the topological domain wall of interest must be adjacent to two couplings $u$, this is just two SSH models attached through an extra site using coupling $u$.
To move the domain wall, we assign a time dependence to each coupling $u(t)$ and $v(t)$. These functions have to be smooth and continuous while also beginning and finalizing the evolution following

$$u(t_0) = u \qquad v(t_0) = v$$
$$u(t_f) = v \qquad v(t_f) = u$$

This maintains the geometry and preserves the topological phase. The modulation shown in figure 1.10 can be done repetitively, moving the domain wall along the lattice. To maintain the

geometry, the domain wall can only be moved to the next-adjacent site in each modulation. In practice, time-dependent coupling is rare in condensed matter as the lattices, dictated by nature, are in equilibrium which usually means a fixed coupling given the geometry of the lattice. As we will see, photonic systems allow us to create and study these types of systems in a relatively easy way. More details about this modulation and how it looks in waveguides will be discussed in Section 5.

# Chapter 2

# Photonic systems

## 2.1. Introduction to photonic systems

The area of photonics focuses on studying the propagating of light through different mediums and geometries, understanding its origin, manipulation, and detection. From an experimental point of view, photonics systems are characterized by using optical fibers, lasers, detectors, quantum electronics, fibers, and materials. With uses in technology for areas such as computation, communication, information [33] and biology [34] to mention a few.
In this thesis, our study is made on waveguide systems defined in the coupled mode theory (CMT) approximation. These systems are typically made by locally changing the refractive index inside a medium, confining the light to travel inside it [35]. We must mention that the coupled mode approximation is not only defined to this kind of system, coupled optic oscillators and cold atoms lattices can also be studied [36, 37].
A characteristic of light traveling through waveguides is the reproduction of the results of systems defined in other areas of physics (providing the correct approximations) and, as we will see, the coupled mode theory works at the same level of approximation as the tight-binding theory introduced in Chapter 1, and as such, photonic lattices can present topological effects.

## 2.2. Coupled mode theory

In the following section, we will formulate and describe the basics of the coupled mode approximation. This theory has been extensively used and studied in optics to study periodic systems [38]. To derive the coupled mode equations, we start with the Maxwell equations in

materials

$$\vec{\nabla} \cdot \vec{D} = \rho \tag{2.1}$$
$$\vec{\nabla} \cdot \vec{B} = 0 \tag{2.2}$$
$$\vec{\nabla} \times \vec{E} = -\frac{\partial \vec{B}}{\partial t} \tag{2.3}$$
$$\vec{\nabla} \times \vec{H} = \vec{J} + \frac{\partial \vec{D}}{\partial t}, \tag{2.4}$$

with the constitutive relations:

$$\vec{D} = \epsilon_0 \vec{E} + \vec{P} \tag{2.5}$$
$$\vec{H} = \frac{\vec{B}}{\mu_0} - \vec{M} \tag{2.6}$$

We now assume materials where there is no charge accumulation, no current, and no magnetization, thus we have $\rho = 0$, and $\vec{J}, \vec{M} = 0$. In classical light, the polarization vector $\vec{P}$ represents the effects of the medium on the light dynamics. In a dielectric, the induced polarization can be expressed as a Taylor expansion of the electric field.
In general, when considering a non-linear response, the polarization is expressed in higher terms of the expansion. For more information on this topic, we recommend [39] which also develops the coupled mode theory taking into account non-linear effects. In this work, we only consider the linear response *i.e.*, $\vec{P} \propto \vec{E}$, where the proportional factor is called electric susceptibility which is a tensor depending on the medium's properties. We will work on glass-like materials that are both isotropic and homogeneous. The susceptibility is then a constant fulfilling

$$\vec{P} = \epsilon_0 \chi^{(1)} \vec{E}^{tot}, \tag{2.7}$$

where $\chi^{(1)}$ is the first order electric susceptibility of the medium and $\vec{E}^{tot}$ is the total electric field inside the medium.
Combining the Maxwell equations, the electric field satisfies the following

$$\vec{\nabla} \times \vec{\nabla} \times \vec{E} = \vec{\nabla} \cdot (\vec{\nabla} \vec{E}) - \nabla^2 \vec{E} = -\mu_0 \epsilon_0 \frac{\partial^2 \vec{E}}{\partial t^2} - \frac{\partial^2}{\partial t^2} \left( \frac{\vec{P}}{\epsilon_0 c^2} \right). \tag{2.8}$$

For materials where the permittivity depends on the spatial coordinates $\epsilon = \epsilon_0 \left(1 + \chi^{(1)}(x, y, z)\right) = \epsilon(x, y, z)$, and can be related to the refractive index as $\epsilon = n^2(x, y, z)$, we arrive to the relation: $\vec{\nabla} \cdot \vec{D} = 0 = \vec{\nabla} \cdot (\epsilon \vec{E}) = (\vec{\nabla} \epsilon \cdot \vec{E} + \epsilon \vec{\nabla} \cdot \vec{E})$. Using this we get the general wave equation

$$\nabla^2 \vec{E} - \frac{1}{c^2} \frac{\partial^2 \vec{E}}{\partial t^2} = -\vec{\nabla} \left( \vec{E} \cdot \frac{\vec{\nabla} \epsilon}{\epsilon} \right) + \frac{\partial^2}{\partial t^2} \left( \frac{\vec{P}}{\epsilon_0 c^2} \right). \tag{2.9}$$

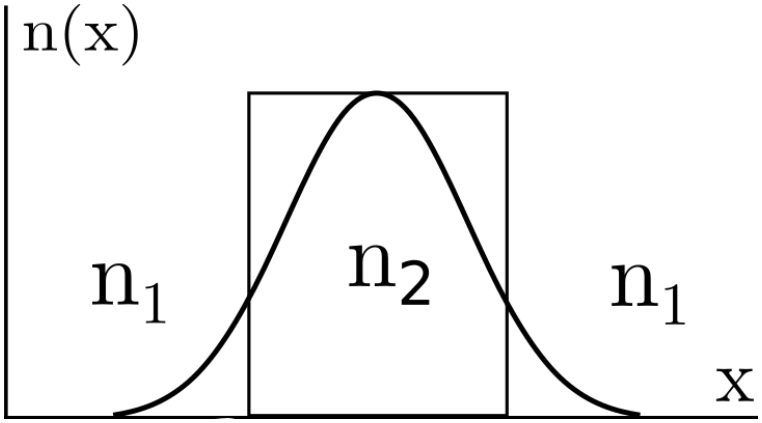


Figure 2.1: Representation of a single waveguide in a medium with the shape of its fundamental mode. Where the refractive index have the relation $n_2(x, y, z) = n_1 - \Delta n(x, y, z)$

We now consider two approximations for geometries like figure 2.1, where the change of refraction index is small. The first is called weak guidance approximation, which states that locally changing the refractive index inside a medium by a small amount $\Delta n(x, y, z)$ implies that

$$\begin{aligned}\vec{\nabla}(\ln n_2^2) &= \vec{\nabla}\left(2\ln\left(n_1^2 - 2n_1\Delta n + (\Delta n)^2\right)\right.\\ &= \frac{4n_1\vec{\nabla}(\Delta n)}{n_1 + 2n_1\Delta n} \approx \frac{\vec{\nabla}(\Delta n(x, y, z))}{n_1} \to 0\end{aligned}$$

causes the gradient of the logarithm of the permittivity $\vec{\nabla}(\ln(\epsilon)$ to tend to zero as $\Delta n \to 0$. This neglects the first term of the right side in (2.9) and doing this uncouples the polarizations of the electric field and each one evolves independently.

The second is called the paraxial approximation, it is applied to the injected light stating that light enters the medium perpendicular to the change of refraction index and the wave vector in the injected direction is much greater than the transversal directions ($k_z \gg k_{x,y}$), *i.e.*, we are focusing the light (lasers in most cases) through the "entrance" of the waveguide, not the sides and the solution is of the form $\vec{E} = \vec{E}(x, y, z)e^{ik_z z}$. This also makes the second derivative of the electric field with respect to the propagation variable negligible.

Using the weak guidance approximations on equation (2.9) and setting the parallel component to $\hat{z}$, we now separate the Laplacian as $\nabla^2 = \nabla_{\parallel}^2 + \nabla_{\perp}^2 = \frac{\partial^2}{\partial z^2} + (\frac{\partial^2}{\partial x^2} + \frac{\partial^2}{\partial y^2})$ yielding

$$\frac{\partial^2\vec{E}}{\partial z^2} + \left(\frac{\partial^2}{\partial x^2} + \frac{\partial^2}{\partial y^2}\right)\vec{E} - \frac{1}{c^2}\frac{\partial^2\vec{E}}{\partial t^2} = \frac{\partial^2}{\partial t^2}\left(\frac{\vec{P}}{\epsilon_0 c^2}\right). \tag{2.10}$$

Considering a single waveguide, as depicted in figure 2.1, where the solution can be expressed as a sum of the normal modes with both amplitude and polarization inside the function

$\vec{f}(x,y,z)$, the solution for equation (2.10) can be expressed as

$$\vec{E}(\vec{r},t) = \sum_j \vec{f_j}(x,y,z)e^{i(k_j z - \omega_j t)} + c.c., \qquad \vec{P} = \epsilon_0 \chi^{(1)}(x,y,z)\vec{E} \tag{2.11}$$

The polarization $\vec{P}$ takes this form because we assume there is no extra electric field except the one inside the waveguide. Replacing in equation (2.10) and that $\frac{\partial^2 \vec{f}}{\partial z^2}(x,y,z) \approx 0$ due to the paraxial approximation, yields

$$2ik_j \frac{\partial \vec{\mathbf{f}}}{\partial z}(x,y,z)e^{i(k_j z - w_j t)} + \left[\frac{\partial^2}{\partial x^2} + \frac{\partial^2}{\partial y^2} - 2\frac{k_j^2}{n_1}\Delta n(x,y,z)\right]\vec{\mathbf{f}}(x,y,z)e^{i(k_j z - w_j t)} = 0, \tag{2.12}$$

where $k_0 = \omega_j/(c\sqrt{\epsilon_0})$ and $k_j = n_1 k_0$. Equation 2.12 represents the evolution of the light inside a single waveguide.

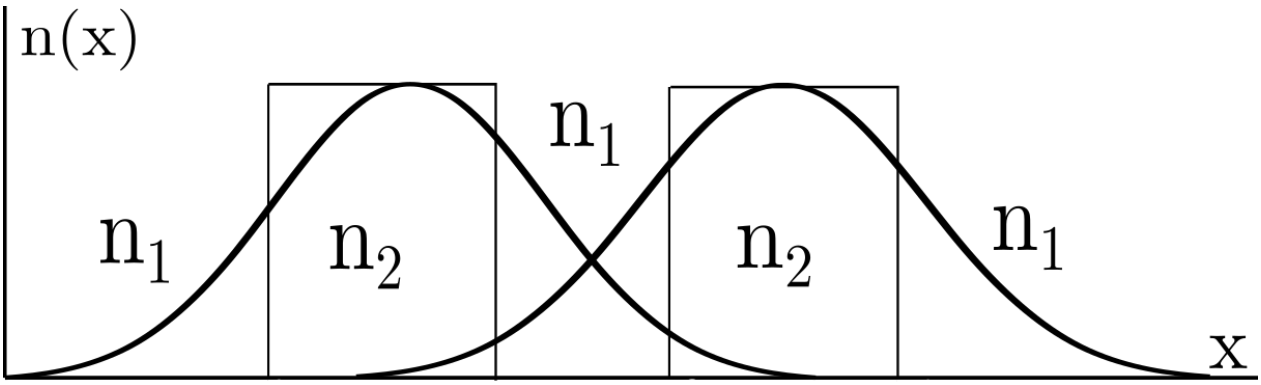


Figure 2.2: Two adjacent waveguides with their fundamental modes overlapping.

We now turn to define the evolution of the electric field for two adjacent waveguides, depicted in figure 2.2, with the same refractive index $n_2$ in a medium with refractive index $n_1$. To do this, we assume that the shape's evolution of each mode remains the same throughout the evolution but it can variate in amplitude represented as

$$\vec{f_j}(x,y,z) = \vec{f_j}(x,y)a_j(z), \tag{2.13}$$

This assumption can be made because by tuning the injecting light in a waveguide, it is possible to select which mode to excite. The excited mode will define all the evolution depending on the initial conditions of the light. The function $f_j(x,y)$ fulfills the mode equation:

$$\left[\frac{\partial^2}{\partial x^2} + \frac{\partial^2}{\partial y^2} - 2\frac{k_j^2}{n_1}\Delta n(x,y,z)\right]\ \vec{f_j}(x,y) = 0 \tag{2.14}$$

and the solution for the electric field in each waveguide $m$ is

$$\vec{E}_m(\vec{r},t) = \sum_j \vec{f}_{m,j}(x,y)a_{m,j}(z)e^{i(k_j z - \omega_j t)} + c.c. \tag{2.15}$$

Now, we calculate the amplitude evolution of light traveling in a waveguide that is adjacent to another waveguide; for this, we study the effects on waveguide 1 (left side) to make it easier to understand. The results are later generalized to an array of waveguides and are independent of the ones chosen initially. The left side of equation (2.10), after inserting in (2.15) for $m = 1$, yields

$$\frac{\partial^2 \vec{E}_{1,j}}{\partial z^2} = \left[2ik_j \frac{\partial a_{1,j}}{\partial z} - k_z^2 a_{1,j}(z)\right] \vec{f}_{1,j}(x,y) e^{i(k_j z - w_j t)} + c.c. \tag{2.16}$$

$$\frac{1}{c^2}\frac{\partial^2 \vec{E}_{1,j}}{\partial t^2} = -\frac{\omega_j^2}{c^2} \vec{f}_{1,j}(x,y) a_{1,j}(z) e^{i(k_j z - \omega_j t)} + c.c., \tag{2.17}$$

where we used that $\frac{\partial^2 a_{1,j}}{\partial z^2} \approx 0$ due to the paraxial approximation.
To express the polarization, we use the total electric field on the waveguide; for this, we consider the electric field coming from waveguide 2 (right side). Assuming a linear polarization response and that the field in each waveguide possesses the same propagation constant and frequency we have that the total electric field on waveguide 1 is:

$$\vec{E}_{1,j}^{tot} = \vec{E}_{1,j} + \vec{E}_{2,j} = \left[\vec{f}_{1,j}(x,y) a_{1,j}(z) + \vec{f}_{2,j}(x,y) a_{2,j}^{(1)}(z)\right] e^{i(k_j z - \omega_j t)} + c.c. \tag{2.18}$$

where $a_{2,j}^{(1)}$ is the amplitude of the field of waveguide 2 inside waveguide 1, which can be redefined as the amplitude inside waveguide 2 multiplied by a constant lower than 1, $a_{2,j}^{(1)} = \alpha a_{2,j}$ with $\alpha < 1$. The polarization takes the form

$$\frac{\partial^2}{\partial t^2}\left(\frac{\vec{P}}{\epsilon_0 c^2}\right) = -\frac{\omega_j^2}{c^2} \chi_{1,j}^{(1)} \vec{E}_{1,j}^{tot}, \tag{2.19}$$

where $\chi_{1,j}^{(1)}$ is the first-order electric susceptibility of the waveguide 1 and mode $j$. Inserting equations 2.18 and 2.19 into (2.9) yields

$$2ik_k \frac{\partial a_{1,j}}{\partial z} \vec{f}_{1,j} + \frac{\omega_j^2}{c^2} \chi_{1,j}^{(1)} \vec{f}_{2,j} \alpha a_{2,j} = 0. \tag{2.20}$$

To get rid of the mode shape dependence, we multiply by $f_{1,j}^*$ and integrate in the x-y plane. We define the power in the waveguide 1 of mode $j$ as $P_1^{(j)}$, and the coupling matrix elements between the two waveguides of mode $j$ as $V_{1,2}^{(j)}$ :

$$P_1^{(j)} = \iint dxdy \, |\vec{f}_{1,j}|^2 \tag{2.21}$$

$$V_{1,2}^{(j)} = \frac{k_0^2}{2k_j P_1} \alpha \iint dxdy \, \chi_{1,j}^{(1)} \vec{f}_{2,j} \vec{f}_{1,j}^* \tag{2.22}$$

To simplify, we consider waveguides that can only support one mode so we omit the index $j$. The dynamics equation for the amplitude of the mode in waveguide 1 is similar to waveguide

2, known as the homogeneous coupled dimer

$$i\frac{\partial a_1}{\partial z} + V_{1,2}a_2 = 0 \tag{2.23}$$

$$i\frac{\partial a_2}{\partial z} + V_{2,1}a_1 = 0. \tag{2.24}$$

If each waveguide possesses a different propagation constant, the treatment is similar, but we assume a phase difference between both amplitude of the form $a_i(z) = u_i(z)e^{-ik_i z}$ yielding the inhomogeneous coupled dimer

$$-i\frac{\partial u_1}{\partial z} = k_1 u_1(z) + V_{1,2}u_2(z) \tag{2.25}$$

$$-i\frac{\partial u_2}{\partial z} = k_2 u_2(z) + V_{2,1}u_1(z). \tag{2.26}$$

These equations define the evolution of the dimer, we will return to this system in Chapter 5 to comment on the propagation of squeezed light through it. Generalizing the procedure to a d-dimensional lattice is straightforward and the evolution of the amplitude in the waveguide $i$ is governed by

$$-i\frac{\partial a_i}{\partial z} = \beta_i a_i + \sum_l V_{i,l}a_l, \tag{2.27}$$

with $\beta_i$ the propagation constant of the waveguide $i$-th depending on the size and material properties of each waveguide. Equation (2.27) does not tell us anything about the shape evolution of the mode, only its amplitude, and is valid as long as there are no abrupt changes in the direction of propagation or effects that destroys the shape of the mode.
The coupling matrix satisfies that $V^{(j)} \propto \frac{1}{k_j} \propto \lambda_j$; *i.e.*, the larger the wavelength of the mode, the larger is the effective coupling between waveguides. Also, since $V_{1,2} \propto (\vec{f}_{2,j} \cdot \vec{f}^*_{1,j})$, the coupling between waveguides is proportional to the spatial size of their modes and how much their tails reach adjacent waveguides. Until now we have only worked in 1-D and considered symmetrical waveguides where each polarization has the same mode. In asymmetrical waveguides, the mode's shape of each polarization is not equal and the coupling to adjacent waveguides depends on the polarization of injected light.
To summarize, the coupled mode theory approximates the evolution of the light through a waveguide as a constant mode that travels varying in amplitude in the $z$ direction. The amplitude evolves following a Schrodinger-like equation. To finish, we now can study the band structure by identifying the unit cell, expanding each waveguide amplitudes as plane waves with propagation constant $\lambda$ like $a_i(z) = \alpha_i e^{i\lambda z}$.

$$\lambda\alpha_i = (\beta_j + V_{ij})\alpha_j \tag{2.28}$$

Solving this equation allows us to get the band structure of the system just like in tight-binding models. Each value of $\lambda$ after solving the eigenvalue problem will tell us about the possible standing solution *i.e.* the normal modes of the system.

This, as we will see in Section 4, allow us to have photonic lattices with topological geometries capable of replicating the properties seen in Section 1 but using light, and in particular, using quantum light which is explained in the following section.

## 2.3. Experimental waveguides systems

To finalize explaining the coupled mode theory, we briefly show and comment on the experimental realization of waveguides. There are two principal methods to fabricate waveguides, the first one consists of depositing material with a higher refractive index called deposition. The second one locally changes the refractive index by removing or changing the distribution of the atoms and is called substitution. Among substitution methods, the femtosecond laser writing technique consists of locally modifying the refractive index inside a medium (typically some kind of glass) using a femtosecond laser, confining the light to travel within it with low losses [40] [41]. The waveguides are created by moving the femtosecond laser along the material, as seen in figure 2.3. By varying the power and speed of the writing, waveguides can be made of different sizes. The size and shape of the waveguides determine how many and which modes they can support, given the initial condition of the injected light (frequency and amplitude). The change in the refractive index is about the order of $10^{-3} - 10^{-4}$ with respect to the bulk material, making the approximation made in the previous section suitable to describe the behavior of these waveguides.

This technique makes the manufacture of waveguide lattices low-cost and low-time-consuming. The flexibility in their creation allows for waveguides of different sizes and distances between them. Particularly, it is fairly easy to simulate a time-dependent coupling by only varying the distance between waveguides as they are being written [42]. Making these experimental setups suitable for simulating a lattice with a time-dependent Hamiltonian.

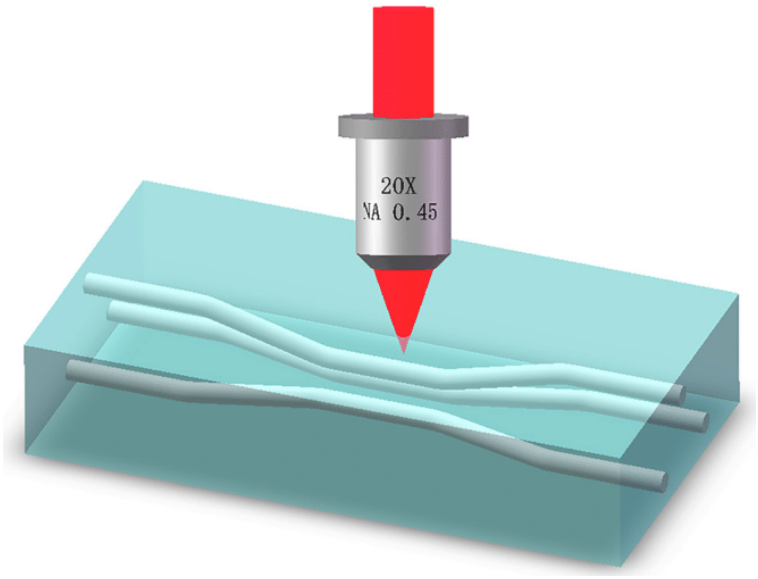


Figure 2.3: Example of a fetmosecond laser writing a waveguide [43].

# Chapter 3

# Quantum light

In the early 20th century, based on existing experimental evidence, light was predominantly considered as a wave, akin to sound, with the Maxwell equations accounting for its properties and behaviors. This perception changed with Einstein's photoelectric experiment in which light was associated with discrete energy packages, revealing its corpuscular nature and challenging the classical theory. Subsequently, in 1956, R. Hanbury Brown and R.Q. Twiss conducted a study on the correlation of intensity [44], which, while consistent with classical theory, showcased the predictive capabilities of the emerging quantum theory. Quantum theory could account for phenomena such as sub-Poissonian and sup-Poissonian photon statistics, which classical theory failed to explain. Notably, R.J. Glauber, in 1963, predicted the sub-Poissonian distribution [45], commonly referred to as photon anti-bunching. Experimental confirmation of this statistical property came in 1977, when H.J. Kimble, M. Dagenais, and L. Mandel observed it in the resonance fluorescence of a two-level atom [46], marking the first non-classical effect observed in optics.

A little later, squeezed light was theoretically proposed as a state of the electromagnetic field exhibiting a sub-Poissonian distribution of photons. This state, which originated from a non-linear process, was experimentally observed by R.E. Slusher,*et.al.* using Four-wave-mixing in 1985 [47]. The principal characteristic of squeezed states is their asymmetric distribution of the uncertainty principle along the canonical variables.

In this section, our focus is on deriving the quantum electromagnetic field and introducing the quadrature operator. We will explore its properties and discuss its significance in describing quantum electromagnetic states. Specifically, we will examine three important states: the Fock state, the coherent state, and the squeezed state, with particular emphasis on the latter as it is the main state used in this investigation.

## 3.1. Quantizing the electromagnetic field

To study the electric and magnetic field on the quantum regime we need to quantize them, starting from the Maxwell equations in vacuum

$$\vec{\nabla} \cdot \vec{E}(r,t) = 0 \qquad \vec{\nabla} \cdot \vec{B}(r,t) = 0 \tag{3.1}$$

$$\vec{\nabla} \times \vec{E}(r,t) = -\frac{\partial \vec{B}}{\partial t}(r,t) \qquad \vec{\nabla} \times \vec{B}(r,t) = \mu_0 \epsilon_0 \frac{\partial \vec{E}}{\partial t}(r,t), \tag{3.2}$$

where $\mu_0$ and $\epsilon_0$ are the magnetic and electric permittivity in vacuum, respectively. We can define a potential vector

$$\vec{B} = \vec{\nabla} \times \vec{\mathbf{A}}(r,t) \qquad \vec{E} = -\frac{\partial \vec{\mathbf{A}}}{\partial t}. \tag{3.3}$$

Using this definition and choosing the coulomb gauge ($\vec{\nabla} \cdot \vec{A} = 0$), the vector potential satisfies the wave equation

$$\nabla^2 \vec{\mathbf{A}} - \frac{1}{c^2} \frac{\partial^2 \vec{\mathbf{A}}}{\partial t^2} = 0, \tag{3.4}$$

where $c = \frac{1}{\sqrt{\mu_0 \epsilon_0}}$ is the speed of light. It is sufficient to find the potential vector $\vec{\mathbf{A}}$ to get both electric and magnetic fields.
The general solution of (3.4) can be expanded in normal modes as

$$\vec{A}(r,t) = \sum_{k,\alpha} C_k a_k(t) \vec{u}_{k,\alpha}(\vec{r}) + c.c., \tag{3.5}$$

where the summation is taken over an infinite discrete set of values of the wave vector $\vec{k}$ in three dimensions, $a_k(t)$ is a dimensionless scalar function that depends on time and $\vec{u}_{k,\alpha}(\vec{r})$ is a vector function which is orthogonal between different modes and depends on the polarization $\alpha$ and position $\vec{r}$. The constant $C_k$ is defined as

$$C_{\mathbf{k}} = \left( \frac{\hbar}{2\epsilon_0 \omega_k} \right)^{\frac{1}{2}}, \tag{3.6}$$

which is conveniently defined this way to ease future calculations. Plugging the solution above in the wave equation (3.4) yields

$$\nabla^2 \vec{u}_{k,\alpha} + \frac{\omega_k^2}{c^2} \vec{u}_{k,\alpha} = 0 \qquad \frac{\partial^2 a_k}{\partial t^2} + \omega_k^2 a_k = 0, \tag{3.7}$$

We now consider the fields inside a big but finite 3D square box of width L. From the last equations, the solution for $\vec{u}_{\alpha,k}$ can be plane waves or sinusoidal waves, by imposing periodic boundary conditions

$$u_{k,\alpha}(\vec{r}) = \vec{u}_{k,\alpha}(\vec{r} + L\hat{x}) = \vec{u}_{k,\alpha}(\vec{r} + L\hat{y}) = \vec{u}_{k,\alpha}(\vec{r} + L\hat{z}), \tag{3.8}$$

we get plane waves solutions

$$\vec{u}_{k,\alpha}(\vec{r}) = \frac{\vec{\epsilon}_{k,\alpha}}{\sqrt{V}} \exp\Big(i\vec{k}_n \cdot \vec{r}\Big) + c.c., \tag{3.9}$$

where $\vec{k}_n = \frac{2\pi}{L}(n_x, n_y, n_z)$ with $n_i \in \mathbb{N}$ and $V = L^3$.
The second equation tells us that $a_k(t)$ evolves as an harmonic oscillator, with the solution

$$a_k(t) = a_k \exp(-i\omega_k t) + c.c. \tag{3.10}$$

Using both solutions and redefining $C_k = C_k/\sqrt{V}$, the fields take the form of

$$\vec{A} = \sum_{k,\alpha} C_{\mathbf{k}} \vec{\epsilon}_{k,\alpha} a_{\mathbf{k}} \exp\Big(i(\vec{k}_n \vec{r} - \omega_k t)\Big) + c.c. \tag{3.11}$$

$$\vec{E} = i \sum_{k,\alpha} C_{\mathbf{k}} \omega_k \vec{\epsilon}_{k,\alpha} a_{\mathbf{k}} \exp\Big(i(\vec{k}_n \vec{r} - \omega_k t)\Big) - c.c. \tag{3.12}$$

$$\vec{B} = \frac{i}{c} \sum_{k,\alpha} C_{\mathbf{k}} (\vec{k} \times \vec{\epsilon}_{k,\alpha}) a_{\mathbf{k}} \exp\Big(i(\vec{k}_n \vec{r} - \omega_k t)\Big) - c.c. \tag{3.13}$$

Since $\vec{\nabla} \cdot \vec{A} = 0$, we have that $\vec{k}$ must satisfy

$$\vec{k} \cdot \vec{\epsilon}_{k,\alpha} = 0, \tag{3.14}$$

meaning the fields are purely transverse and therefore the two polarization are independent for each $k$.
The electromagnetic Hamiltonian is defined as

$$\mathcal{H} = \frac{1}{2} \int dV \Big[\epsilon_0 |\mathbf{E}|^{\mathbf{2}} + \frac{\mathbf{1}}{\mu_{\mathbf{0}}} |\mathbf{B}|^{\mathbf{2}}\Big] \tag{3.15}$$

Using the definition of the fields in (3.11) and expanding the constant $C_k$ yields (since both polarizations are independent of each other) we get the classical Hamiltonian as

$$\mathcal{H} = \sum_k \hbar\omega_k (a_k a_k^*), \tag{3.16}$$

the form of the constant $C_k$ was chosen specifically to arrive at this Hamiltonian, otherwise, we would have carried extra constants hindering the explanation and making it harder to see the resemblance of the harmonic oscillator.
We can redefine this Hamiltonian by using the classical canonical variables of position and momentum $q$ and $p$, respectively, as

$$a_k = \frac{1}{\sqrt{\hbar\omega_k}}(\omega_k q_k + i p_k) \qquad\qquad a_k^* = \frac{1}{\sqrt{\hbar\omega_k}}(\omega_k q_k - i p_k) \tag{3.17}$$

arriving at an analog of the harmonic oscillator

$$\mathcal{H} = \sum_k \frac{1}{2}[p_k^2 + (\omega_k q_k)^2]. \tag{3.18}$$

Up to this point, we have worked on the classical domain whereby by imposing some conditions on the Maxwell equation we get the fields, and by using them in the electromagnetic Hamiltonian we arrive at the form of the harmonic oscillator. To quantize, we use the standard procedure, that is, by promoting the canonical variables to operators satisfying the conmutation relations

$$q \to \hat{q} \qquad\qquad p \to \hat{p} \qquad\qquad [\hat{q}, \hat{p}] = i\hbar\hat{I} \tag{3.19}$$

imposing this, we transform the amplitudes $a_k$ and $a_k^*$ into the operators $\hat{a}_k$ and $\hat{a}_k^\dagger$, respectively, satisfying the commutation relations

$$[\hat{a}_k, \hat{a}_{k'}^\dagger] = \delta_{k,k'} \qquad\qquad [\hat{a}_k, \hat{a}_{k'}] = 0 = [\hat{a}_k^\dagger, \hat{a}_{k'}^\dagger], \tag{3.20}$$

$\hat{a}_k$ and $\hat{a}_k^\dagger$ are the annihilation and creation operators of the mode $k$. Replacing the newly promoted operators into the energy (3.15) yields the quantum electromagnetic Hamiltonian

$$\hat{\mathcal{H}} = \sum_k \hbar\omega_k(\hat{a}_k^\dagger\hat{a}_k + \frac{1}{2}) = \sum_k \hbar\omega_k(\hat{N} + \frac{1}{2}), \tag{3.21}$$

$\hat{N_k} = \hat{a}_k^\dagger\hat{a}_k$ is the number operator for the mode $k$. Expanding the constant $C_k$, the quantum electromagnetic fields are

$$\vec{A}(r,t) = \sum_{k,\alpha} \sqrt{\frac{\hbar}{2\epsilon_0 V\omega_k}}\vec{\epsilon}_{k,\alpha}\hat{a}_k \exp\left[i(\vec{k}\vec{r} - \omega_k t)\right] + c.c \tag{3.22}$$

$$\vec{E}(r,t) = i\sum_{k,\alpha} \sqrt{\frac{\hbar\omega_k}{2\epsilon_0 V}}\vec{\epsilon}_{k,\alpha}\hat{a}_k \exp\left[i(\vec{k}\vec{r} - \omega_k t)\right] - c.c \tag{3.23}$$

$$\vec{B}(r,t) = \frac{i}{c}\sum_{k,\alpha} \sqrt{\frac{\hbar}{2\epsilon_0 V\omega_k}}(\vec{k} \times \vec{\epsilon}_{k,\alpha})\hat{a}_k \exp\left[i(\vec{k}\vec{r} - \omega_k t)\right] - c.c \tag{3.24}$$

The index $k$ denotes the different modes of the electromagnetic field which in principle are infinite and the total solution is the sum of all of them. However, in photonic lattices, the evolution is given by one mode per the waveguide, then when propagating quantum light we can limit the sum and relate each $k$ to the waveguide $k$ where $\hat{a}_k$ destroys a photon in the $k$-th waveguide, this is elaborated in section 4.

## 3.2. The quadrature, uncertainty principle, and Wigner function

We now introduce the quadrature operator, its properties, and what is their use in representing quantum light states, later, we will connect it with the Wigner function as a way to fully describe a state. The generalized quadrature operator for the mode $j$ of the electromagnetic field is defined for an angle $\phi$ as

$$\hat{X}_j(\phi) = \frac{1}{2}(\hat{a}_j e^{-i\phi} + \hat{a}_j^\dagger e^{i\phi}), \tag{3.25}$$

for any angle, it satisfies

$$[\hat{X}(\phi), \hat{X}(\phi + \frac{\pi}{2})] = \frac{i}{2} \qquad\qquad \Delta X(\phi)\Delta X(\phi + \frac{\pi}{2}) \geq \frac{1}{4}, \tag{3.26}$$

with the variance defined as $(\Delta X)^2 = \langle \hat{X}^2 \rangle - \langle \hat{X} \rangle^2$, and $\langle\,\rangle$ is the expectation value of an arbitrary state. We can connect them to the known momentum and position operators of a mode $j$ as

$$X_j(0) = X_j^{(1)} = \sqrt{\frac{\omega}{2\hbar}} \cdot \hat{q}_j = \frac{1}{2}(\hat{a}_j + \hat{a}_j^\dagger) \tag{3.27}$$

$$X_j(\frac{\pi}{2}) = X_j^{(2)} = \frac{1}{\sqrt{2\hbar\omega}} \cdot \hat{p} = \frac{1}{2i}(\hat{a}_j - \hat{a}_j^\dagger) \tag{3.28}$$

They are orthogonal quadratures and, like the canonical variables, describe the phase space of the system. We can use their definition to redefine the electromagnetic field in (3.22)-(3.24) as

$$\hat{A}(r,t) = \sum_{k,\alpha} \sqrt{\frac{2\hbar}{\epsilon_0 V \omega_k}} \hat{\epsilon}_{k,\alpha} \left[ \hat{X}_k^{(1)} \cos(\vec{k}\vec{r} - \omega_k t) - \hat{X}_k^{(2)} \sin(\vec{k}\vec{r} - \omega_k t) \right] \tag{3.29}$$

$$\hat{E}(r,t) = -\sum_{k,\alpha} \sqrt{\frac{\hbar\omega_k}{2\epsilon_0 V}} \hat{\epsilon}_{k,\alpha} \left[ \hat{X}_k^{(1)} \sin(\vec{k}\vec{r} - \omega_k t) + \hat{X}_k^{(2)} \cos(\vec{k}\vec{r} - \omega_k t) \right] \tag{3.30}$$

$$\hat{B}(r,t) = \sum_{k,\alpha} \sqrt{\frac{\hbar}{2\epsilon_0 V \omega_k}} (\vec{k} \times \hat{\epsilon}_{k,\alpha}) \left[ \hat{X}_k^{(1)} \sin(\vec{k}\vec{r} - \omega_k t) + \hat{X}_k^{(2)} \cos(\vec{k}\vec{r} - \omega_k t) \right] \tag{3.31}$$

We now see that both quadratures represent the magnetic and electric fields with a $\frac{\pi}{2}$ phase between them. As conjugate variables, $X^{(1)}$ and $X^{(2)}$ cannot be measure simultaneously. Both operators $\hat{X}_1$ and $\hat{X}_2$ can be used to represent properties of states of light by analyzing the phase-space diagram. The uncertainty of each state is represented as an area in the phase space. From a "classical" point of view, the distance from the origin to the state is proportional to the photon number or amplitude of the field and the complex angle between the axes is proportional to the phase of the field. The angle $\phi$ in equation (3.25) defines the reference of phase-space axes. In the field equations, this translates to adding an extra phase

$\phi$.

To fully describe a quantum state, we now introduce the Wigner Function. It is a quantum generalization of the classical distribution function which depends on the phase-space variables. Even though the Wigner function plays an analog role to a conventional distribution function, it does not satisfy the same properties. As a quasi-probabilistic function, it might yield negative values corresponding to quantum states, nevertheless, quantum states can have positive values as it is seen in the squeezed state. The Wigner function for a system represented with a density operator $\hat{\rho}$ is

$$W(q,p) = \frac{1}{4\pi\hbar}\int_{\infty}^{\infty}\langle q + \frac{1}{2}x|\hat{\rho}|q - \frac{1}{2}x\rangle e^{ipx/\hbar}dx \tag{3.32}$$

where $q = X^{(1)}(0)$ and $p = X^{(2)}(0)$, for pure states the density operator can be written as $\hat{\rho} = |\psi\rangle\langle\psi|$, which is the case for all states above. Integrating the Wigner function for all variables yields 1 *i.e.*, it is normalized, and integrating over one canonical variable yield the probability function of the other one

$$\int d^N q\, d^N p\, W(q,p) = 1 \tag{3.33}$$

$$\int d^N q\, W(q,p) = |\phi(p)|^2 \tag{3.34}$$

$$\int d^N p\, W(q,p) = |\psi(q)|^2 \tag{3.35}$$

where $\phi(p)$ and $\psi(q)$ are the momentum and coordinate space wave functions, respectively. Just like in classical statistics, integrating this function with a given operator yields the average. The Wigner function tells us about the quantum properties of the state and it is used to differentiate each state.

## 3.3. Quantum states of light

In the previous section, we defined the electric and magnetic fields in terms of operators, successfully quantizing both fields. What is left to do is define the quantum states that describe the fields and their properties. In this section, we will introduce the concept of the "Fock state," which serves as a discrete representation of the number of photons within a field. Additionally, we will discuss the "Coherent state," known for possessing minimal uncertainty and being regarded as the most 'classical' state. Finally, we will explore the "Squeezed state," which exhibits an asymmetric distribution of uncertainty. We will show the properties of each state using the quadrature and the phase-space representation, the Wigner function. Taking special emphasis on squeezed states which are the main focus of this thesis [48, 49].

### 3.3.1. Fock states

Fock states, also called number states, are defined through the number operator $N_k = \hat{a}_k^\dagger \hat{a}_k$. The eigenstate of this operator is the well-defined number state $|n\rangle$ with the relations

$$\hat{a}_k^\dagger |n_k\rangle = \sqrt{n_k + 1}\, |n_k + 1\rangle \qquad \hat{N}_k |n_k\rangle = n_k |n_k\rangle \tag{3.36}$$

$$\hat{a}_k |n_k\rangle = \sqrt{n_k}\, |n_k - 1\rangle\,, \tag{3.37}$$

where $\hat{a}_k$ and $\hat{a}_k^\dagger$ are the creation and annihilation operators with the commutations relation in (3.20). Its quadrature properties are

$$\langle n| \hat{X}_1 |n\rangle = 0 \qquad \langle n| \hat{X}_2 |n\rangle = 0 \tag{3.38}$$

$$\langle n| \hat{X}_1^2 |n\rangle = \frac{1}{4}(2n+1) \qquad \langle n| \hat{X}_2^2 |n\rangle = \frac{1}{4}(2n+1) \tag{3.39}$$

$$(\Delta\hat{X}_1)^2 (\Delta\hat{X}_2)^2 = \frac{1}{16}(4n^2 + 4n + 1) \tag{3.40}$$

The relations on 3.38 tell us that a single Fock state is not a state of well-defined electric and magnetic fields, this is because the operators $\hat{E}$ and $\hat{N}$ do not commute. This, however, does not hold when taking a superposition of Fock states as we will see in the coherent states. The relation 3.39 shows the uncertainty increases proportionally to the photon number, meaning the uncertainty of the field is well defined. This state minimizes the uncertainty principle for $n = 0$, and it increases proportionally to the photon number, as seen in relation 3.40. For the Hamiltonian and the number operator, we have

$$\hat{H} |n\rangle = \hbar\omega(n + \frac{1}{2}) |n\rangle \tag{3.41}$$

$$\langle n| (\Delta n)^2 |n\rangle = 0 \tag{3.42}$$

The relation 3.41 implies that the state fock state represents the energy of the field as discrete amounts of $\hbar\omega$ proportional to the photon number. Finally, the relation 3.42 indicates that the Fock state possesses a "sharp" photon number but, because of the uncertainty principle, the phase of the field, which is the canonical variable to the photon number, is completely lost [48].

The multimode basis is constructed using the tensor product between sub-spaces

$$|n\rangle = |n_1\rangle \otimes |n_2\rangle \otimes |n_3\rangle \,... \otimes |n_\infty\rangle = |n_1, n_2, ..n_\infty\rangle\,, \tag{3.43}$$

each of these kets fulfill the relation $\langle n_i | n_j \rangle = \delta_{i,j}$.

The Wigner function of the Fock state is shown in figure 3.1. The photon number is represented as the distance from the origin to where the area is located, in this case, an area shaped like a circle . The number of circles around the origin is proportional to the number of photons, each circle is highlighted on yellow. The phase, defined as the angle between the axes, goes from 0 to $2\pi$ which correspond to a superposition of all possible phases meaning

that the phase is undefined for the Fock state. The quadratures are centered on the origin while the uncertainty is represented as the width of each circle, which is equal in both quadratures and increases with the photon number.

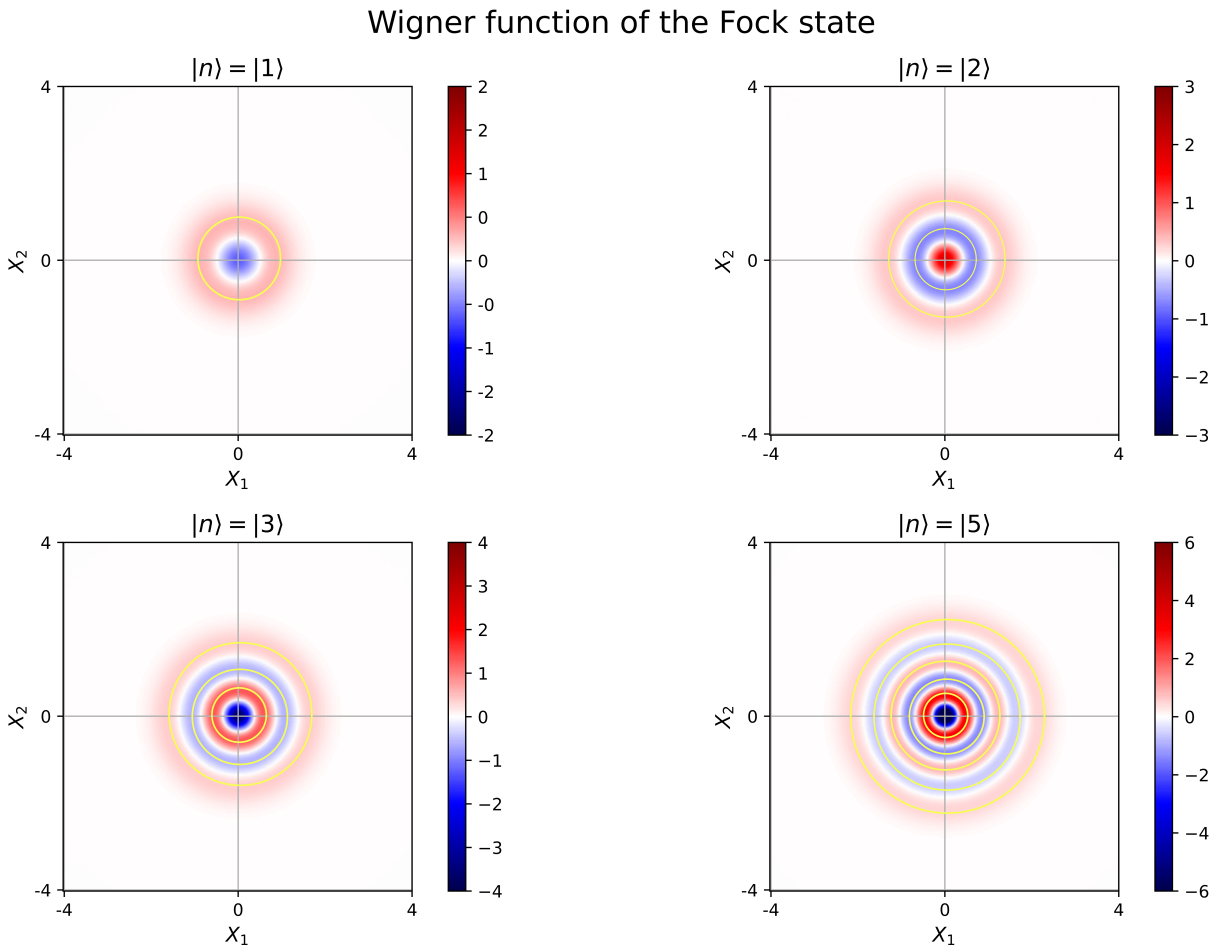


Figure 3.1: Wigner function for the Fock states $|1\rangle, |2\rangle, |3\rangle$ and $|5\rangle$. The photon number is proportional to the radius from the origin to the outer circle, each state has the same number of circles as the number of photons. The negativity of the Wigner function implies that the state is non-classical. The phase defined by the angle between planes is, in this case, undefined as it is an infinite superposition from 0 to $2\pi$.

Because of their discrete nature, Fock states have been proposed for several protocols and setups in quantum information and communication [50, 51]. The limits are the challenging realization in experiments of single or more indistinguishable photons with high fidelity [52, 53]. Even though deterministic methods have been proposed [54, 55], to this date, there has not been an experiment to produce this kind of state at the fidelity and stability required.

### 3.3.2. Coherent states

The coherent state is defined as the eigenstate of the annihilation operator $\hat{a}$:

$$\hat{a}\,|\alpha\rangle = \alpha\,|\alpha\rangle \tag{3.44}$$

Expanding on the Fock basis it can be rewritten as

$$|\alpha\rangle = e^{-\frac{|\alpha^2|}{2}} \sum_n \frac{\alpha^n}{\sqrt{n!}}\,|n\rangle\,, \tag{3.45}$$

corresponding to a Poissonian distribution in the photon number.
The quadrature relations for the coherent states are

$$\langle\alpha|\,\hat{X}^{(1)}\,|\alpha\rangle = \frac{1}{2}(\alpha+\alpha^*) = \mathrm{Re}(\alpha) \qquad \langle\alpha|\,\hat{X}^{(2)}\,|\alpha\rangle = \frac{1}{2i}(\alpha-\alpha^*) = \mathrm{Im}(\alpha) \tag{3.46}$$

$$\langle\alpha|\,(\hat{X}^{(1)})^2\,|\alpha\rangle = \frac{1}{4} + \mathrm{Re}(\alpha)^2 \qquad \langle\alpha|\,(\hat{X}^{(2)})^2\,|\alpha\rangle = \frac{1}{4} + \mathrm{Im}(\alpha)^2 \tag{3.47}$$

then each quadrature obeys

$$\langle\Delta\hat{X}^{(1)}\rangle^2 = \langle(\hat{X}^{(1)})^2\rangle_\alpha - (\langle\hat{X}^{(1)}\rangle_\alpha)^2 = \frac{1}{4}\langle\Delta\hat{X}^{(1)}\rangle^2\langle\Delta\hat{X}^{(2)}\rangle^2 = \frac{1}{16} \tag{3.48}$$

$$\langle\Delta\hat{X}^{(2)}\rangle^2 = \langle(\hat{X}^{(2)})^2\rangle_\alpha - (\langle\hat{X}^{(2)}\rangle_\alpha)^2 = \frac{1}{4} \tag{3.49}$$

The average of the quadrature means the state is displaced on the phase space depending on the real and imaginary parts of $\alpha$. They are also states of well-defined electromagnetic fields, using relations (3.44) in (3.22)-(3.24) yields a nonzero amplitude that maintains the initial form of the fields, looking analogous to the classical fields. From equations in (3.48), the coherent state is independent of $\alpha$ and has minimum uncertainty relation on each quadrature. The Hamiltonian and number operators satisfy

$$\langle\alpha|\,\hat{H}\,|\alpha\rangle = \hbar\omega(|\alpha|^2 + \frac{1}{2}) \qquad \langle\alpha|\,\Delta n\,|\alpha\rangle^2 = |\alpha|^2 \tag{3.50}$$

meaning the energy of this state is proportional to its amplitude and the standard deviation of the photon number is equal to its mean value, as expected of a Poissonian distribution.
It also is possible to define the operator $\hat{D}(\alpha)$, which when applied to the vacuum, yields the coherent state

$$\hat{D}(\alpha)\,|0\rangle = |\alpha\rangle\,, \tag{3.51}$$

The operator $\hat{D}$ is called the displacement operator and it is defined for a general mode $i$ as

$$\hat{D}_i(\alpha) = \exp\Big(\alpha\hat{a}_i^\dagger - \alpha^*\hat{a}_i\Big) \tag{3.52}$$

The representation of a coherent state with $\alpha = |\alpha|e^{i\theta}$ on the phase-space plane is shown in figure 3.2. It is represented as circular area where the distance from the origin to the center

of the circle is the amplitude $|\alpha|$ and the polar angle between both axes is $\theta$. The Wigner function is centered at $(\mathrm{Re}\{\alpha\}, \mathrm{Im}\{\alpha\})$, while the uncertainty is constant and equal on both quadratures shown by the circle.

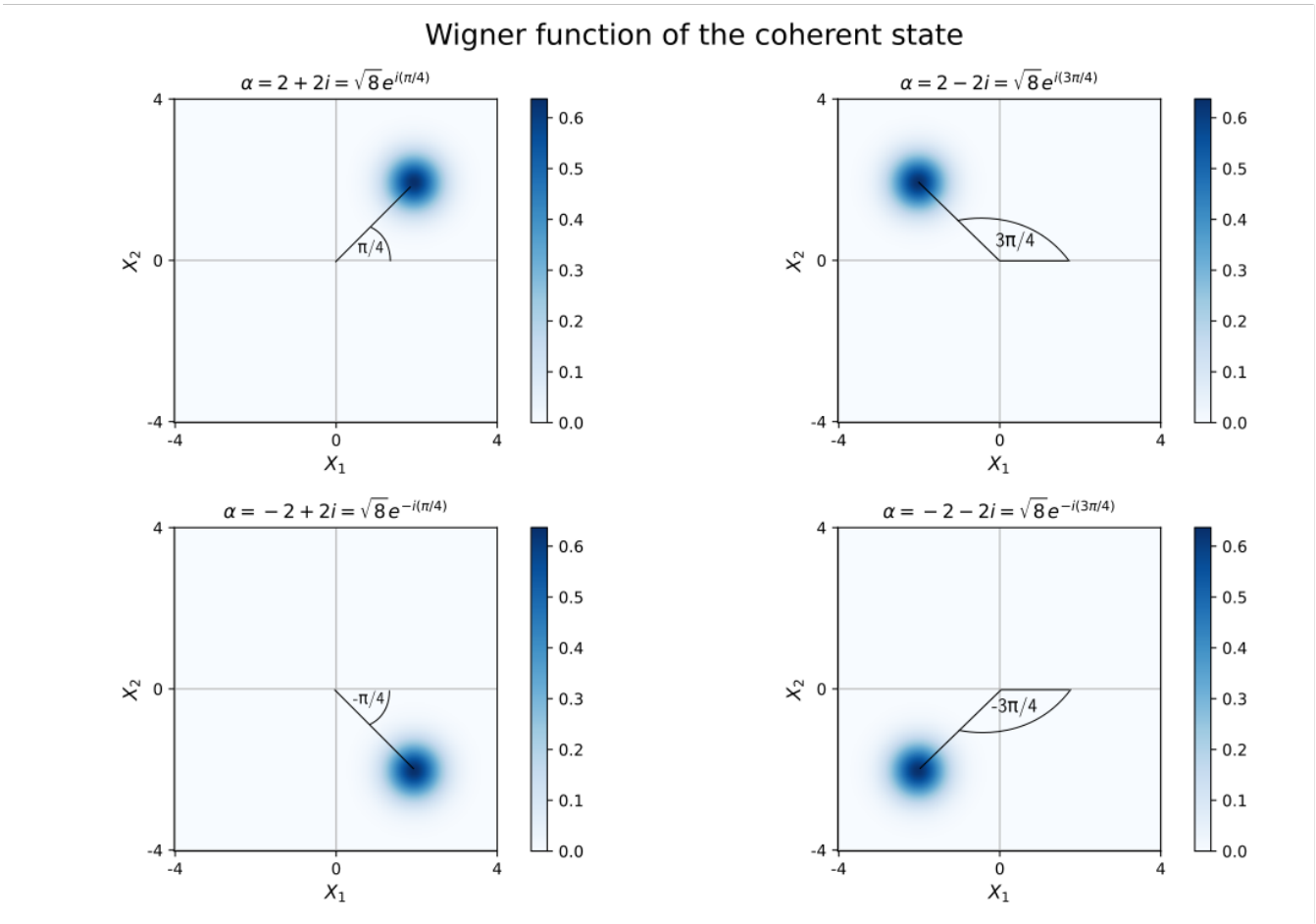


Figure 3.2: Wigner function for a coherent state $\alpha = |\alpha|e^{i\theta}$, where $\alpha = \sqrt{8}$ and the phases are $(\frac{\pi}{4}, \frac{-\pi}{4}, \frac{3\pi}{4}, \frac{-3\pi}{4})$. The distance from the origin to the center of the area is proportional to the amplitude while the angle between the axes is proportional to the phase of the coherent state.

Coherent states share many properties and similarities with the classical fields, as such, they are regarded the most "classical" state. The expectation value of the quantum field takes the same form as the classical field and they follow Poissonian statistics. The fluctuation in both phase and amplitude quadratures becomes negligible for a large number of photons, which can be interpreted as watching the phase space from afar where the circled area looks like a point, making amplitude and phase well-defined within classical magnitudes. These states minimize the uncertainty principle and as such, they define the standard quantum limit of measurement.

### 3.3.3. Squeezed states and their properties

Squeezed light is a quantum state of light with the property of having an asymmetrical uncertainty in their quadratures, this means that the measurement of the "squeezed" quadrature is enhanced while the "stretched" quadrature losses accuracy, always obeying the uncertainty principle.

$$(\Delta\hat{X}(\phi))^2 < \frac{1}{4} \qquad\qquad (\Delta\hat{X}(\phi+\frac{\pi}{2}))^2 > \frac{1}{4} \tag{3.53}$$

where $\phi$ defines the phase-space reference of the orthogonal quadratures. We can squeeze the quadrature of a single mode, this is known as a single-mode squeezed state. Or we can squeeze the quadrature superposition of 2 or more modes, called two-mode squeezing and multi-mode, respectively. This state is different from the single mode because the squeezed quadratures of a two-mode state contain a correlation between both modes, manifesting entanglement. We first analyze the single-mode field to make the squeezed state easier to comprehend.
Considering the single-mode squeezed vacuum state defined as

$$\hat{S}(\xi)\,|0\rangle = |\xi\rangle \tag{3.54}$$

Similar to the coherent state we can define the squeezing operator as

$$\hat{S}(\xi) = \exp\Big\{\frac{1}{2}(\xi^*\hat{a}^2 - \xi(\hat{a}^\dagger)^2)\Big\}, \tag{3.55}$$

where $\xi = r\exp(i\theta)$, with $r$ the magnitude of squeezing defining how much the quadrature is squeezed and $\theta$ defining which quadrature is squeezed in relation with the chosen quadrature axes determined by $\phi$.
We can compute how it transforms the annihilation and creation operators using the Baker–Campbell–Hausdorff (BCH) formula

$$e^A B e^{-A} = B + \frac{1}{2}[[B,A],A] + ... + \frac{1}{n!}\underbrace{[[B,A],...,A]}_{\text{n veces}} \tag{3.56}$$

for the squeezing operator, this relation yields

$$\hat{S}^\dagger(\xi)\hat{a}\hat{S}(\xi) = \hat{a}\cosh(r) - \hat{a}^\dagger e^{i\theta}\sinh(r), \tag{3.57}$$

$$\hat{S}^\dagger(\xi)\hat{a}^\dagger\hat{S}(\xi) = \hat{a}^\dagger\cosh(r) - \hat{a}e^{-i\theta}\sinh(r). \tag{3.58}$$

Using these, the uncertainty of the quadrature yields

$$\langle(\Delta\hat{X}^{(1)}(\phi))^2\rangle = \frac{1}{4}[\cosh(2r) - \sinh(2r)\cos(\theta - 2\phi)], \tag{3.59}$$

$$\langle(\Delta\hat{X}^{(2)}(\phi))^2\rangle = \frac{1}{4}[\cosh(2r) + \sinh(2r)\cos(\theta - 2\phi)]. \tag{3.60}$$

For $\theta = 2\phi$ we get

$$\langle(\Delta\hat{X}^{(1)})^2\rangle = \frac{1}{4}e^{-2r} \qquad\qquad \langle(\Delta\hat{X}^{(2)})^2\rangle = \frac{1}{4}e^{2r} \tag{3.61}$$

The uncertainty principle can be understood using the phase space diagram. The area defined by the uncertainty of any state must be greater than $\frac{1}{16}$, but this relation does not put a condition on how this area is shaped.

Equations on (3.61) indicate that the uncertainty of a squeezed state decreases below the standard uncertainty limit for a quadrature at the cost of increasing the uncertainty in the orthogonal quadrature.

The squeezed vacuum state is represented as an ellipse centered at the origin. It is possible to move this state by applying the displacement operator defined before. We must notice that the displacement and squeezing operators do not commute thus a displaced squeezed state possesses a different phase-space representation than a squeezed displaced state.

From equations (3.59) and (3.60), $\theta$ defines which quadrature is squeezed according to the reference of the quadratures. Usually, the phase $\phi$ is set such that the uncertainty is minimized, so the axes are aligned to the squeezed quadrature. Otherwise, the ellipse is distributed between quadratures where each one will be squeezed by a different amount.

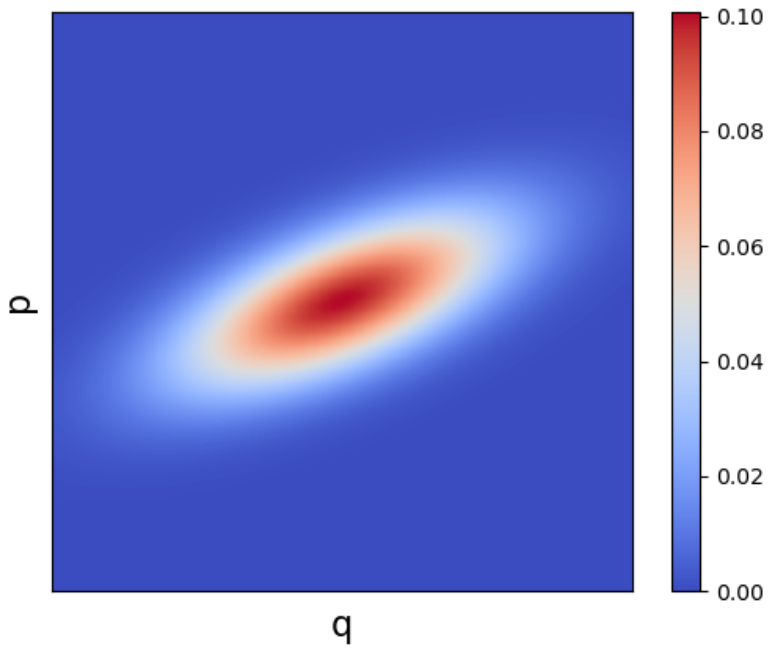


Figure 3.3: Wigner function of a single-mode squeezed state with $\xi = 0.5e^{i\pi/4}$. The ellipse is rotated at an angle $\pi/8$ with respect to $\mathbf{q}$

To characterize how much a quadrature is squeezed, we use a standard decibel formula for the uncertainty using the coherent state as the reference

$$S[dB] = 10\log_{10}\left(\frac{\langle\Delta\hat{X}\rangle^2(\phi)}{\langle\Delta\hat{X}\rangle^2_{ch}}\right), \tag{3.62}$$

with $\langle\Delta\hat{X}\rangle^2$ the uncertainty of the measured state and $\langle\Delta\hat{X}\rangle^2_{ch} = 1/4$ the uncertainty of the coherent state. A state with a squeezed quadrature yields negative values, a stretched quadrature yields positive values, and if the uncertainty is equal to the coherent state, the value is zero.

### 3.3.4. Two-mode squeezed state

The two-mode squeezed states of light are defined by squeezing the superposition of the quadrature between two modes of the electromagnetic field. If we consider a multi-mode field like (3.22)-(3.23), an exact solution for a free propagating field can be calculated using the infinite sum of all the modes, this only get worse if we add non-linear effect as the interaction between modes is generated, this is no easy feat. Luckily in photonic lattices, only one mode is supported per waveguide so the total field inside the lattice is a superposition of each fundamental mode $k$, corresponding to the waveguide $k$. This means that saying correlation between the mode $i$ and $j$ means a correlation between the light on waveguides $i$ and $j$. To understand this correlation we introduce the general two-mode orthogonal quadratures

between modes $i$ and $j$ as

$$\hat{X}^{(1)}_{i,j} = \frac{1}{\sqrt{2}}[\hat{X}^{(1)}_i(\phi) + \hat{X}^{(1)}_j(\phi)] = \frac{1}{2^{\frac{3}{2}}}[(\hat{a}^\dagger_i + \hat{a}^\dagger_j)e^{i\phi} + (\hat{a}_i + \hat{a}_j)e^{-i\phi}] \tag{3.63}$$

$$\hat{X}^{(2)}_{i,j} = \frac{1}{\sqrt{2}}[\hat{X}^{(2)}_i(\phi) + \hat{X}^{(2)}_j(\phi)] = \frac{1}{2^{\frac{3}{2}}i}[(\hat{a}_i + \hat{a}_j)e^{-i\phi} - (\hat{a}^\dagger_i + \hat{a}^\dagger_j)e^{i\phi}] \tag{3.64}$$

We can squeeze one of these quadratures by using the two-mode squeezing operators

$$\hat{S}_{ij}(\xi) = \exp\Big\{\xi^* \hat{a}_i \hat{a}_j - \xi\, \hat{a}^\dagger_i \hat{a}^\dagger_j\Big\}, \tag{3.65}$$

with $\xi = re^{i\theta}$ defined in an analogous way to the single mode, it satisfies the properties

$$\hat{S}^\dagger_{ij}\hat{a}_{i(j)}\hat{S}_{ij} = \cosh(r)\hat{a}_{i(j)} - e^{i\theta}\hat{a}^\dagger_{j(i)}\sinh(r) \tag{3.66}$$

$$\hat{S}^\dagger_{ij}\hat{a}^\dagger_{i(j)}\hat{S}_{ij} = \cosh(r)\hat{a}^\dagger_{i(j)} - e^{-i\theta}\hat{a}_{j(i)}\sinh(r) \tag{3.67}$$

Acting on the vacuum $|\psi_{ij}\rangle = \hat{S}_{ij}\,|0_i, 0_j\rangle$, we get a state where its two-mode quadrature is squeezed as

$$\langle(\Delta\hat{X}^{(1)}_{i,j})^2\rangle = \frac{1}{4}[\cosh^2(r) + \sinh^2(r) - 2\sinh(r)\cosh(r)\cos(\theta - 2\phi)] \tag{3.68}$$

$$\langle(\Delta\hat{X}^{(2)}_{i,j})^2\rangle = \frac{1}{4}[\cosh^2(r) + \sinh^2(r) + 2\sinh(r)\cosh(r)\cos(\theta - 2\phi)] \tag{3.69}$$

yielding the same result as the quadrature for the single mode state, but here we are squeezing the superposition of both modes. Expanding in the Fock basis, the two mode squeezed state can be written as

$$|\xi_{i,j}\rangle = \frac{1}{\cosh r}\sum_{n=0}^{\infty}(-1)^n e^{in\theta}(\tanh r)^n\,|n_i, n_j\rangle\,, \tag{3.70}$$

each pair $|n_i, n_j\rangle$ corresponds to the number state of both modes $i, j$ and they are correlated. This state cannot be separated into two single-mode states, and as such, it has entanglement properties containing a correlation between both [56].

If we are working only with two-mode states, the selection of $\phi$ is performed, just like in the single-mode, by choosing the angle that minimizes the superposition of quadratures in equation (3.68).

In the presence of single-mode squeezing the choice of the angle $\phi$ is not so simple because the single-mode squeezing has a contribution to the two-mode squeezing but as a single-mode, it does not bring correlation between modes. Not selecting the correct phase $\phi$ can lead to misinterpretation and the appearance of two-mode squeezing where there is none.

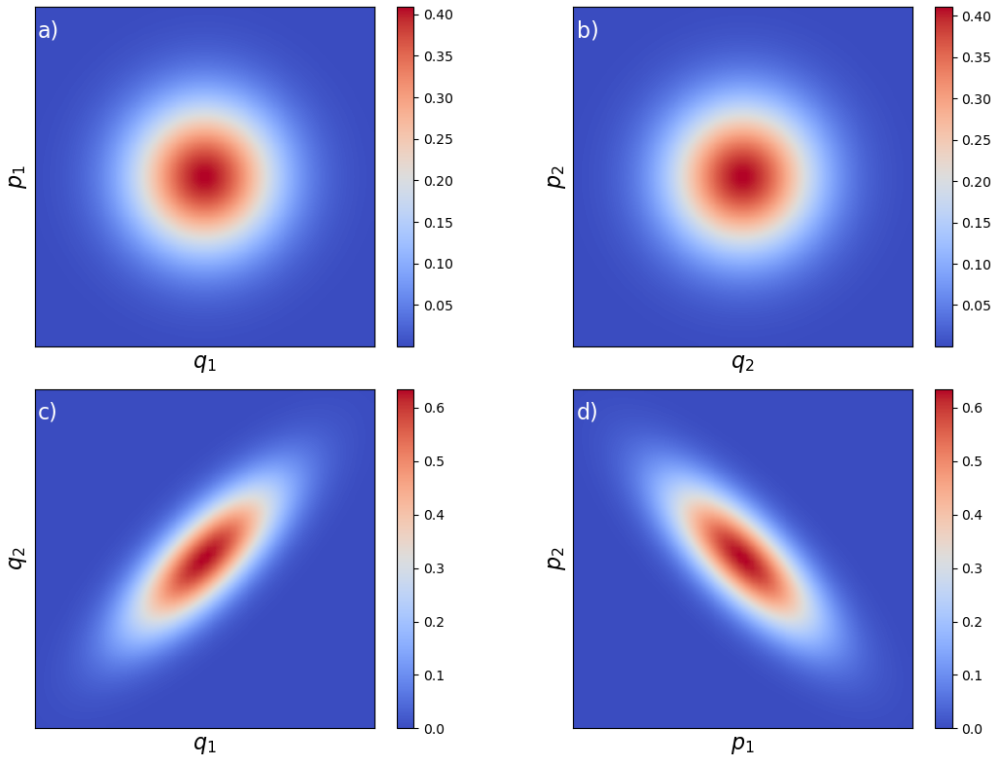


Figure 3.4: Wigner function of a two-mode squeezed state with magnitude $\xi = 0.5$. **a)** and **b)** are the marginal distribution between each mode $j = (1, 2)$, showing no single mode squeezing. **c)** and **d)** are the marginal distributions for the combination of modes, where each quadrature has entanglement between modes.

As depicted in figure 3.4, the Wigner function of the two modes squeezed state, shows no correlation between the same mode meaning there is no single-mode squeezing.

### 3.3.5. Generation and usage of squeezed states

Squeezed states are produced using non-linear interactions, needing precise conditions on the injected light and the non-linear medium. The most common processes to generate them are by four-wave-mixing [47] and an optical parametric oscillator [57]. Squeezed light possesses interesting and unique properties with no classical counterpart. The most impactful property is they can decrease the uncertainty for amplitude or phase quadratures allowing for measurements below the standard noise limit defined by the coherent state [58, 59, 60]. In particular, the usage of squeezed state in metrology has allowed for the enchantment of detection systems. The most famous example is in the LIGO collaboration for the detection of gravitational waves, where by using vacuum-squeezed states they managed to improve the measurement beyond the quantum noise limit. This enhancement in performance allowed the clear detection of gravitational waves in 2015 [61]. Apart from gravitational waves, sensing with squeezed light has increased in many areas as they show much promise for the future [62]. These states have also been proposed as continuum variables for computer quantum protocols, like teleportation [63] and logic gates, among others [64, 65, 3].

The current challenges these states possess in technology are their creation and propagation without the loss in coherence, entanglement, and amplitude because as quantum states they are sensitive to many interactions inside systems. In the context of waveguides, the initial coupling after creation and the thermal effects along the propagation are the main generators of losses [66].

Having explained the quantum states of light, in the next section, we put together the tools we gathered from all previous sections and show the capacity for photonic lattices with topological properties to propagate quantum states such as the squeezed state. In order to present the investigation in a clear and complete way.

# Chapter 4

# Topological photonics

## 4.1. Quantum states of light in coupled mode theory

We will now discuss the relationship between the coupled mode (CMT) and tight-binding theory (TBT), the ability of the former to sustain the evolution of quantum states of light, and the definition of topology for systems with photons.

In Chapter 3, we showed how we could approximate the evolution of the fields inside a waveguide by localized modes that change in amplitude but not in shape, this is the first similarity to tight-binding. The dynamical equation for the paraxial evolution of light in periodic systems bears resemblance to the evolution of spinless massive particles subject to a periodic potential. The key distinction lies in the fact that the spatial coordinate, denoted by $z$, assumes the role of time, represented by $t$. The electric field $\mathbf{E}$ in optics and wavefunction $\mathbf{\Psi}$ in electronic obey the equations

$$i\partial_z \mathbf{E} = \left(-\frac{1}{2k_j}\nabla_\perp^2 + \frac{2k_j}{n_1}\Delta n(x,y)\right)\mathbf{E} \qquad i\hbar\partial_t \mathbf{\Psi} = \left(-\frac{\hbar^2}{2m}\nabla^2 + V(x,y)\right)\mathbf{\Psi} \tag{4.1}$$

Both CMT and TBT approximations are defined analogously, the light (electron) is confined to propagate inside each waveguide (atom) as a bound state which may jump to adjacent waveguides (atoms) proportional to the coupling defined using the evanescent field inside the adjacent waveguides (atoms). CMT can be further expanded to accommodate quantum states by establishing a connection between the annihilation and creation operators of the quantized electromagnetic field and the amplitudes described in (3.11). This extension allows us to apply the paraxial equation to the quantum electric field, resulting in a similar evolution as observed in the classical field.

In CMT each waveguide supports only one mode, then, we can associate each mode $k$ of the field to the waveguide $k$, using this, the total field is now a finite sum of all the waveguides in the lattice. The operator $\hat{a}_j^\dagger(\hat{a}_j)$ creates (destroys) a photon on the waveguide $j$, and the electric field is given by

$$\hat{\mathbf{E}}(r) = \sum_j E(r)_j \hat{a}_j + E(r)_j^* \hat{a}_j^\dagger \tag{4.2}$$

This allows us to define the multimode vacuum as the tensorial product of the number of waveguides, just like equation (3.43) but with a finite number of sub-spaces.
The propagation of quantum light can also be understood by interpreting that each waveguide is a harmonic oscillator whose energy is quantized and each photon has a probability to tunnel over adjacent waveguides proportional to the coupling constant. The corresponding interaction between modes is defined using a tight-binding Hamiltonian where the site energy $\epsilon_0$ is defined using the wave vector $k_j$ of the injected light together with the shape of the mode on the waveguide. The coupling matrix between sites is defined through the classical matrix $V_{ij}$ in equation 2.22 and depends on the injected light, refractive index, and distance between waveguides.
In contrast to electronic systems, photons are bosonic particles, and as such, there can be many particles in the same state (waveguide in this case). This is necessary when working with the squeezed state, which, as a non-linear state, is represented by a superposition of even number states

$$|\xi\rangle = \frac{1}{\sqrt{\cosh r}} \sum_{m=0}^{\infty} (-1)^m \frac{\sqrt{(2m)!}}{2^m m!} e^{im\theta} (\tanh r)^m \, |2m\rangle \tag{4.3}$$

Even though the tight binding is a one-electron model, because our photons are indistinguishable and do not interact with each other, this approximation is valid and we can have many photons in each site, instead of a normalized wave-function probability. Of course, it is always possible to normalize the electric field to yield a normalized probability function given an initial amount of photons assuming the system does not pump in extra photons throughout the evolution. The description above is valid for linear systems, when introducing non-linear interaction between the medium or photons we must take extra steps to describe the full quantum dynamic [67, 68]

## 4.2. Topological photonics

From Chapter 2, we can see that the coupled mode theory uses the same formalism as the tight-binding theory, yielding the same kind of Hamiltonian to describe the low-energy interaction of the system. From equation (4.1), we know that the dynamic equations for each system are analogous, where a spatial dimension in optics takes the role of time, and a periodic refractive index represents the periodic potential in a crystal.
For both we can expand the electric field and wave function as plane and Bloch waves, respectively, finding the band structure of the systems. The difference is that the crystal momentum and energy are replaced by the wave vector and the frequency of the light, respectively. For optics systems, the dynamic variable is defined using a spatial dimension so we need $D + 1$ spatial dimensions in optics to represent the evolution of a $D$ dimension electronic system. There is no traveling back in time for the case of back-scattered light as our systems are smooth enough (in theory and experiment) so that light back-scattered is negligible and does not interfere with the dynamics. All of this together means that

the evolution of photons in a lattice made of waveguides obeys the same dynamic as the evolution of electrons in a lattice of atoms, granting they possess the same geometry. We can also analogously calculate the band structure and topological invariants in photonics systems as in condensed matter. [69, 6]

Does it mean we can replicate electronic systems and phenomena in photonics systems? is the topology defined in the same way for both systems? It does not, and there are two key differences between photonic and electronic systems. The first and most direct is that photons are bosonic particles while electrons are fermionic, this makes a difference in the definition of their statistic, symmetries, and commutators. An example is the time-reversal symmetry which obeys $\mathcal{T}^2 = -1$ for fermions and $\mathcal{T}^2 = +1$ for bosons, and because this relation is necessary degeneracy of the state due to Kramer's theorem, the quantum spin hall effect can not be replicated in photonics. This, however, does not mean that an analog of this system can not be made rather it means that the topology will present itself differently. Topological symmetries and their consequences do not show themself in the same way for electronic and photonic systems. Nevertheless, analogous systems with similar properties can and have been realized without the need to be defined exactly the same [7, 70].

For the SSH model, the chiral operator cannot be defined the same way because the Fermionic commutations are needed for the relation in (1.7). It is sufficient to define a local operator $\hat{\Gamma}$ that satisfies the relation which is the only condition needed for the topological invariant to be well-defined and non-trivial. In our system the topology is defined through the geometry, as long as the refractive index possesses the same periodicity as the tight-binding SSH model, it can be represented in a photonic array of waveguides.

The second difference is the non-equilibrium nature of photons. Typically photons, as non-conservative particles, tend to be absorbed by a medium, scattered by thermal radiation, or just expelled off the system. This means that to maintain light propagating through a system a pump-like mechanism must be put in place, like a laser, nevertheless, there are exceptions to this condition [71, 72, 73, 74]. The non-equilibrium effects also change how the topology is manifested and measured [75]. An experimental consequence for photons is radiation loss which acts as an effective non-hermitian term that has to be taken into account in the replication of electronic systems, but for this effect to take place the light has to propagate long distances. For short enough distances, the pump-like mechanism will maintain the photons inside the waveguide and the radiation loss will be negligible to the dynamics. One consequence of this is that for optics systems, states in the energy bands can be selectively excited by the injected light in comparison to electronic bands where all bands below the Fermi level are occupied. This means that the topological number in photonics is defined for each band which differs from the electronic part where the topological number is defined from the sum of the filled bands while the Fermi energy must be in the energy gap for it to be calculated. Another consequence of the weakly interaction of photons is that measuring time evolution (spatial evolution) or obtaining properties of the photon means that it must be absorbed in some setup, in contrast to electronic systems where the properties can be probed using quantum transport methods.

We can conclude that topology in lattices is not only reserved for electronic systems, but optical lattices made of waveguides will also possess topological properties if the geometry allows it. In the case of the SSH model, the topology will manifest as localization and robustness of the injected light when propagating through the topological state.

# Chapter 5

# Preliminar for the investigation

In this Chapter, we briefly introduce the dimer, trimer and the propagation of squeezed light through them which was studied in [76], this will help us compare and understand the results. Following this, we talk about the effect of topology on the squeezed quadrature and the benefit it provides to the quadrature, following the work in [10]. Ending with the numerical method used for the simulations of squeezed light on photonic lattices for both time-independent and time-dependent Hamiltonians.

## 5.1. Evolution of squeezing on dimer

In this section, we focus on the simplest multi-waveguide setup, the dimer depicted in figure 5.1, consists of two waveguides adjacent to each other, and the trimer, consists of three adjacent waveguides.

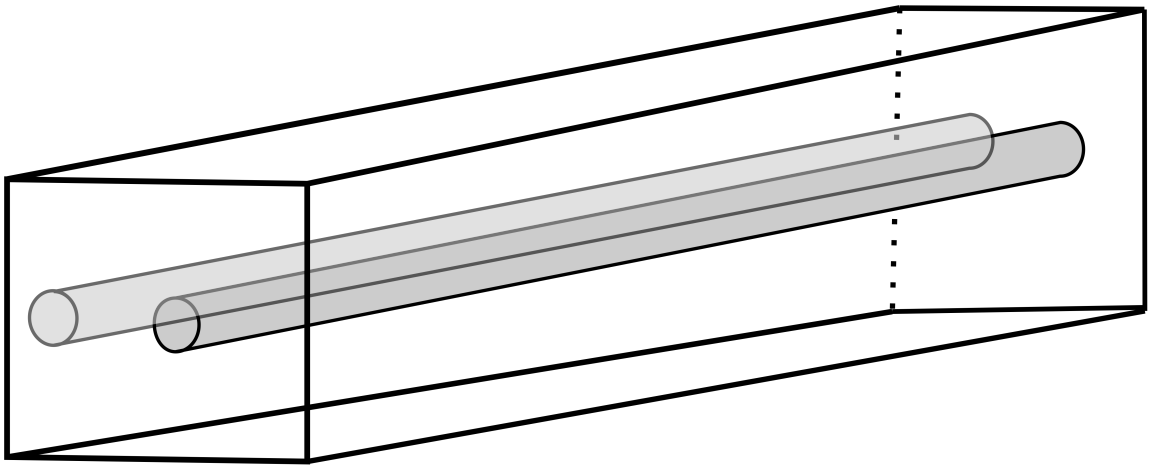

Figure 5.1: Representation of the dimer, two waveguides next to each other.

It can be solved analytically (assuming only linear effects take place) and the solutions are periodic functions that transmit the light back and forth between waveguides. It possesses two modes with opposite phases called the even and odd modes. The periodic transmission

of light when injecting it on one waveguide is due to the excitation of both modes which have different energy ($\beta_{even}, \beta_{odd}$). As light propagates, a phase difference $(\beta_{even} - \beta_{odd})z$ is added, explaining the transmission between waveguides. The trimer has a slightly more complex solution and we omit it here to not overload this section but the general solution for the amplitude when exciting the waveguide $n_0$ of a homogeneous chain with coupling $V$ is $a_n(z) = i^{n-n_0} J_{n-n_0}(2Vz)$ [39], where $J_n(x)$ are the first order Bessel functions, this behavior is known as discrete diffraction.
From a quantum mechanic point of view, the evolution operator of the dimer using the coupled mode theory approximation and the beam splitter operator, respectively, are :

$$\hat{U}_{dimer} = e^{i\kappa z(\hat{a}_0^\dagger \hat{a}_1 + \hat{a}_1^\dagger \hat{a}_0)} \qquad \hat{U}_{BS} = e^{i\theta(\hat{a}_0^\dagger \hat{a}_1 + \hat{a}_1^\dagger \hat{a}_0)} \tag{5.1}$$

Identifying $\theta = \kappa z$ shows the equivalence between both, meaning that a dimer is a beam splitter with its angle defined by the coupling and length of the waveguides.
The propagation of squeezed light in a waveguide dimer and trimer was studied in [76]. In this work, single-mode squeezed light is propagated on a dimer and trimer through all the entries. It is found for the dimer, that the output light on each waveguide can have single-mode, two-mode squeezing, or a mix of the two for both orthogonal quadratures. The output state depends on the coupling and length of the waveguides. For the trimer, generation two and even three mode squeezing is seen depending on the same parameters. They studied the effect of adding losses which diminished the magnitude but not the behavior, and by using different polarization of the light, they managed to control the output as the coupling depends on the polarization for asymmetrical waveguides.

## 5.2. Topological protection of squeezed quadrature

What are the effects of the topology on the properties of a squeezed state when propagating through a topological edge state? Are there any benefits compared to a trivial edge state?
In the work [10], we compared a topological edge state in the SSH with a trivial edge state made by an onsite impurity in a homogeneous chain as depicted in figure 5.2.

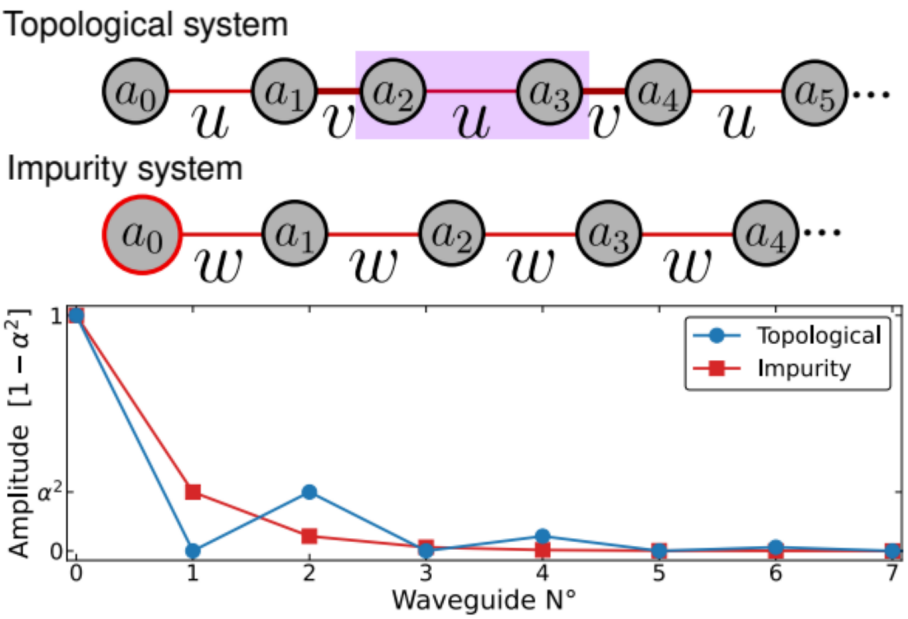


Figure 5.2: The top two images show the topological edge state (T) with the unit cell highlighted and the impurity edge state (I) in a homogeneous lattice. The bottom image shows the eigenstate localized on each of the edges and their distribution on each waveguide. The topological state decays exponentially with weight only on the even sites due to chiral symmetry. The impurity state decays exponentially on each site. Figure taken directly from [10].

When propagating squeezed light throughout them, it was seen that the squeezing inherits the localization of the edge states. Showing, at first sight, no significative difference between both states apart from the sub-lattice localization of the topological state favoring the two-mode squeezing between sites of the same sub-lattice. The difference appears in the presence of coupling disorder, it was seen that the topological state protects the phase of the squeezed quadrature from rotating due to the disorder, in comparison to the trivial state where it rotates randomly as depicted in figure 5.3

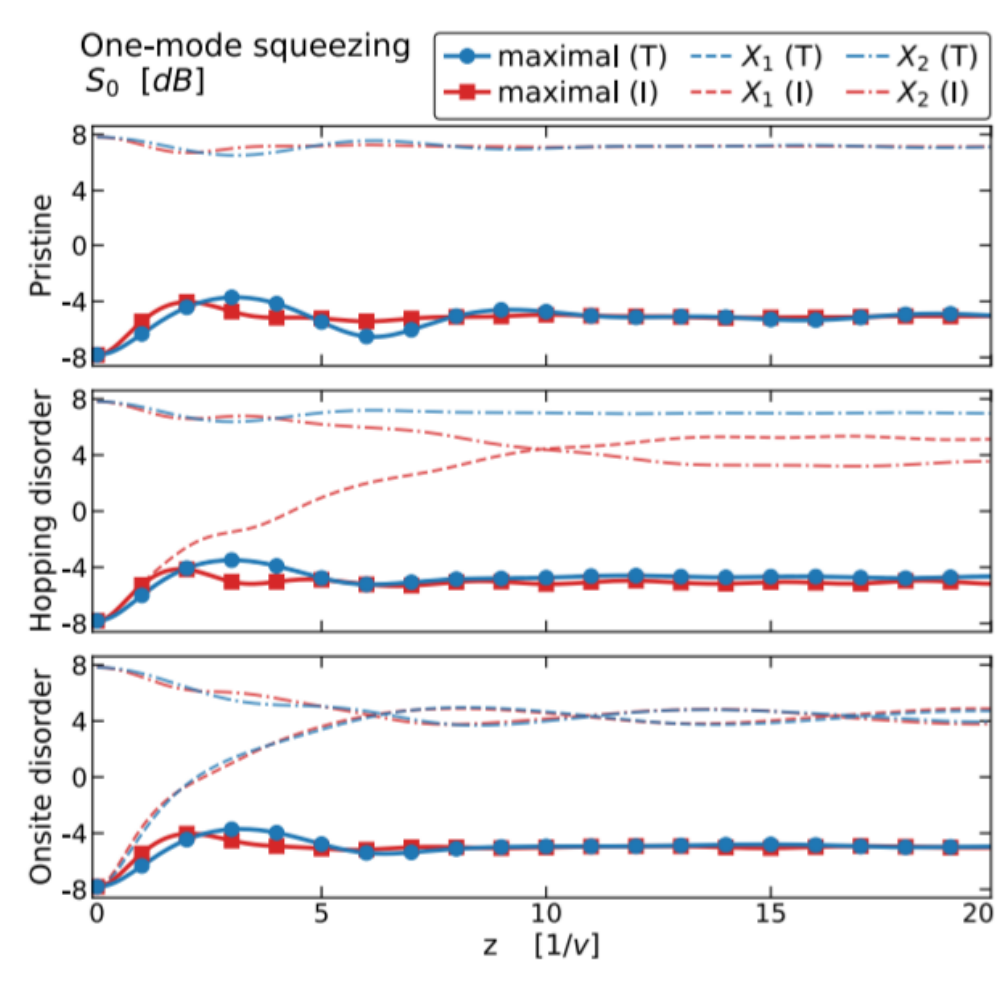


Figure 5.3: Evolution of single-mode squeezing through the topological (T) and the impurity (I) edge states. The initial phase of the quadrature is chosen to be maximally squeezed. The top panel corresponds to a lattice without disorder, and the initially squeezed quadrature persists for both edge states. The middle panel corresponds to a lattice with coupling disorder, the phase of squeezed quadrature starts to rotate for the impurity showing diminishing squeezing on the quadrature we are currently measuring, on the other hand, the topological state does not rotate and the maximally squeezed quadrature remains in the same phase, this is effect of the topology. Last but not least, on-site disorder is added on the bottom panel. It shows the breaking of the topology causing a rotation in the phase of the squeezed quadrature for both types of edge states. Figure taken directly from [10].

This behavior was explained by realizing that the rotation of the phase is due to the energy of the state, which remains at zero for the topological system even in the presence of disorder while it varies randomly for the trivial state. This property was exploited to enhance a teleportation protocol using two-mode squeezed state [63]. In the presence of coupling disorder, it was observed that the topological edge state possessed a much greater fidelity in the received message compared to the trivial state due to the locking of the squeezed quadrature, asserting the benefits of using topologically protected squeezed light in the protocol.

Because we would like to exploit this property, we now comment on the two types of domain walls an SSH model can host, one type is between two coupling $u$, and the other type is between two coupling $v$. As seen in figure 1.9, the latter possesses two trivial states and two topological states localized on and around the domain wall. This means that injecting squeezed light in the domain wall or neighbor sites will excite all four states, causing a beating of the light between them [77]. In our system, this will cause the squeezed quadrature to rotate as the trivial states does not have zero energy. To exploit the zero energy states, we only study the propagation of squeezed light in a domain wall between couplings $u$ which only hosts topological states and the squeezed phase is locked.

## 5.3. Evolution of expectation values on photonic lattices

The squeezing is proportional to the uncertainty of the quadrature, to obtain this, we need to calculate:

$$\langle \Delta \hat{X}_{i,j}(\phi) \rangle^2(t) = \langle \hat{X}_{i,j}(\phi)^2 \rangle(t) - \langle \hat{X}_{i,j}(\phi) \rangle^2(t) \tag{5.2}$$

for both orthogonal quadratures. For this, we use the time-dependent Trotter-Suzuki algorithm [78] and exploit the linearity of the Hamiltonian to compute the evolution, even for time-dependent Hamiltonians.
We start by considering a general linear Hamiltonian which can be written as

$$\hat{\mathcal{H}} = \sum_{m,n} H_{mn} \hat{a}_m^\dagger \hat{a}_n, \tag{5.3}$$

$H_{mn}$ is the matrix containing the site's energies and coupling in real space, which correspond to the diagonal and non-diagonal matrix elements, respectively. In the Heisenberg picture, the evolution of an operator $\hat{Y}$ is given by the equation

$$\frac{d\hat{Y}}{dt} = i[\hat{\mathcal{H}}, \hat{Y}], \tag{5.4}$$

for time-independent Hamiltonians, this equation has solutions of the form

$$\hat{Y}(t) = \hat{U}^\dagger(t_0, t) \hat{Y}(t_0) \hat{U}(t_0, t), \tag{5.5}$$

with $\hat{U}(t_0, t) = \exp\Big\{-i \int_{t_0}^{t_0+t} \hat{\mathcal{H}}(s) ds\Big\}$.
The evolution for the operator $\hat{a}_j$ in the Heisenberg picture is given by

$$\hat{a}_j(t) = e^{ib\hat{\mathcal{H}}} \hat{a}_j e^{-ib\hat{\mathcal{H}}} = (e^{ib\sum_{m,n} H_{mn}\hat{a}_m^\dagger \hat{a}_n}) \hat{a}_j (e^{-ib\sum_{m,n} H_{mn}\hat{a}_m^\dagger \hat{a}_n}), \tag{5.6}$$

where $b$ is a real constant depending on time. By using the BCH relation (3.56) this expression can be reduced to

$$e^{ib\mathcal{H}}\hat{a}_j e^{-ib\mathcal{H}} = \sum_n e^{-ibH_{jn}}\hat{a}_n. \tag{5.7}$$

This relation can be used to calculate the evolution in the Heisenberg picture for any operator defined in terms of the ladder operators for a time-independent Hamiltonian. The calculation of the expectancy or variance is straightforward given the initial state.

Now we focus on treating a time-dependent Hamiltonian, meaning that the matrix $H_{mn} = H_{mn}(s)$ can depend on the time $s$. The evolution from $t_0$ to $t_0 + t$ is determined by the evolution operator satisfying the equation $\frac{d}{dt}U(0,t) = -iH(t)U(0,t)$, with the solution given by the time-ordered integral

$$\hat{U}(t_0,t) = \mathcal{T}\exp\Big\{\int_{t_0}^{t}\hat{H}(s)ds\Big\}, \tag{5.8}$$

this expression can be approximated, even for time-dependent Hamiltonian, as a series of small steps using an infinitesimal time-evolution operator [78]

$$\hat{U}(t_j, t_j+\Delta t) \approx \exp\left\{-i\int_{t_j}^{t_j+\Delta t}\hat{\mathcal{H}}(s)ds\right\} = \exp\Big\{-B(t_i,\Delta t)_{mn}\,\hat{a}_m^\dagger\hat{a}_n\Big\}) \tag{5.9}$$

with $B(t_i,\Delta t)_{mn} = i\int_{t_i}^{t_i+\Delta t}H(s)_{mn}ds$. The evolution of a state is approximately given by

$$|\Psi(t)\rangle \approx \prod_{j=0}^{N-1}\hat{U}(t_j, t_j+\Delta t)\,|\Psi(t_0)\rangle\,, \tag{5.10}$$

where $N$ is the number of steps and $\Delta t$ the step size satisfying $\Delta t = (t-t_0)/N$. Using equation (5.7), the infinitesimal evolution of an operator in the Heisenberg picture is

$$\hat{a}_m(t_i+\Delta t) = \hat{U}^\dagger(t_i, t_i+\Delta t)\hat{a}_m(t_i)\hat{U}(t_i, t_i+\Delta t) \tag{5.11}$$

s

$$= \sum_n \exp\{-B(t_i,\Delta t)\}_{mn}\hat{a}_n(t_i) = \sum_n U(t_i, t_i+\Delta t)_{mn}\hat{a}_n(t) \tag{5.12}$$

where $U(t_i, t_i+\Delta t)_{mn} = \exp[B(t_i,\Delta t)]_{mn} = \exp\Big(i\int_{t_i}^{t_i+\Delta t}H(s)ds\Big)_{mn}$ is a squared matrix with the same size of the system. Using this method, it is possible to compute the expectancy and variance evolution of any combination of ladder operators as long as the initial state possesses an initial matrix representation and the system has a linear Hamiltonian of the form (5.3).

To characterize how much a quadrature is squeezed using equation (5.2), we use the decibel formula in equation (3.62). The one-mode quadrature and two-mode quadrature of states fulfilling $\langle\psi_0|\,\hat{a}_{i,j}\,|\psi_0\rangle = 0$ and $\langle\psi_0|\,\hat{a}_{i,j}^\dagger\,|\psi_0\rangle = 0$, means that the evolution of the variance will be completely dictated by $\langle\hat{X}_{ij}^2\rangle$, which can be computed from the following relations for

both single and two-mode quadratures as

$$A_{ij}^{(1)}(t) = \langle\psi(t)|\,\hat{a}_i\hat{a}_j\,|\psi(t)\rangle = \langle\psi(t_0)|\,\hat{U}^\dagger(t_0,t)\hat{a}_i\hat{a}_j\hat{U}(t_0,t)\,|\psi(t_0)\rangle \tag{5.13}$$

$$A_{ij}^{(2)}(t) = \langle\psi(t)|\,\hat{a}_i^\dagger\hat{a}_j\,|\psi(t)\rangle = \langle\psi(t_0)|\,\hat{U}^\dagger(t_0,t)\hat{a}_i^\dagger\hat{a}_j\hat{U}(t_0,t)\,|\psi(t_0)\rangle \tag{5.14}$$

$$A_{ij}^{(3)} = \langle\psi(t)|\,\hat{a}_i\hat{a}_j^\dagger\,|\psi(t)\rangle = A_{ji}^{(2)} + \delta_{ij} \tag{5.15}$$

$$A_{ij}^{(4)} = \langle\psi(t)|\,\hat{a}_i^\dagger\hat{a}_j^\dagger\,|\psi(t)\rangle = (A_{ji}^{(1)})^\dagger, \tag{5.16}$$

Each one can be expressed as a multiplication of matrices, by finding the BCH transformation of the operator using the linear Hamiltonian, in this case, it yields the evolution

$$A_{ij}^{(1)}(t) = \sum_{m,n}\prod_{k=0}^{N-1} U_{im}(t_k, t_k+\Delta t)A_{mn}^{(1)}(t_0)U_{nj}^T(t_k, t_k+\Delta t) \tag{5.17}$$

$$A_{ij}^{(2)}(t) = \sum_{m,n}\prod_{k=0}^{N-1} U_{im}^\dagger(t_k, t_k+\Delta t)A_{mn}^{(2)}(t_0)U_{nj}^T(t_k, t_k+\Delta t) \tag{5.18}$$

where $T$ is the transpose and $\dagger$ is the transpose conjugate. These equations tell us that by recursively multiplying the time evolution matrix $U(t_i, \Delta t)$ to both sides of the initial matrix $A_{mn}^{(j)}(t_0)$ at each time, we can compute the total evolution and, by taking the correct matrix elements we can get both one-mode and two-mode squeezing in and between waveguides.
These relations are theoretical and are only limited by intrinsic numerical errors. That does not mean that the total evolution is exact, because we are using the trotter algorithm to approximate the evolution operator it is necessary to define a time-step shorter than the fluctuation of the Hamiltonian *i.e*, $\Delta t \ll ||\partial H/\partial t||$. Our system satisfies $||\partial H/\partial t|| \approx 10^{-1}|u-v|$, defining the trotter step-size as $\Delta t = 10^{-3}$ relative to the coupling values $(u, v) \propto 10^0$, will be enough to simulate the evolution accurately.

# Chapter 6

# Manipulation of squeezed light in an SSH model with adiabatic modulation

To fully understand the results, the setup has to be clear. For this, the beginning of this chapter is reserved to explain how to move the domain wall, the parameters controlling the quality, and the limits of the modulation. Once this is understood, we present the initial conditions which are the injected light, and how we study the effects of the disorder. The chapter is finalized by presenting the results of the evolution, the behavior observed, and the robustness of the states.

The results of this thesis focus on manipulating squeezed light in a photonic array of waveguides with topological properties, understanding what benefits the topology brings, and what are the limits.

To do this, we inject two single-mode squeezed lights onto two separated topological domain walls. Then, by using a time-dependent Hamiltonian, we locally change the coupling around each domain wall and move them together as depicted in figure **??**. After the modulation, both domain walls remain together for a fixed period of time, called time of interaction. After this, the inverse modulation begins. the domain walls are separated and taken back to their original waveguides. We see that the properties and transmission of the output states depend on the time of interaction $T_{int}$, the smoothness of the modulation $T_M$, and the initial band gap $\Delta$C(g).

The output states, which are physically apart and possess topological properties, have single-mode or/and two-mode squeezing, depending on the interaction length $T_{int}$ for a fixed modulation $T_M$ and band gap $\Delta$C(g). The same is seen when injecting three single-mode squeezed light into three domain walls. The behavior of the output squeezing at the two and three domain walls for different interaction lengths is analogous to the evolution of single-mode squeezed light in a two and three-waveguide system, as talked about in the previous section. In our system, because the Hamiltonian is linear and the squeezing is generated through a non-linear interaction, the total injected squeezing magnitude acts as a conserved quantity. This means that any loss in the output states is due to coupling and scattering to the bulk. We do not consider any other type of loss effect.

## 6.1. Details of the coupling modulation

In the modulation, each domain wall is moved across the lattice using the mechanism 1.10 described at the end of Chapter 1. It is represented in waveguides in figure 6.1, where the couplings $u$ and $v$ are inversely proportional to the distance between waveguides.

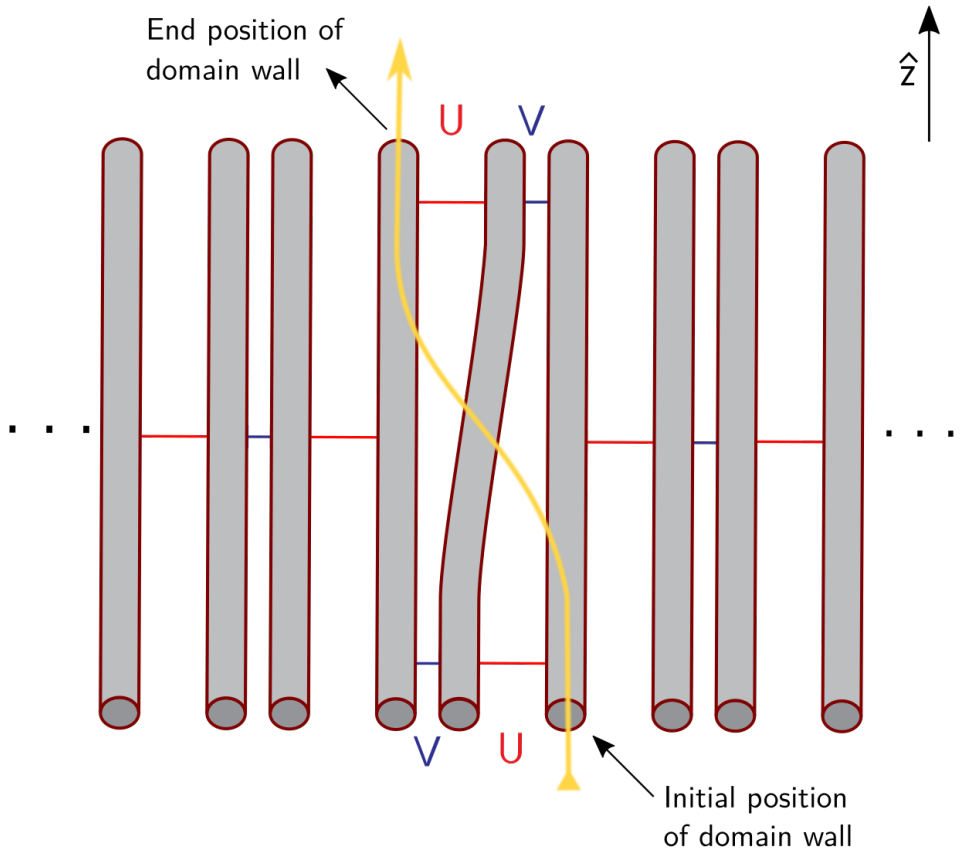


Figure 6.1: Coupling modulation represented in waveguides that moves the domain wall two sites to the left. The yellow line shows the evolution of light through the system when injected on the domain wall.

In the first part of the evolution, the two nearest coupling in the direction of the movement varies with length in which the modulation in figure 6.1 is repeated the number of times necessary for the domain walls to get next to each other, this process is depicted in figure 6.2 and it takes a total length of $T_M$. As we will see, varying the total length affects the quality of the modulation. At the end of this, the domain walls are at the middle point between their original location and have a coupling $u$ between them. Because the system is still in a topological phase, the coupled domain walls host localized states, which prevents light from scattering to the bulk while permitting the light to propagate between them. After a length $T_{int}$, which defines the length of interaction between the domain walls.

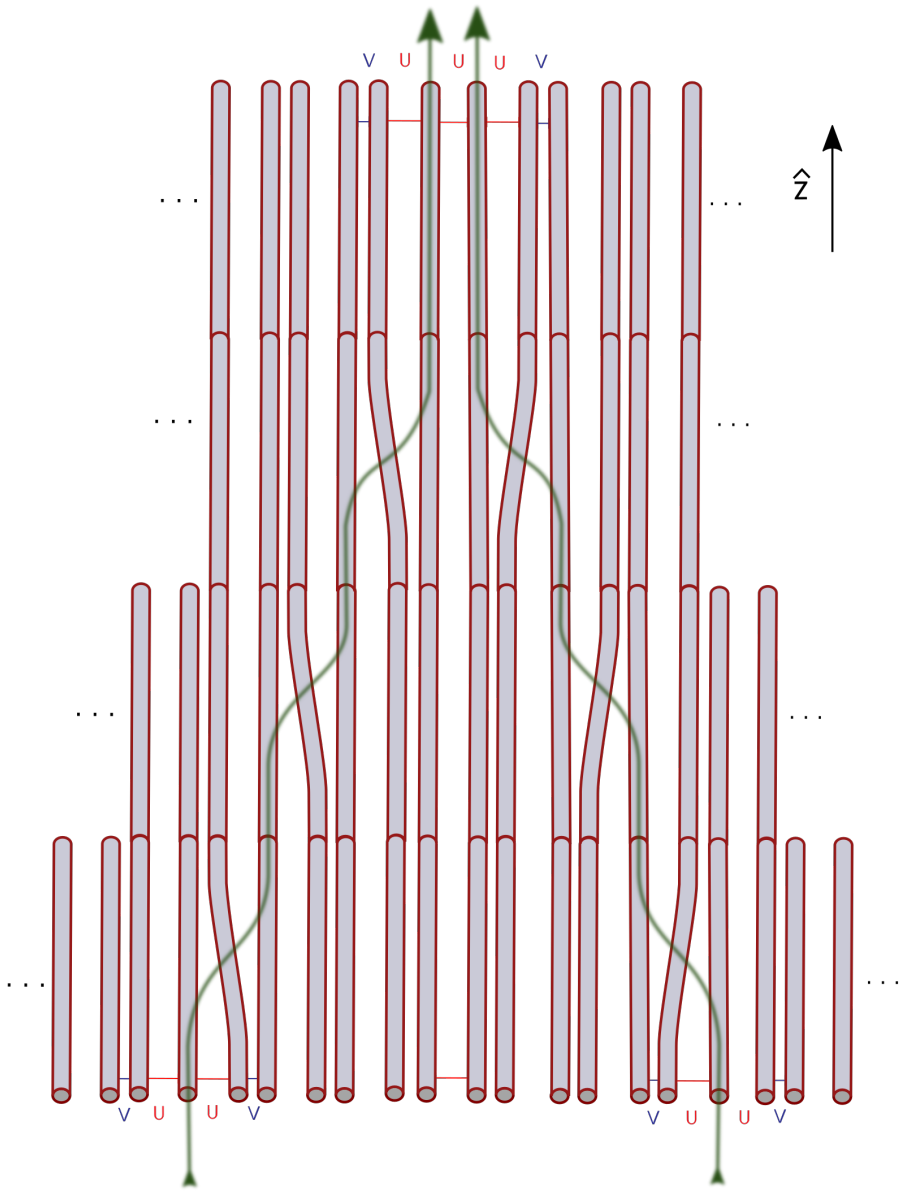


Figure 6.2: Example of half the evolution, the domain walls are "moved" until coupled. The black box shows the modulation in 6.1, by repeating the process the domain wall is "moved" across the system guiding the light. The green arrow shows the evolution of the light when injected into the domain walls.

By doing the inverse process of the initial modulation, the domain walls are separated and returned to their original waveguides. After this, the output light at both domain walls is studied. The whole evolution is represented in figure 6.3, the domain walls are coupled and then returned to their original positions.

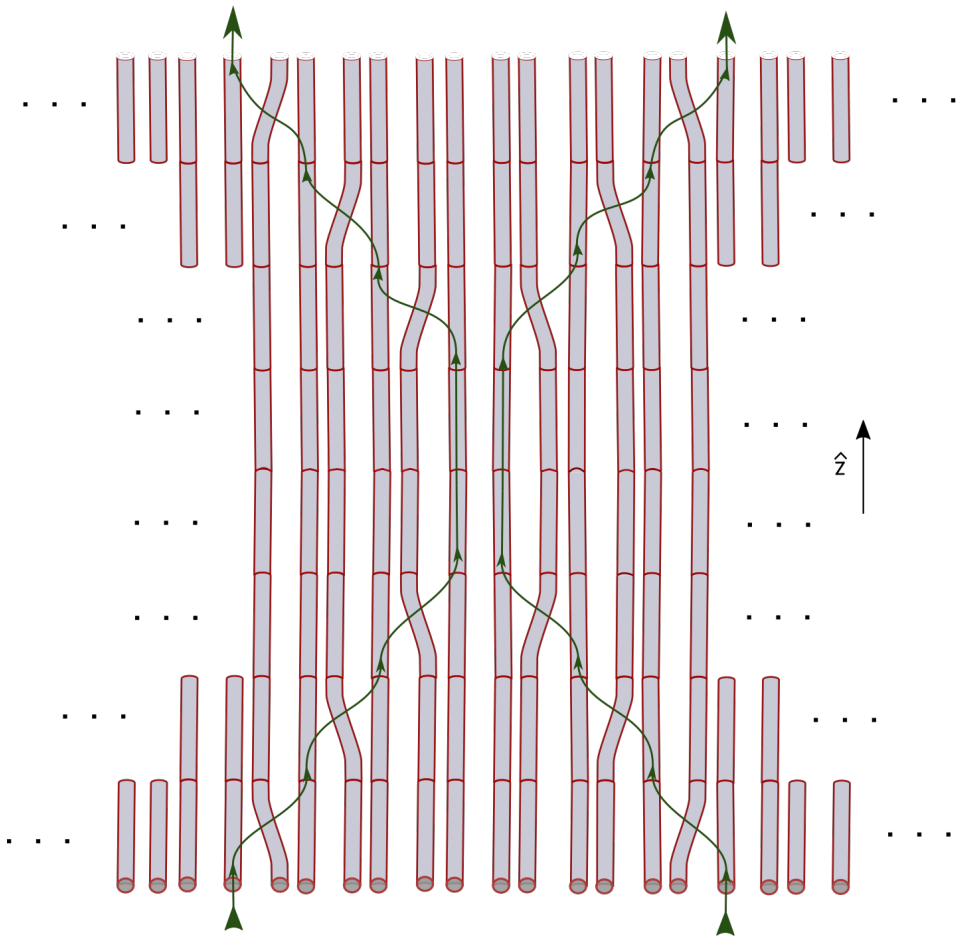


Figure 6.3: Example of full evolution, the domain walls are coupled for a fixed length and then returned to their original positions. The green arrows show the path taken by the light when injected on the domain wall.

To modulate the coupling, we use the hyperbolic tangent function because of its smoothness and convenience as a switch function, its integral is also convenient when defining an infinitesimal step.
For convenience, the order of the coupling is $\mathrm{v}_{order}$ is proportional to $\mathrm{u}_{order}$ so that the order of magnitude is defined by one variable. The length dependence of the coupling is defined as

$$\mathrm{v}_{order} = \mathrm{u}_{order} + g \cdot \tanh(1) \tag{6.1}$$

$$\mathrm{v}(t) = \mathrm{u}_{order} + g \cdot \tanh\left(1 - \frac{(t - t_0)}{t_m}\right) \tag{6.2}$$

$$\mathrm{u}(t) = \mathrm{u}_{order} + g \cdot \tanh\left(\frac{(t - t_0)}{t_m}\right) \tag{6.3}$$

where $t_0$ is the initial length and $t_m$ is the length of each cycle of modulation, depicted in figure 6.1, and is defined as $t_m = T_M/|\Delta P|$ where $T_M$ is the total duration of the modulation and $\Delta P = |P_b - P_a|/2$ is the number of sites between the domain walls which is fixed. This

form for $t_m$ is chosen to simplify the control over the modulation because of two reasons. First, $T_M$ helps to control how long is the modulation compared to the whole evolution and, second, $\Delta P$ defines the minimum number of cycles you need to move each domain wall to reach the middle. When considering three domain walls, the number of sites is defined using the distance between the middle and one of the lateral domain walls. Using this definition the parameter $g$ determines the size of the energy gap 1.2 while $\mathrm{u}_{order}$ sets the order of magnitude of the system. The band gap of the system with this definition is

$$\Delta C(g) = |\mathrm{v}_{order} - \mathrm{u}_{order}| = g \cdot \tanh(1) \tag{6.4}$$

These will allow us in the next section to control the quality of the modulation using the values $T_M$ and $g$, while $u_{ordere}$ sets reference for the system's energies.

## 6.2. Parameters of the system

We study an SSH model with a total of 30 waveguides possessing two domain walls in the positions $p_a = 11$ and $p_b = 20$, details of the system can be seen in appendix **??**. We inject single-mode squeezed light with a magnitude of $r = 0.5$ and phase $\theta = 0$ on both domain walls. This translates, in the decibel formula, to approximately -4.34 dB of squeezing. We define the length of interaction proportional to the energy gap $\Delta C(6) = \Delta E$ and varies from $2\Delta E$ to $3\Delta E$ which, for all cases, is enough to see at least one full cycle of the behavior. The output squeezing is studied by taking the mean output on the domain walls considering different lengths of interaction $T_{int}$ for a fixed band gap $\Delta C$ and a modulation length $T_m$.
The relation between the modulation time and the band gap defines how good the modulation can be, for smaller band gaps we need larger modulation times, and vice versa. For this reason and to maintain a common order of magnitude when simulating the system, we chose the value $\Delta E$ and explored the system's reaction to changes on this order of magnitude.
We study the output squeezing for varying band gaps using the values $g = (3,\ 6,\ 9,\ 12)$ in combination with the modulation lengths $T_M = (\Delta E,\ 2\Delta E,\ 3\Delta E,\ 4\Delta E)$. These values are chosen because they define the limits of the behavior. The band gap $g = 3$ shows, for all cases, a poor behavior, setting the lower limit for the band gap, and values greater than $g = 12$ show little to no difference in the behavior, setting the upper limit. The modulation length $T_M$ is proportional to $\Delta$E. It is defined this way to match the band's gap order of magnitude, this allows us to get the lower limit where the effective behavior is lost.
We start by presenting the dependence of the output states on the energy gap and modulation length. After this, we present the interaction of three initial localized states with the same conditions.

## 6.3. Two domain walls interacting

For the two domain walls interesting, the correct phase to measure two-mode squeezing is $\phi = (2n+1)\frac{\pi}{4}$. We take the angle from the analysis in [76] but it can be directly obtained by studying the correlation matrix defined for a Gaussian state, such as the squeezed state, or from the Wigner function [3].

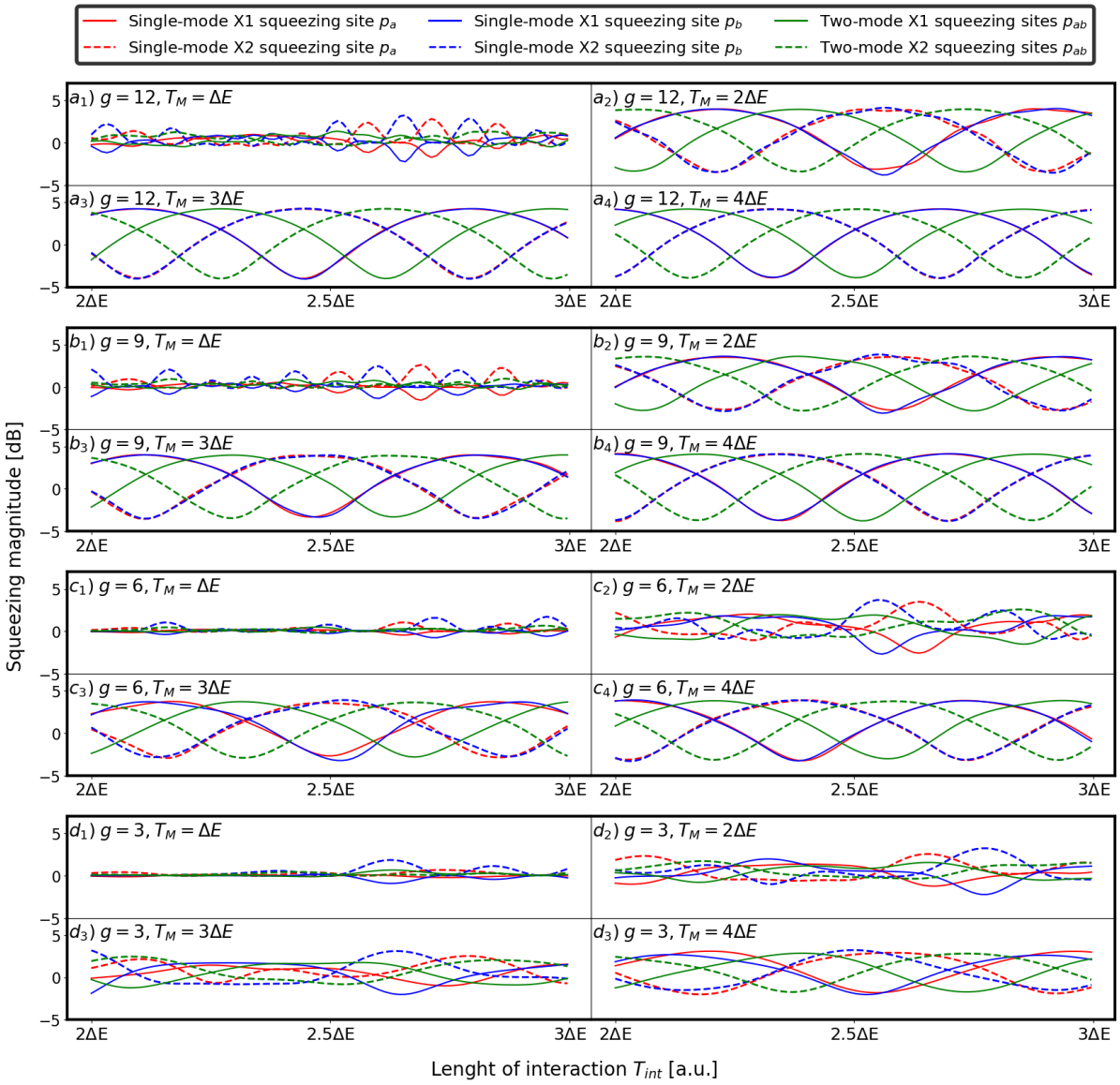


Figure 6.4: Output squeezing of two interacting domain walls. Each figure shows the single and two-mode squeezing output on each domain wall versus the length of interaction for different combinations of modulation lengths and band gaps. Each letter shows a different band gap while each number represents a different modulation time. We have the band gap sizes: $a_i)$ $g = 12$ , $b_i)$ $g = 9$ , $c_i)$ $g = 6$ and $d_i)$ $g = 3$. The index $i$ ranges from 1 to 4 representing the modulation lengths: 1) $T_M = \Delta E$, 2) $T_M = 2\Delta E$, 3) $T_M = 3\Delta E$ and 4) $T_M = 4\Delta E$.

We can see from all images in figure 6.4, by varying the length of interaction the output squeezing at the domain walls changes from single-mode squeezing to two-mode squeezing as a dimer would. The period of each oscillation is fixed and depends on the coupling of the joint domain walls but has a translation on the x-axis depending on the modulation length. Figures in $d$) show that a band gap of $g = 3$ is too low to achieve a successful modulation which translates into a low squeezing transmission (relative to the injected squeezing) and poor behavior (analogy to a dimer). As we increase the band gap, we can see in figures $a_i$), $b_i$), and $c_i$) that, for larger modulation lengths, the output squeezing behaves well and has high transmission. However, this is not valid for the shortest modulation time which does not behave well for all band gaps. In general, the bigger the combination of band gap and modulation time, the better the modulation and the lesser losses but we can see in the figures that good dimer behavior is seen for almost all cases, only diminishing in magnitude at the output by a maximum of 30% and in the best case the loss is lower than 10%. The band gap $g = 3$ and modulation length $T_M = \Delta E$ define the minimum possible values to accurately replicate the behavior of a dimer.

## 6.4. Three domain walls interacting

To study three interacting domain walls, we consider a system of size $n = 31$, with domain walls in the positions $p_a = 9$, $p_b = 16$, and $p_c = 23$. The chosen values for the band gaps and modulation lengths are the same as the dimer. In this case, the two-mode squeezing is measured at the quadrature phases of $\phi_{ab} = \frac{3\pi}{4}$, $\phi_{bc} = \frac{3\pi}{4}$ and $\phi_{ac} = \frac{\pi}{2}$.

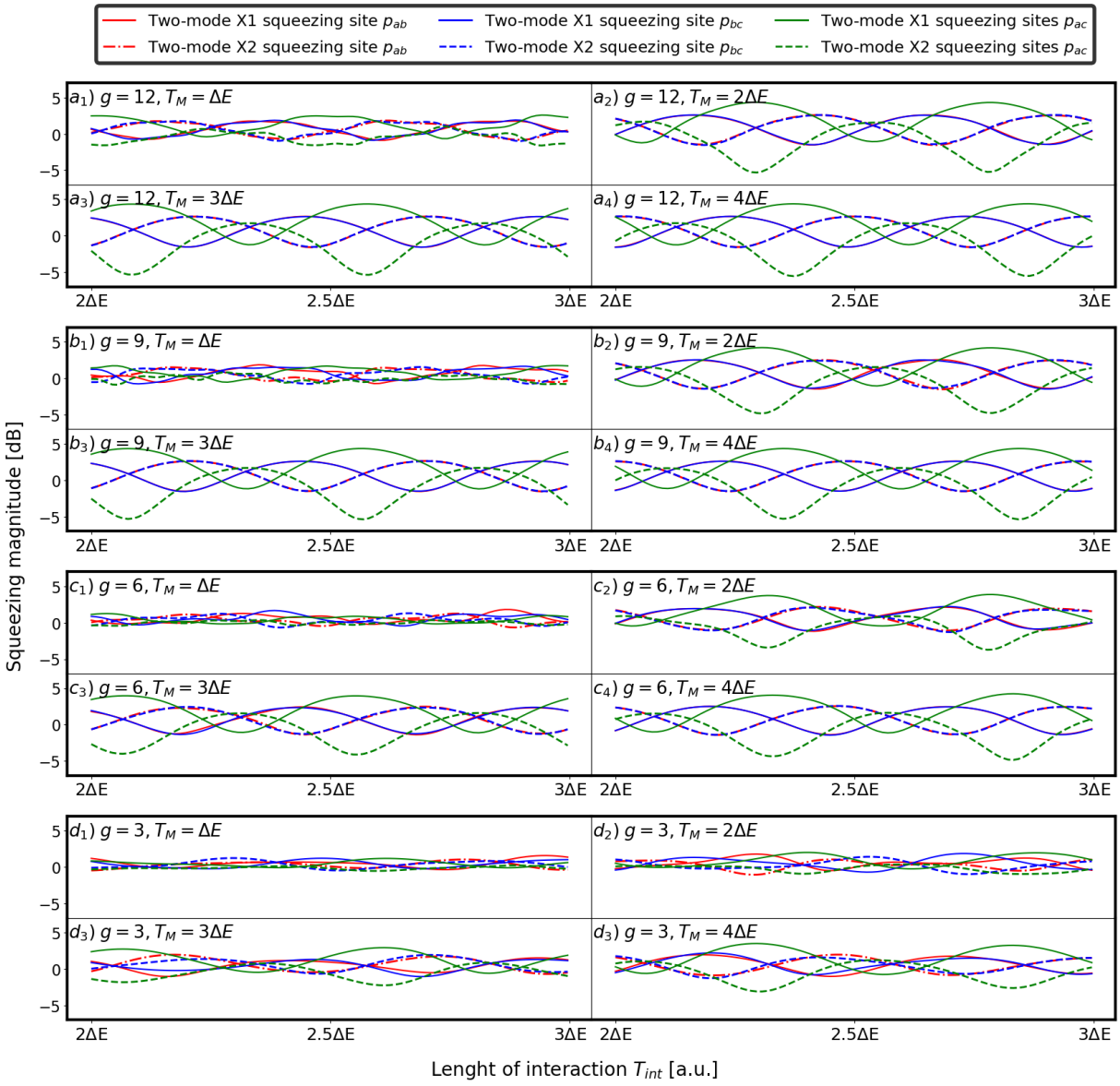


Figure 6.5: Output squeezing of three interacting domain walls. Each figure shows the output two-mode squeezing on each domain wall versus the length of interaction for different fixed values of modulation lengths and band gaps. Each letter shows a different band gap while each sub-index represents a different modulation time. We have the band gap sizes: $a_i$) $g = 12$ , $b_i$) $g = 9$ , $c_i$) $g = 6$ and $d_i$) $g = 3$. For each letter we have the index $i$ ranging from 1 to 4 representing the modulation lengths: 1) $T_M = \Delta E$, 2) $T_M = 2\Delta E$, 3) $T_M = 3\Delta E$ and 4) $T_M = 4\Delta E$.

Just like two domain walls, by changing the length of interaction we can output two-mode squeezing between each domain wall. For certain lengths, we can even get three-mode squeezing as the single and two-mode squeezing is zero just like in [76]. From figures in $d$), just like the dimer, this band gap size is not enough for a good modulation, losing the effective trimer behavior. As we increase the band gap, the behavior and transmission get better at replicating the trimer. For the shortest modulation length $T_M = \Delta E$, the behavior is lost for all band gaps. Nevertheless, good behavior is seen for almost all cases, only changing the magnitude of the output squeezing by less than 30%. Just like in the previous case, the bigger the band gap and the modulation lengths, the better the behavior and transmissivity of the injected squeezing.

## 6.5. Topological protection for two and three domain walls

Different levels of the disorder are added to the couplings $(u, v)$ and on-site energy $(\epsilon_0)$ to visualize the benefits the topology grants. The disorder is proportional to the coupling difference, a uniform random distribution between $-1, 1$ called $r[-1, 1]$ and a $\delta$ parameter that manages the disorder's magnitude.

$$d = |u - v| \cdot \delta \cdot r[-1, 1] \tag{6.5}$$

$$u(d) = u + d \tag{6.6}$$

$$v(d) = v + d \tag{6.7}$$

$$\epsilon_0(d) = d \tag{6.8}$$

As seen in figures 6.4 and 6.5, the behavior is lost for band gap of size $g = 3$ and modulation length of $\Delta$E, we omit these cases as the introduction of disorder will not improve them.
The disorder in the site energies must be placed on the even or odd sites in order to break the chiral symmetry. We chose the even sites but there is no difference in using odd sites.
We added disorder to the systems with the largest modulation length while varying band gap. This means we are testing the topology at different band gaps, we did this because it is the condition directly related to the coupling magnitude and the most prone to fluctuations due to disorder. The following figures show the output squeezing when adding 10% ($\delta = 0.1$) of coupling and on-site disorder for different band gap sizes and fixed modulation time of $4\Delta$E. This magnitude of disorder is big for waveguides which typically present a disorder of 1% in their fabrication. We made 50 realizations to study the disorder for each case.

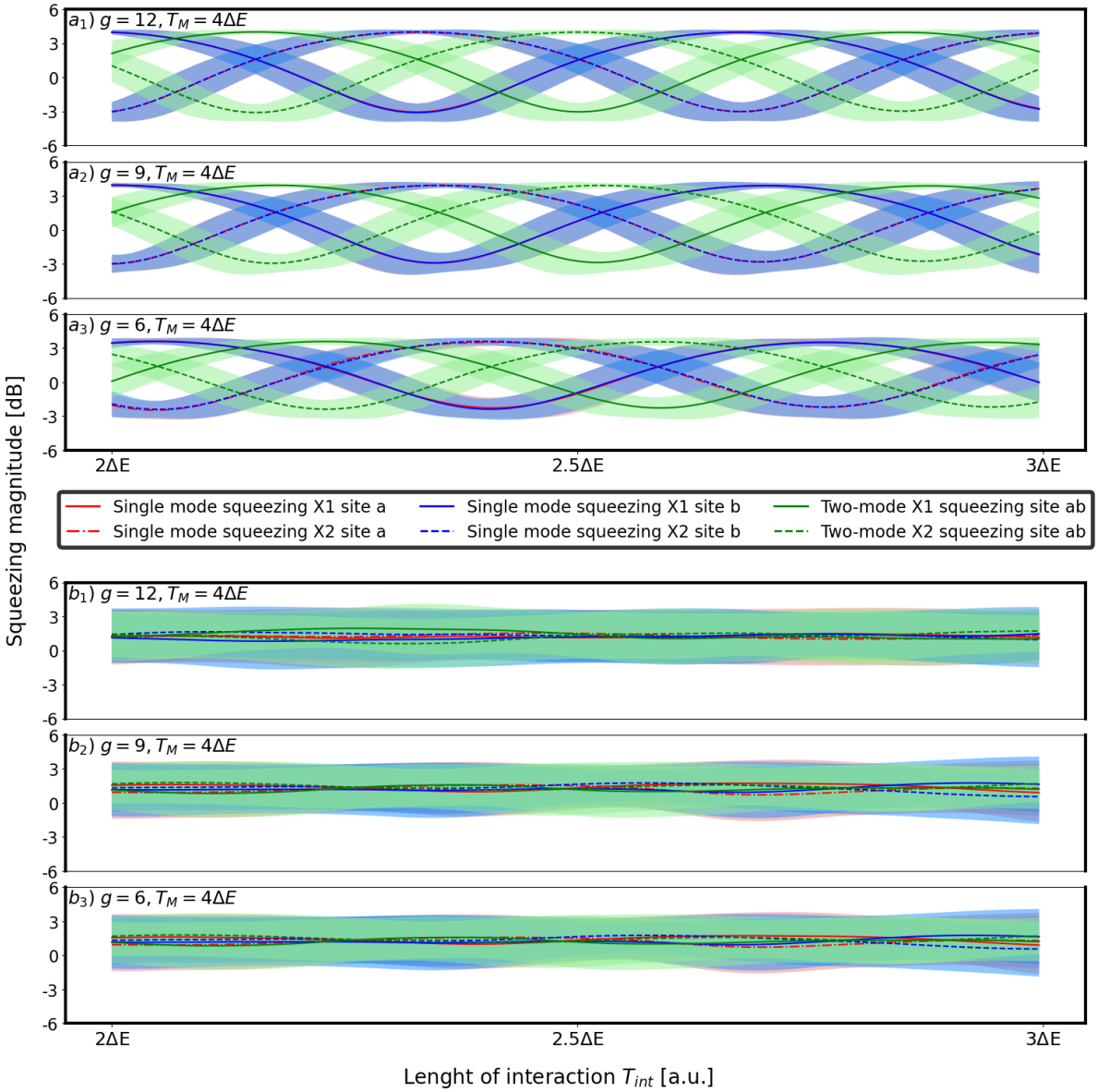


Figure 6.6: Output squeezing of the two interacting domain walls with coupling and on-site disorder. The disorder is of the same magnitude $\delta = 10\%$. The top three images $a_1), a_2), a_3)$ show the effect of coupling disorder. The bottom three images $b_1), b_2), b_3)$ show the effect of on-site disorder. The modulation length is maintained constant at $T_M = 4\Delta E$ while the band gap takes the values of $g = 6, 9, 12$.

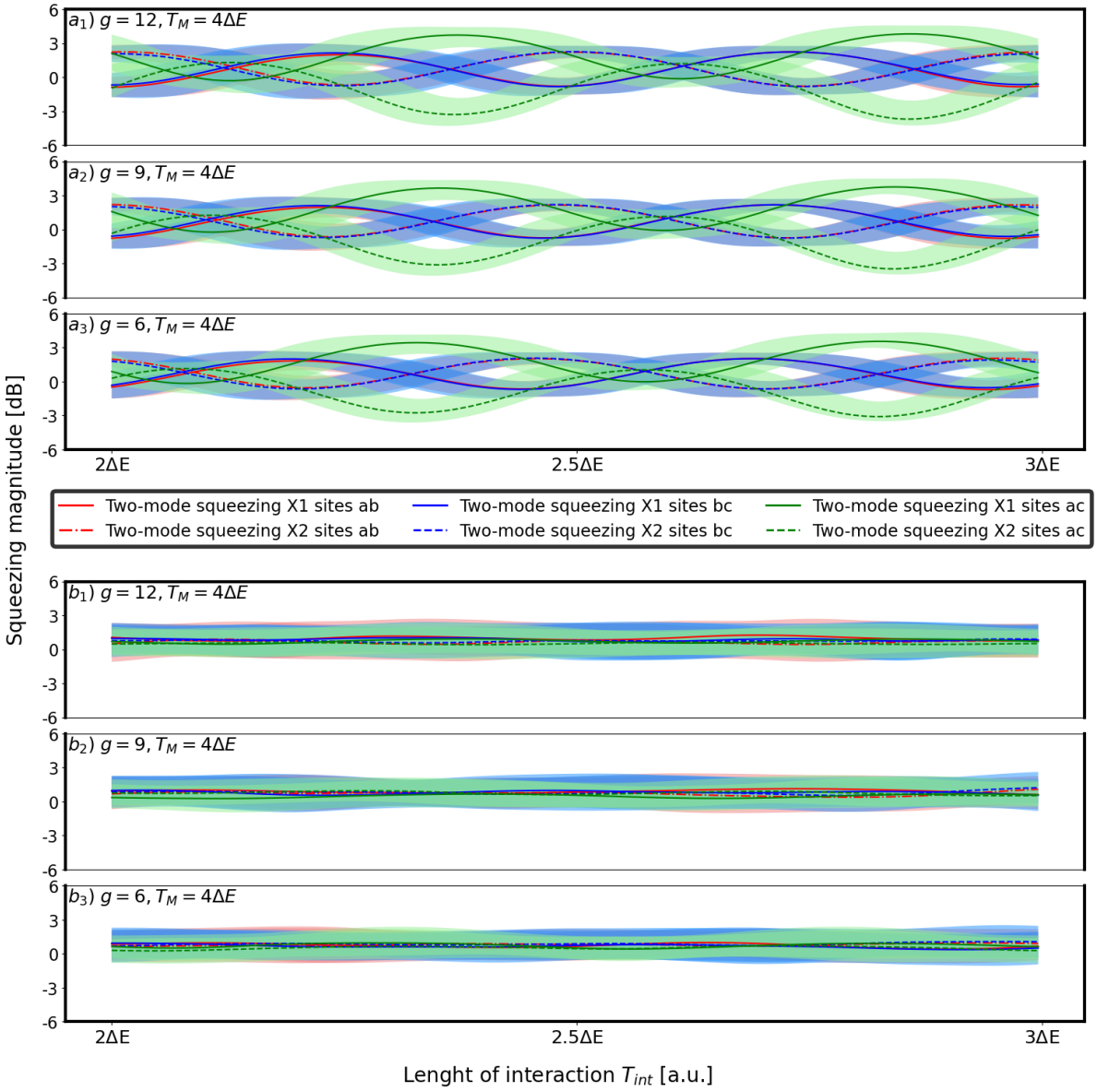


Figure 6.7: Output squeezing of three interacting domain walls with coupling and on-site disorder. The disorder is of the same magnitude $\delta = 10\%$. The top three images $a_1), a_2), a_3)$ show the effect of coupling disorder. The bottom three images $b_1), b_2), b_3)$ show the effect of on-site disorder. The modulation length is maintained constant at $T_M = 4\Delta E$ while the band gap takes the values of $g =$ 6, 9, 12.

The top three images in figure 6.6 show the behavior of a dimer, this is proof of the topological protection. The coupling disorder does not break the sub-lattice symmetry and the domain walls remain, protecting the propagation and localization of the squeezing against it. There are more losses as the scattering to the bulk is increased in the modulation length by the disorder. In figure 6.7, we see a trimer behavior but, like for the dimer, with less magnitude. This is due to the scattering to the bulk as the modulation initial and final points are

imperfect with the added disorder, increasing the band gap or modulation length will increase the transmitted magnitude and quality of the effective trimer. In contrast, adding on-site disorder to both systems break the symmetry and, in consequence, the domain walls, meaning all output squeezing is scattered to the bulk and lost.

# Chapter 7

# Conclusions

We conducted a study on the evolution of squeezed light in a one-dimensional topological system known as SSH, with two domain walls hosting topological states. By manipulating the couplings adjacent to the domain wall, we successfully brought the states closer together, resulting in an interaction between the domain walls. This interaction can be seen as the evolution of an effective dimer or trimer, depending on the number of domain walls involved. Our analysis of the response to coupling disorder revealed that the topological domain wall remains protected throughout the evolution. Although the output squeezing diminished in magnitude due to scattering to the bulk caused by the disorder, the behavior of the output squeezing remained mostly consistent. However, the introduction of on-site disorder disrupted the states and scattered the squeezing throughout the system, thereby nullifying the effectiveness of the effective dimer and trimer. This confirmation of topology protection demonstrates that the quantum properties of the squeezed state are preserved throughout the evolution of moving domain walls. As a side note, the percentage of on-site disorder we selected is significantly larger than what is typically found in real-life waveguide systems. However, it's important to note that even a small amount of on-site disorder could potentially disrupt the states in theory. Nevertheless, in practice, the behavior should still remain within a certain limit. It's also important to consider the edge states in this context since the system is always in a topological phase. These edge states can be leveraged to inject or maintain light during the evolution, thereby opening up possibilities for simulating various systems such as interferometers and quantum protocols that exploit the system's topology. Our investigation highlights the advantages of utilizing topological domain walls for the communication and movement of squeezed light through time-dependent couplings. This approach enhances the interaction between quantum states while minimizing scattering and preserving quantum properties. The topological protection allows for imperfections in the coupling, enabling consistent behavior even in the presence of poorly distanced but similar waveguides. Moreover, these properties may extend to analogous systems governed by similar equations, such as tight-binding and coupled-mode theories. We hope these findings will expand the usage of quantum light on photonic systems with topological properties. Opening the door for greater control and stability of quantum properties and allowing for the creation

of new quantum technology.

# Bibliography


[1] Roman Schnabel. Squeezed states of light and their applications in laser interferometers. *Physics Reports*, 684:1–51, April 2017. arXiv:1611.03986 [quant-ph].

[2] The LIGO Scientific Collaboration, J. Aasi, B. P. Abbott, R. Abbott, T. Abbott, M. R. Abernathy, K. Ackley, C. Adams, T. Adams, and P. Addesso. Advanced LIGO. *Classical and Quantum Gravity*, 32(7):074001, March 2015. Publisher: IOP Publishing.

[3] Samuel L. Braunstein and Peter van Loock. Quantum information with continuous variables. *Reviews of Modern Physics*, 77(2):513–577, June 2005. Publisher: American Physical Society.

[4] Klaus von Klitzing. The quantized Hall effect. *Reviews of Modern Physics*, 58(3):519–531, July 1986. Publisher: American Physical Society.

[5] K. v. Klitzing, G. Dorda, and M. Pepper. New Method for High-Accuracy Determination of the Fine-Structure Constant Based on Quantized Hall Resistance. *Physical Review Letters*, 45(6):494–497, August 1980.

[6] M. Hafezi, S. Mittal, J. Fan, A. Migdall, and J. M. Taylor. Imaging topological edge states in silicon photonics. *Nature Photonics*, 7(12):1001–1005, December 2013. Number: 12 Publisher: Nature Publishing Group.

[7] Mohammad Hafezi, Eugene A. Demler, Mikhail D. Lukin, and Jacob M. Taylor. Robust optical delay lines with topological protection. *Nature Physics*, 7(11):907–912, November 2011. Number: 11 Publisher: Nature Publishing Group.

[8] Tomoki Ozawa, Hannah M. Price, Alberto Amo, Nathan Goldman, Mohammad Hafezi, Ling Lu, Mikael C. Rechtsman, David Schuster, Jonathan Simon, and Oded Zilberberg. Topological photonics. *Reviews of Modern Physics*, 91(1):015006, March 2019. Publisher: American Physical Society.

[9] Jean-Luc Tambasco, Giacomo Corrielli, Robert J. Chapman, Andrea Crespi, Oded Zilberberg, Roberto Osellame, and Alberto Peruzzo. Quantum interference of topological states of light. *Science Advances*, 4(9):eaat3187, September 2018. Publisher: American Association for the Advancement of Science.

[10] Joaquin Medina Dueñas, Gabriel O'Ryan Pérez, Carla Hermann-Avigliano, and Luis E. F. Foa Torres. Quadrature protection of squeezed states in a one-dimensional photonic topological insulator. *Quantum*, 5:526, August 2021. Publisher: Verein zur Förderung

des Open Access Publizierens in den Quantenwissenschaften.

[11] D. J. Thouless, M. Kohmoto, M. P. Nightingale, and M. den Nijs. Quantized Hall Conductance in a Two-Dimensional Periodic Potential. *Physical Review Letters*, 49(6):405–408, August 1982.

[12] F. D. M. Haldane. Model for a Quantum Hall Effect without Landau Levels: Condensed-Matter Realization of the "Parity Anomaly". *Physical Review Letters*, 61(18):2015–2018, October 1988. Publisher: American Physical Society.

[13] C. L. Kane and E. J. Mele. Quantum Spin Hall Effect in Graphene. *Physical Review Letters*, 95(22):226801, November 2005. Publisher: American Physical Society.

[14] B. Andrei Bernevig, Taylor L. Hughes, and Shou-Cheng Zhang. Quantum Spin Hall Effect and Topological Phase Transition in HgTe Quantum Wells. *Science*, 314(5806):1757–1761, December 2006. Publisher: American Association for the Advancement of Science.

[15] Liang Fu, C. L. Kane, and E. J. Mele. Topological Insulators in Three Dimensions. *Physical Review Letters*, 98(10):106803, March 2007. Publisher: American Physical Society.

[16] Shuang Jia, Su-Yang Xu, and M. Zahid Hasan. Weyl semimetals, Fermi arcs and chiral anomalies. *Nature Materials*, 15(11):1140–1144, November 2016. Number: 11 Publisher: Nature Publishing Group.

[17] Netanel H. Lindner, Gil Refael, and Victor Galitski. Floquet topological insulator in semiconductor quantum wells. *Nature Physics*, 7(6):490–495, June 2011. Number: 6 Publisher: Nature Publishing Group.

[18] Lei Xiao, Tianshu Deng, Kunkun Wang, Gaoyan Zhu, Zhong Wang, Wei Yi, and Peng Xue. Non-Hermitian bulk–boundary correspondence in quantum dynamics. *Nature Physics*, 16(7):761–766, July 2020. Number: 7 Publisher: Nature Publishing Group.

[19] Martin Brandenbourger, Xander Locsin, Edan Lerner, and Corentin Coulais. Non-reciprocal robotic metamaterials. *Nature Communications*, 10(1):4608, October 2019. Number: 1 Publisher: Nature Publishing Group.

[20] Ching Hua Lee, Stefan Imhof, Christian Berger, Florian Bayer, Johannes Brehm, Laurens W. Molenkamp, Tobias Kiessling, and Ronny Thomale. Topolectrical Circuits. *Communications Physics*, 1(1):1–9, July 2018. Number: 1 Publisher: Nature Publishing Group.

[21] Ling Lu, John D. Joannopoulos, and Marin Soljačić. Topological photonics. *Nature Photonics*, 8(11):821–829, November 2014. Number: 11 Publisher: Nature Publishing Group.

[22] J. C. Slater and G. F. Koster. Simplified LCAO Method for the Periodic Potential Problem. *Physical Review*, 94(6):1498–1524, June 1954. Publisher: American Physical Society.

[23] Ashcroft, N.W. and Mermin, N.D. (1976) Solid State Physics. Saunders College, Philadelphia, 116, 217. - References - Scientific Research Publishing.

[24] Rudolf Peierls, Sir Rudolf Ernst Peierls, and Rudolf Ernst Peierls. *Quantum Theory of Solids*. Clarendon Press, 1955. Google-Books-ID: WvPcBUsSJBAC.

[25] W. P. Su, J. R. Schrieffer, and A. J. Heeger. Solitons in Polyacetylene. *Physical Review Letters*, 42(25):1698–1701, June 1979. Publisher: American Physical Society.

[26] W. P. Su, J. R. Schrieffer, and A. J. Heeger. Soliton excitations in polyacetylene. *Physical Review B*, 22(4):2099–2111, August 1980. Publisher: American Physical Society.

[27] János K. Asbóth, László Oroszlány, and András Pályi. A Short Course on Topological Insulators: Band-structure topology and edge states in one and two dimensions. *arXiv:1509.02295 [cond-mat]*, 919, 2016. arXiv: 1509.02295.

[28] Michel Fruchart and David Carpentier. An introduction to topological insulators. *Comptes Rendus Physique*, 14(9):779–815, November 2013.

[29] J. Zak. Berry's phase for energy bands in solids. *Physical Review Letters*, 62(23):2747–2750, June 1989. Publisher: American Physical Society.

[30] F. Munoz, Fernanda Pinilla, J. Mella, and Mario I. Molina. Topological properties of a bipartite lattice of domain wall states. *Scientific Reports*, 8(1):17330, November 2018. Number: 1 Publisher: Nature Publishing Group.

[31] S. A. Kivelson. Electron Fractionalization, June 2001. arXiv:cond-mat/0106126.

[32] A. J. Heeger, S. Kivelson, J. R. Schrieffer, and W. P. Su. Solitons in conducting polymers. *Reviews of Modern Physics*, 60(3):781–850, July 1988. Publisher: American Physical Society.

[33] Dror G. Feitelson. *Optical computing: a survey for computer scientists*. MIT Press, Cambridge, MA, USA, October 1988.

[34] Keisuke Goda. Biophotonics and beyond. *APL Photonics*, 4(5):050401, May 2019.

[35] Alexander M. Streltsov and Nicholas F. Borrelli. Study of femtosecond-laser-written waveguides in glasses. *JOSA B*, 19(10):2496–2504, October 2002. Publisher: Optica Publishing Group.

[36] Shanhui Fan, Wonjoo Suh, and J. D. Joannopoulos. Temporal coupled-mode theory for the Fano resonance in optical resonators. *JOSA A*, 20(3):569–572, March 2003. Publisher: Optica Publishing Group.

[37] Immanuel Bloch. Ultracold quantum gases in optical lattices. *Nature Physics*, 1(1):23–30, October 2005. Number: 1 Publisher: Nature Publishing Group.

[38] H.A. Haus and W. Huang. Coupled-mode theory. *Proceedings of the IEEE*, 79(10):1505–1518, October 1991. Conference Name: Proceedings of the IEEE.

[39] Ignacio Alberto Salinas Valdivieso. Localización y transporte controlado en redes fotóni-

cas: Blandas planas, no-linealidad y flujos magnéticos efectivos. 2023. Accepted: 2023-04-13T14:18:22Z Publisher: Universidad de Chile.

[40] K. M. Davis, K. Miura, N. Sugimoto, and K. Hirao. Writing waveguides in glass with a femtosecond laser. *Optics Letters*, 21(21):1729–1731, November 1996. Publisher: Optica Publishing Group.

[41] Yusuke Nasu, Masaki Kohtoku, and Yoshinori Hibino. Low-loss waveguides written with a femtosecond laser for flexible interconnection in a planar light-wave circuit. *Optics Letters*, 30(7):723–725, April 2005. Publisher: Optica Publishing Group.

[42] Thomas Calmano, Anna-Greta Paschke, Sebastian Müller, Christian Kränkel, and Günter Huber. Curved Yb:YAG waveguide lasers, fabricated by femtosecond laser inscription. *Optics Express*, 21(21):25501–25508, October 2013. Publisher: Optica Publishing Group.

[43] Koji Sugioka. Femtosecond laser three-dimensional micro- and nanofabrication. *Journal of Applied Physics*, 1:041303, December 2014.

[44] R. Hanbury Brown and R. Q. Twiss. Correlation between Photons in two Coherent Beams of Light. *Nature*, 177(4497):27–29, January 1956. Number: 4497 Publisher: Nature Publishing Group.

[45] Roy J. Glauber. The Quantum Theory of Optical Coherence. *Physical Review*, 130(6):2529–2539, June 1963. Publisher: American Physical Society.

[46] H. J. Kimble, M. Dagenais, and L. Mandel. Photon Antibunching in Resonance Fluorescence. *Physical Review Letters*, 39(11):691–695, September 1977. Publisher: American Physical Society.

[47] R. E. Slusher, L. W. Hollberg, B. Yurke, J. C. Mertz, and J. F. Valley. Observation of Squeezed States Generated by Four-Wave Mixing in an Optical Cavity. *Physical Review Letters*, 55(22):2409–2412, November 1985. Publisher: American Physical Society.

[48] Christopher Gerry and Peter Knight. *Introductory Quantum Optics*. Cambridge University Press, Cambridge, 2004.

[49] Marlan O. Scully and M. Suhail Zubairy. *Quantum Optics*. Cambridge University Press, Cambridge, 1997.

[50] Fulvio Flamini, Nicolò Spagnolo, and Fabio Sciarrino. Photonic quantum information processing: a review. *Reports on Progress in Physics*, 82(1):016001, November 2018. Publisher: IOP Publishing.

[51] Sergei Slussarenko and Geoff J. Pryde. Photonic quantum information processing: A concise review. *Applied Physics Reviews*, 6(4):041303, October 2019.

[52] Charles Santori, Matthew Pelton, Glenn Solomon, Yseulte Dale, and Yoshihisa Yamamoto. Triggered Single Photons from a Quantum Dot. *Physical Review Letters*, 86(8):1502–1505, February 2001. Publisher: American Physical Society.

[53] Samuel Deléglise, Igor Dotsenko, Clément Sayrin, Julien Bernu, Michel Brune, Jean-Michel Raimond, and Serge Haroche. Reconstruction of non-classical cavity field states with snapshots of their decoherence. *Nature*, 455(7212):510–514, September 2008. Number: 7212 Publisher: Nature Publishing Group.

[54] Caspar Groiseau, Alexander E.J. Elliott, Stuart J. Masson, and Scott Parkins. Proposal for a Deterministic Single-Atom Source of Quasisuperradiant $N$-Photon Pulses. *Physical Review Letters*, 127(3):033602, July 2021. Publisher: American Physical Society.

[55] M. Uria, P. Solano, and C. Hermann-Avigliano. Deterministic Generation of Large Fock States. *Physical Review Letters*, 125(9):093603, August 2020. Publisher: American Physical Society.

[56] A. K. Ekert and P. L. Knight. Correlations and squeezing of two-mode oscillations. *American Journal of Physics*, 57(8):692–697, August 1989. Publisher: American Association of Physics Teachers.

[57] Min Xiao, Ling-An Wu, and H. J. Kimble. Precision measurement beyond the shot-noise limit. *Physical Review Letters*, 59(3):278–281, July 1987. Publisher: American Physical Society.

[58] R. Simon, N. Mukunda, and Biswadeb Dutta. Quantum-noise matrix for multimode systems: U(n) invariance, squeezing, and normal forms. *Physical Review A*, 49(3):1567–1583, March 1994. Publisher: American Physical Society.

[59] Roy S. Bondurant and Jeffrey H. Shapiro. Squeezed states in phase-sensing interferometers. *Physical Review D*, 30(12):2548–2556, December 1984. Publisher: American Physical Society.

[60] P. Grangier, R. E. Slusher, B. Yurke, and A. LaPorta. Squeezed-light–enhanced polarization interferometer. *Physical Review Letters*, 59(19):2153–2156, November 1987. Publisher: American Physical Society.

[61] J. Aasi, J. Abadie, B. P. Abbott, R. Abbott, T. D. Abbott, M. R. Abernathy, C. Adams, T. Adams, P. Addesso, and R. X. Adhikari. Enhanced sensitivity of the LIGO gravitational wave detector by using squeezed states of light. *Nature Photonics*, 7(8):613–619, August 2013. Number: 8 Publisher: Nature Publishing Group.

[62] B. J. Lawrie, P. D. Lett, A. M. Marino, and R. C. Pooser. Quantum Sensing with Squeezed Light. *ACS Photonics*, 6(6):1307–1318, June 2019. Publisher: American Chemical Society.

[63] Samuel L. Braunstein and H. J. Kimble. Teleportation of Continuous Quantum Variables. *Physical Review Letters*, 80(4):869–872, January 1998. Publisher: American Physical Society.

[64] Gerardo Adesso and Fabrizio Illuminati. Entanglement in continuous-variable systems: recent advances and current perspectives. *Journal of Physics A: Mathematical and Theoretical*, 40(28):7821, June 2007.

[65] Christian Weedbrook, Stefano Pirandola, Raúl García-Patrón, Nicolas J. Cerf, Timothy C. Ralph, Jeffrey H. Shapiro, and Seth Lloyd. Gaussian quantum information. *Reviews of Modern Physics*, 84(2):621–669, May 2012. Publisher: American Physical Society.

[66] Ulrik L. Andersen, Tobias Gehring, Christoph Marquardt, and Gerd Leuchs. 30 years of squeezed light generation. *Physica Scripta*, 91(5):053001, April 2016. Publisher: IOP Publishing.

[67] Pierre-Élie Larré and Iacopo Carusotto. Propagation of a quantum fluid of light in a cavityless nonlinear optical medium: General theory and response to quantum quenches. *Physical Review A*, 92(4):043802, October 2015. Publisher: American Physical Society.

[68] K. Igeta and Y. Yamamoto. Quantum mechanical computers with single atom and photon fields. In *International Conference on Quantum Electronics (1988), paper TuI4*, page TuI4. Optica Publishing Group, July 1988.

[69] F. D. M. Haldane and S. Raghu. Possible Realization of Directional Optical Waveguides in Photonic Crystals with Broken Time-Reversal Symmetry. *Physical Review Letters*, 100(1):013904, January 2008. Publisher: American Physical Society.

[70] Jiho Noh, Sheng Huang, Kevin P. Chen, and Mikael C. Rechtsman. Observation of Photonic Topological Valley Hall Edge States. *Physical Review Letters*, 120(6):063902, February 2018. Publisher: American Physical Society.

[71] M. Hafezi, P. Adhikari, and J. M. Taylor. Chemical potential for light by parametric coupling. *Physical Review B*, 92(17):174305, November 2015. Publisher: American Physical Society.

[72] Jan Klaers, Julian Schmitt, Frank Vewinger, and Martin Weitz. Bose–Einstein condensation of photons in an optical microcavity. *Nature*, 468(7323):545–548, November 2010. Number: 7323 Publisher: Nature Publishing Group.

[73] José Lebreuilly, Alberto Biella, Florent Storme, Davide Rossini, Rosario Fazio, Cristiano Ciuti, and Iacopo Carusotto. Stabilizing strongly correlated photon fluids with non-Markovian reservoirs. *Physical Review A*, 96(3):033828, September 2017. Publisher: American Physical Society.

[74] Yaron Silberberg, Yoav Lahini, Yaron Bromberg, Eran Small, and Roberto Morandotti. Universal Correlations in a Nonlinear Periodic 1D System. *Physical Review Letters*, 102(23):233904, June 2009. Publisher: American Physical Society.

[75] Mor Verbin, Oded Zilberberg, Yaacov E. Kraus, Yoav Lahini, and Yaron Silberberg. Observation of Topological Phase Transitions in Photonic Quasicrystals. *Physical Review Letters*, 110(7):076403, February 2013. Publisher: American Physical Society.

[76] S. Rojas-Rojas, E. Barriga, C. Muñoz, P. Solano, and C. Hermann-Avigliano. Manipulation of multimode squeezing in a coupled waveguide array. *Physical Review A*, 100(2):023841, August 2019. Publisher: American Physical Society.

[77] Andrea Blanco-Redondo, Imanol Andonegui, Matthew J. Collins, Gal Harari, Yaakov Lumer, Mikael C. Rechtsman, Benjamin J. Eggleton, and Mordechai Segev. Topological Optical Waveguiding in Silicon and the Transition between Topological and Trivial Defect States. *Physical Review Letters*, 116(16):163901, April 2016. Publisher: American Physical Society.

[78] David Poulin, Angie Qarry, Rolando Somma, and Frank Verstraete. Quantum Simulation of Time-Dependent Hamiltonians and the Convenient Illusion of Hilbert Space. *Physical Review Letters*, 106(17):170501, April 2011. Publisher: American Physical Society.

# Energy spectrum and wavefunction distribution of the systems in results

The following shows the energy spectrum and wavefunctions of the system used for the simulation in the results.

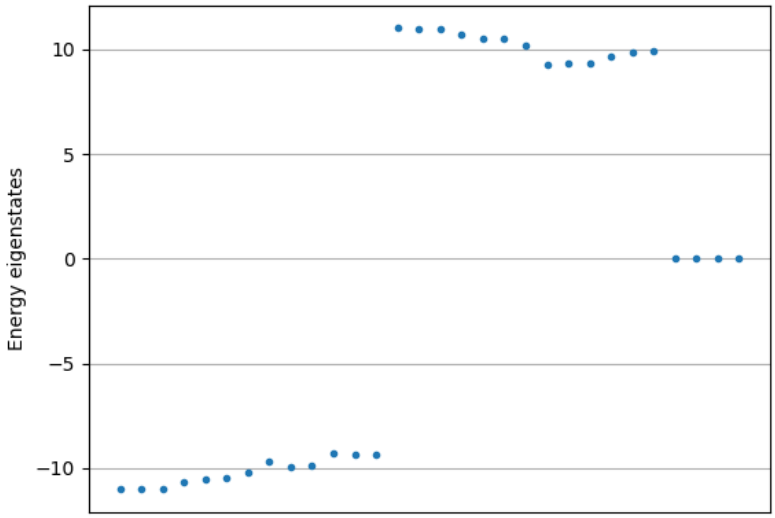


Figure 0.1: Energy spectrum SSH in a topological phase with two domain walls in the positions $p_a = 11$ and $p_b = 20$. The system has 32 sites and couplings $u = 1$, $v = 1 + 6tanh(1)$.

Because of the two domain walls, we have 4 states with zero energy. One per edge and one per domain wall. The distribution weight across the lattice can be seen in figure 0.2. The amplitude of all energies quickly decays when moving away from the domain walls and edges, they are sufficiently apart for the injected light to be confined on the domain wall.

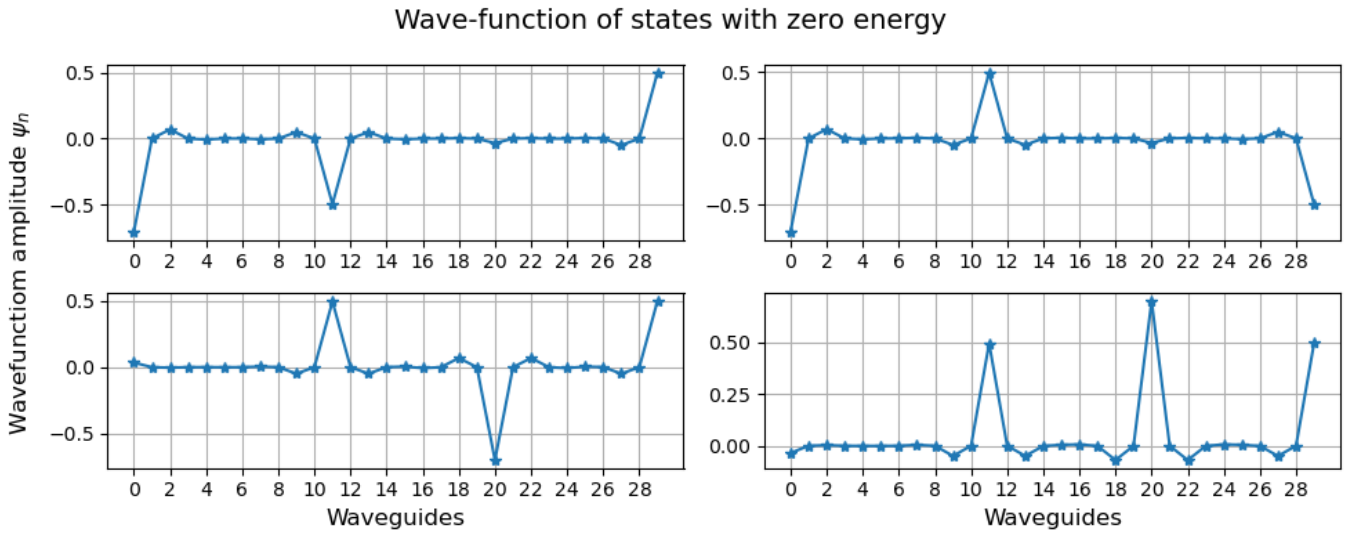


Figure 0.2: Wavefunction across the lattice of the states with zero energy in a system with two domain walls.

For three domain walls, we can see there is a similar extra zero energy state corresponding to the third domain wall.

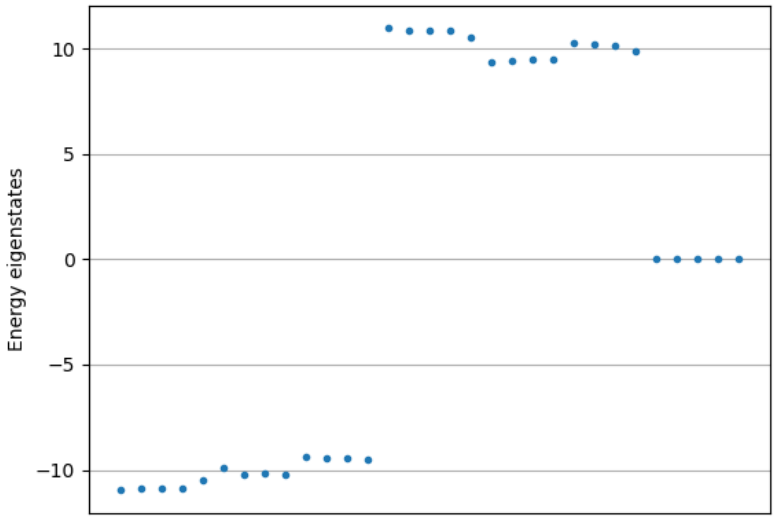


Figure 0.3: Energy spectrum SSH in a topological phase with three domain walls on the positions $p_a = 9$ , $p_b = 16$ and $p_c = 23$.

The distribution weight across the lattice with three domain walls for each zero energy state is shown in 0.4. Just like for the dimer, all states with zero energy quickly decay when moving away from the edges or domain walls, ensuring the light keeps propagating mainly through one of those waveguides if injected in it.

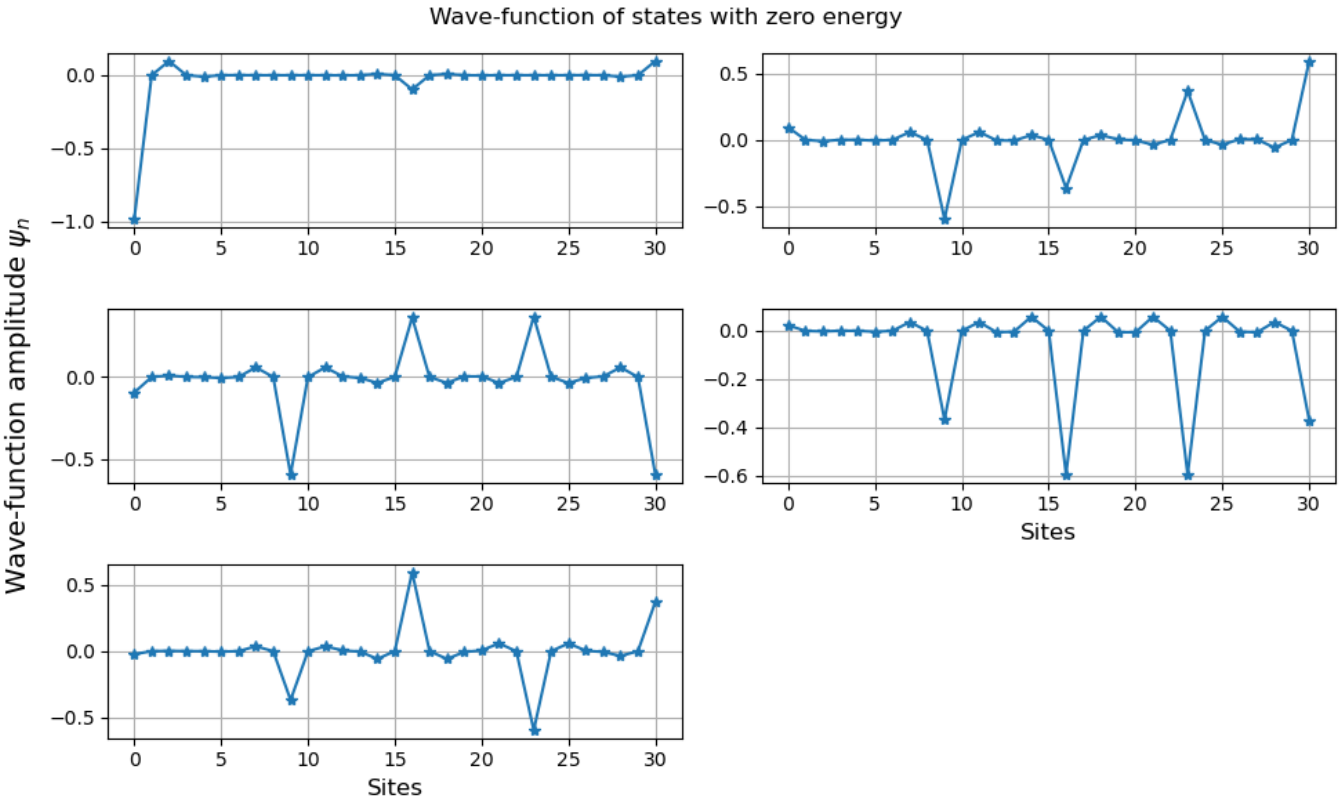


Figure 0.4: Wavefunction across the lattice of the states with zero energy in a system with three domain walls.